

Magazine of Civil Engineering

ISSN 2712-8172

Online peer-reviewed open-access scientific journal in the field of Civil and Construction Engineering

Founder and Publisher: Peter the Great St. Petersburg Polytechnic University

This journal is registered by the Federal Service for Supervision of Communications, Information Technology, and Mass Media (ROSKOMNADZOR) in 2020. Certificate El No. FS77-77906 issued February 19, 2020.

Periodicity: 8 issues per year

Publication in the journal is open and free for all authors and readers.

Indexing: Scopus, Web of Sceince (ESCI, RSCI), DOAJ, Compendex, Google Academia, Index Copernicus, ProQuest, Ulrich's Serials Analysis System, CNKI

Corresponding address: 29 Polytechnicheskaya st., Saint Petersburg, 195251, Russia

Chief science editor:

D.Sc., Galina L. Kozinetc

Deputy chief science editors:

D.Sc., Sergey V. Korniyenko

Executive editor: Ekaterina A. Linnik

Translator, editor: Irina Ye. Lebedeva

Proofreader: Philipp Chrysanthes S. Bastian

DT publishing specialist: Anastasiya A. Kononova

Contacts:

E-mail: mce@spbstu.ru

Web: http://www.engstroy.spbstu.ru

Date of issue: 26.12.2024

© Peter the Great St. Petersburg Polytechnic University. All rights reserved.

© Coverpicture - Polina A. Ivanova

Editorial board:

T. Awwad, PhD, professor, Damascus University, Syrian Arab Republic

A.I. Belostotsky, D.Sc., professor, StaDyO Research & Engineering Centre, Russia

A.I. Borovkov, PhD, professor, Peter the Great St. Petersburg Polytechnic University, Russia

M. Veljkovic, PhD, professor, Delft University of Technology, The Netherlands

R.D. Garg, PhD, professor, Indian Institute of Technology Roorkee (IIT Roorkee), India

M. Garifullin, PhD, postdoctoral researcher, Tampere University, Finland

T. Gries, Dr.-Ing., professor, RWTH Aachen University, Germany

T.A. Datsyuk, D.Sc., professor, Saint-Petersburg State University of Architecture and Civil Engineering, Russia

V.V. Elistratov, D.Sc., professor, Peter the Great St. Petersburg Polytechnic University, Russia

O.N. Zaitsev, D.Sc., professor, Southwest State University, Russia

T. Kärki, Dr.-Ing., professor, Lappeenranta University of Technology, Russia

G.L. Kozinetc, D.Sc., professor, Peter the Great St. Petersburg Polytechnic University, Russia

D.V. Kozlov, D.Sc., professor, National Research Moscow State Civil Engineering University, Russia S.V. Korniyenko, D.Sc., professor, Volgograd State Technical University, Russia

Yu.G. Lazarev, D.Sc., professor, Peter the Great St. Petersburg Polytechnic University, Russia

M.M. Muhammadiev, D.Sc., professor, Tashkent State Technical University, Republic of Uzbekistan H. Pasternak, Dr.-Ing.habil., professor, Brandenburgische Technische Universität, Germany

F. Rögener, Dr.-Ing., professor, Technology Arts Science TH Köln, Germany

V.V. Sergeev, D.Sc., professor, Peter the Great St. Petersburg Polytechnic University, Russia

T.Z. Sultanov, D.Sc., professor, Tashkent Institute of Irrigation and Agricultural Mechanization Engineers, Republic of Uzbekistan

A.M. Sychova, D.Sc., professor, Military Space Academy named after A.F. Mozhaysky, Russia M.G. Tyagunov, D.Sc., professor, National Research University "Moscow Power Engineering Institute", Russia

M.P. Fedorov, D.Sc., professor, Peter the Great St. Petersburg Polytechnic University, Russia

D. Heck, Dr.-Ing., professor, Graz University of Technology, Austria

P. Cao, D.Sc., professor, Jilin University, China A.G. Shashkin, D.Sc., PI Georekonstruktsiya, LLC, Russia

B.M. Yazyev, D.Sc., professor, Don State Technical University, Russia

Contents

Kozinetc, G.L., Chechevichkin, V.N., Tryaskin, M.A., Chechevichkin, A.V., Yakunin, L.A. Hydraulic operating features of filtering cassettes as part of treatment facilities on highways	13201
Rybakov, V.A., Usanova, K., Seliverstov, A.V., Kislitcyna, A.A., Tsvetkova, A.A., Akimov, S.V. Bearing capacity of lightweight steel concrete enclosure wall panels	13202
Vasileva, E.D., Popov, D.N., Vinokurov, P.V., Popov, A.L. Electrically conductive cement composites modified with weakly oxidized graphene	13203
Shen, N.J., Hasan, M., Anuar, N.N. Construction of coconut shell column for the enhancement of expansive soil	13204
Panchenko, L.A., Druzhinina, T.Y. Energetic basis in rational constructions projection	13205
Kozinetc, G.L., Badenko, V.L., Sharapov, D., Shonina, E.V. Method of integrated consideration of factors for calculation of anchor system of pontoons	13206
Abd Hacheem, Z., Al-Khyat, S., Saeed, K.A., Fartosy, S.H.L. Stability of gypseous soils slopes stabilized with cutback asphalt and lime using the finite element method	13207
Suleymanova, L.A., Maslennikova, A.A., Kravchenko, D.E., Martyushev, N.V., Vatin, N.I., Karlina, A.I. Ensuring uniform brightness of the afterglow surface of the hardened cement paste with photoluminescent pigment	13208



Magazine of Civil Engineering

ISSN 2712-8172

journal homepage: http://engstroy.spbstu.ru/

Research article UDC 628.3

DOI: 10.34910/MCE.132.1



Hydraulic operating features of filtering cassettes as part of treatment facilities on highways

G.L. Kozinetc, V.N. Chechevichkin, M.A. Tryaskin, A.V. Chechevichkin 🕒 , L.A. Yakunin 🖾 🔟





Peter the Great St. Petersburg Polytechnic University

⊠ yakunin_la@spbstu.ru

Keywords: surface runoff, shungite, filter cassette, hydraulic mode, filtration

Abstract. Surface runoff water (SRW) from highways is highly polluted and has negative impact on adjacent areas and water bodies. The article describes constructed wetlands (CW), including detention ponds and facilities for sorption post-treatment, one of the simplest methods to treat the SRW from highways. It is established that filter cassettes (FCs) based on gabion constructions (GC) and loaded with shungite rock (SR) are used as sorption post-treatment facility. One of the reasons for the unsatisfactory operation of such facilities on the St. Petersburg Ring Road (the SPb RR) has been analyzed. It is shown that the SR recommended for loading into the FC has a fractional composition of 2÷4 cm and thus mostly providing a turbulent filtration mode of SRW passing through the facility. The impossibility of using SR with the optimal towards sorption treatment fractional composition of (0.1÷0.3) cm within the existing GC is shown. It is also shown that the use of permeable for SRW containers — the filter cartridges (such as FOPS® filters) is shown to be one of the simplest and most effective ways of using SR of optimal fractional composition and working with a large amount of sorption materials. The approach to the organization of complex multistage treatment of surface runoff is shown.

Citation: Kozinetc, G.L., Chechevichkin, V.N., Tryaskin, M.A., Chechevichkin, A.V., Yakunin, L.A. Hydraulic operating features of filtering cassettes as part of treatment facilities on highways. Magazine of Civil Engineering. 2024. 17(8). Article no. 13201. DOI: 10.34910/MCE.132.1

1. Introduction

Surface runoff water (SRW) from highways, currently classified as highly polluted [1, 2], has a negative impact on natural landscapes in the area of highway right-of-way [3-5], on water bodies and watercourses adjacent to them.

The SRW entering water bodies without proper treatment contain significant amounts of toxic pollutants that exert an extremely negative influence on their biocenosis [6, 7]. This leads to degradation of water bodies, ranging from eutrophication to complete disappearance of all life in them.

In order to reduce the negative impact of SRW treatment facilities of various designs are used on highways. The most common of these are constructed wetlands (CWs), the tank-type treatment facilities and the sorption-filtration facilities based on filter cartridges [8-11].

There are about 220 CWs (Fig. 1, 2) on the St. Petersburg Ring Road (RR), which have long ceased to comply with the regulatory document¹, or with the aesthetic ideas of modern man, or with common sense

¹ Federal Road Agency (Rosavtodor). Metodicheskie rekomendatsii po soderzhaniiu ochistnykh sooruzhenii na avtomobil'nykh dorogakh [Methodological recommendations for the maintenance of treatment facilities on highways]. ODM 218.8.005–2014. 2017. 83 p. URL: https://rosavtodor.gov.ru/storage/app/media/uploaded-files/210odm-2188005-2014.pdf?ysclid=m67l2a01ap610205907 (Accessed: 22.12.2024)

[©] Kozinetc, G.L., Chechevichkin, V.N., Tryaskin, M.A., Chechevichkin, A.V., Yakunin, L.A., 2024. Published by Peter the Great St. Petersburg Polytechnic University.

in the field of environmental safety. The detention ponds of the CWs have turned into unattended settling tanks filled with toxic sludge consisting of a mixture of insoluble forms of heavy metals, asphalt pavement microparticles and soot, as well as petroleum products, fragments of dead plants and debris. In their current state, such ponds are not only a pitiful sight, but also a real environmental threat. Today, no one would hardly be surprised by the absence of macrophytes in the CWs, rusty and torn mesh of GC at the air-water interface, territory littered with household waste etc., which are the consequence of improper maintenance (at least according to ODM 218.8.005-2014). These shortcomings of actually CWs on the RR were discussed earlier [2, 12]. Scientific publications dealing with the CWs problems are quite widely represented in domestic [13–17] and foreign periodicals [18–26].



a)

a)



Figure 1. Exterior of the CW (a) and the SRW post-reatment facility based on filter cassettes with shungite-III (b) located on the SPb RR (2018).

b)





Figure 2. Exterior of the CW (a) and the SRW post-reatment facility based on filter cassettes with shungite-III (b) located on the SPb RR (2024).

b)

The use of shungite rock (SR) for sorption post-treatment of the SRW within the CWs became widespread at the turn of the 21st century and exclusively in Russia, during the construction of major highways (RR, Federal Highway M10 "Russia", Federal Highway M11 "Neva" etc.), while discarding the real hydrodynamic conditions of its use in sorption processes.

The study of SR properties, which began in the 19th century [27] and continued in the 20th century, is still relevant today [28–36]. The use of SR (mainly structural type III) for the purification of various water environments is currently carried out in laboratory conditions [37–44] without assessing its real capabilities in the processes of treatment of large volumes of polluted water (as is the case with SRW). The internal structure of shungite-III is unique. It has the appearance of the combination of mutually opposite components (hydrophobic globules of non-graphitized carbon and hydrophilic globules of silicate and aluminosilicate nature). This circumstance ultimately determines the bifunctional properties of shungite-III in aqueous environment. The presence of metal oxide forms in its composition additionally determines its catalytic properties. However, these properties are manifested at low concentration loads and at low velocities of liquid phase movement through the shungite-III layer due to its small porosity and, accordingly, small specific surface area (less than (10÷15) m2/g for shungite-III, while for activated carbons it is 500–1000 m2/g). This is the reason that shungite-III quickly becomes saturated and loses its geoprotective properties upon contact with heavily polluted SRW, subsequently acting as an inert filter material (at best).

The main purposes of the study are to assess the actual operating conditions of the filter cassettes (FC) with SR and the possibilities of their improvement. The research tasks are defined as follows:

- investigation of SR particle size distribution, used in actual FC;
- calculation of the characteristics of the hydraulic operating modes of the FC with SR loading.

2. Methods

One of the CWs on the RR (111th km of the inner ring, intersection with the Karasta River) was selected as a research object, the appearance of which is shown in Fig. 1 and 2. On its territory, the samples of SR from FC (shungite-III) were taken and the necessary measurements were carried out.

The amount of SRW from a given catchment area (W_{srw} , m³) was calculated for one average rainfall (lasting up to 3 h) for the North-West in accordance with recommendations [45]:

$$W_{Srw} = H_{\text{max}} \times F \times 10^{-3},\tag{1}$$

where $H_{\rm max}$ is maximum precipitation layer for one average rainfall [45], mm; F is catchment area, m².

The size of the SR particles in the form of equivalent grain diameter (d_g , cm) was calculated from the projection areas of these particles on the photographs using the raster graphics editor Adobe Photoshop [46]. Filtration coefficients K_f for the SR particles up to 0.5 cm in size were taken from reference data [47], and for particles larger than 0.5 cm were calculated using the Izbash formula [47]:

$$K_f = \left(20 - \frac{14}{d_g}\right) \times P \times \sqrt{d_g}, \tag{2}$$

where K_f is filtration coefficient, cm/s; P is porosity of the layer and equals 0.4; d_g is equivalent diameter of the SR particle, cm.

The SRW flow rate for continuous treatment Q_{tr} (m³/h) through one FC filled with the SR was determined through the specific flow rate q (cm²/s) according to formula (3)

$$Q_{tr} = q \times B,\tag{3}$$

where B is width of the FC, cm.

For the SR particles of 0.05 to 0.5 cm in size, q values were calculated assuming laminar flow using formula (4):

$$q_{lam} = K_f \times \left(\frac{h_1^2 - h_2^2}{2L}\right),\tag{4}$$

where L is length of the FC, cm.

For the SR particles 1–10 cm in size, q values were calculated using the formula based on the dependence proposed by Puzyrevsky for turbulent filtration [47]:

$$q_{turb} = K_f \times \sqrt{\frac{h_1^3 - h_2^3}{3L}},\tag{5}$$

Depression curves were calculated for a rectangular array (the FC) according to formula (4) for laminar and formula (5) for turbulent filtration at given values of K_f , q, h_1 , h_2 and L [47].

3. Results and Discussion

For comparison, Fig. 3 shows:

- shungite-III (piece size 8–12 cm), which was used for loading the FCs on the RR in 2018 (Fig. 1);
- shungite-III (piece size 4–6 cm), which was used for reloading the FCs on the RR in 2024 (Fig. 2);
- fraction of the SR with particles 0.4–0.5 cm in size, which is the maximum (as will be shown below) for the sorption process to be carried out in the laminar filtration mode [48, 49].

Compliance with the conditions of laminar flow of SRW through a layer of SR is mandatory, since the dynamics of sorption in the SR layer is determined exclusively by external diffusion kinetics (only the outer surface of the SR grains is involved in the process).

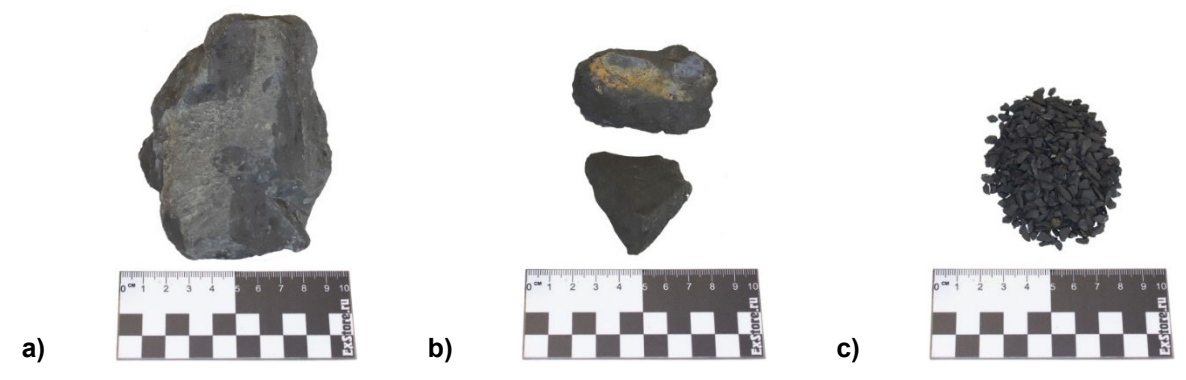


Figure 3. Schungite-III used in the FCs on the SPb RR in 2018 (a) and in 2024 (b), as well as the SR for sorption filters, operating in the optimal sorption-hydraulic mode (c).

Laminar filtration through granular media, defined by Darcy's law [47], has limitations on the ratio of the linear velocity of the liquid phase v (cm/s, m/h) and the grain diameter of the layer d_{φ} (cm):

$$v \times d_g < 0.01 \div 0.07.$$
 (6)

For different given d_g of the SR, the values of υ were calculated, on the basis of which the dependence shown in Fig. 4 (based on the maximum value of the range (6)) was plotted. The area of existence of the laminar flow mode through the SR layer, shown in Fig. 4, determines the limits of optimal values of υ for different d_g of the SR.

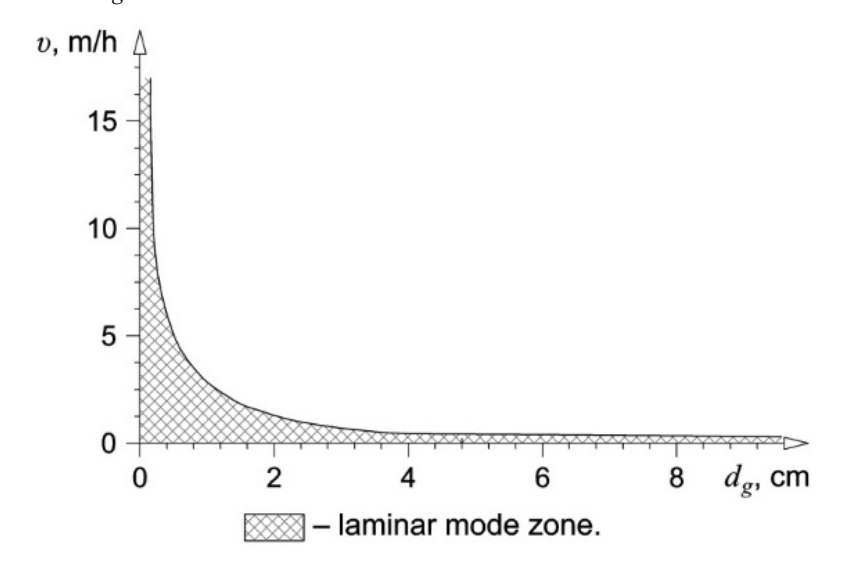


Figure 4. Zone of laminar filtration mode for SR of a different particle size distribution.

It follows from Fig. 4 that for granular layers with the SR particles of 8 to 12 cm in size (used at some other CWs of the SPb RR) the range of water velocities in the laminar mode will be from 0.035 to 0.25 m/h, for the SR fraction (2÷4) cm used according to the recommendations ODM 218.8.005–2014 will be from 0.09 to 1.25 m/h, and for the SR fraction (0.4÷0.5) cm – from 1.0 to 10 m/h, respectively.

What is the hydraulic mode of the SRW flow through the real FCs within the CWs on the RR?

The diagram of the FC filled with SR, the operation and construction of which was described earlier [50], is shown in Fig. 5. The FCs (Fig. 1b and 2b) are assembled on the basis of reinforced concrete trays (type II, intertrack²) and GC filled with SR in accordance with ODM 218.8.005–2014. The length of the tray

² Ministerstvo transportnogo stroitel'stva (Glavtransproekt), Moskovskii gosudarstvennyi proektno-izyskatel'skii institut (Mosgiprotrans). Al'bom vodootvodnykh ustroistv na stantsiiakh [Album of drainage devices at stations]. M., 1975. 90 s. URL: https://gostrf.com/normativ/1/4293830/4293830933.htm (Accessed: 22.12.2024)

is $1.5 \, \text{m}$, the length of the FC in it is $1.0 \, \text{m}$, the inlet cross-sections are $0.5 \, \text{m} \times 0.5 \, \text{m}$. Some of the characteristics of the SPb RR treatment facility are presented in Table 1.

Parameter	Unit	Value	
Catchment area	ha	2.12	
Surface area of detention pond	m^2	160	
SRW flow rate for continuous treatment	m³/h	14.8	
Rainfall layer height in the pond	cm	22.3	
Number of FCs installed	pcs.	3	

Table 1. Some characteristics of the CW at the SPb RR.

For the 3 FCs available at the object under study (total inlet cross-section $-0.75~\text{m}^2$) the filtration rate υ has been calculated and is 19.7 m/h.

The actual filtration rate υ' taking into account the fraction of the cross-sectional area of impermeable particles of the SR loading will be 2 times higher [47].

For a single FC of 0.5 m x 0.5 m x 1.0 m the maximum flow rate of the SRW, still providing laminar mode, will be: $Q_{tr} = 0.06 \,\mathrm{m}^3/\mathrm{h}$ (for d_g from 8 to 12 cm); $Q_{tr} = 0.31 \,\mathrm{m}^3/\mathrm{h}$ (for d_g from 2 to 4 cm); $Q_{tr} = 2.5 \,\mathrm{m}^3/\mathrm{h}$ (for d_g from 0.4 to 0.5 cm).

Accordingly, to ensure laminar filtration mode of the entire volume of SRW from one rainfall, it is necessary to have in the composition of treatment facilities the number n (pcs.) of FCs: n = 247 (for d_g from 8 to 12 cm); n = 48 (for d_g from 2 to 4 cm); n = 6 (for d_g from 0.4 to 0.5 cm).

Currently, only 3 FCs are installed at the facility instead of the required 48 (according to ODM 218.8.005–2014), i.e. 16 times less than the calculated number.

In such conditions the mode of the SRW passing through the FCs of the considered CW will have a pronounced turbulent character, and it is impossible to speak about any sorption treatment.

It should be noted that the velocity mode in the FC is determined not only by the particle size of granular material (d_g) , but also by the difference of SRW levels at the inlet and outlet of the FC $\Delta h = h_1 - h_2$ (Fig. 5).

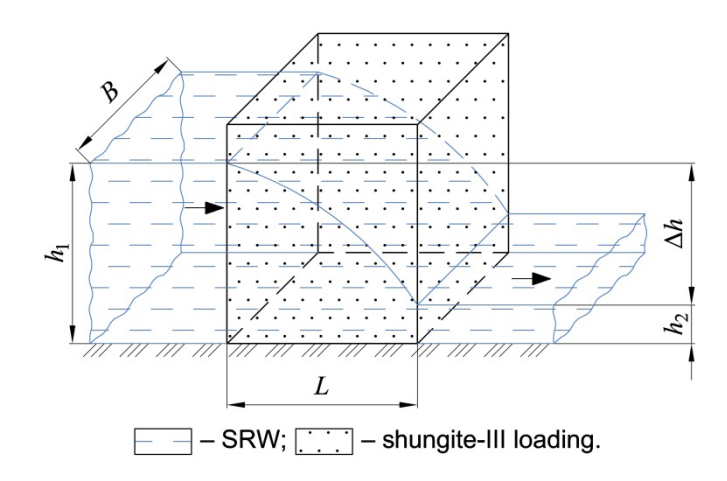


Figure 5. Schematic diagram of the FC on the SPb RR.

Table 2 shows the calculated values of filtration coefficients K_f (cm/s) for a single FC, as well as characteristics such as: SRW flow rate for continuous treatment \mathcal{Q}_{tr} (m³/h), linear velocity $\overline{\upsilon}$ (m/h) and values of Reynolds number (Re), which were calculated for the SR particles of 0.05 to 1.0 cm in size by formulae (3, 4), and for the SR particles of 1.0 to 10.0 cm in size by formula (2, 3, 5). The data in Table 2 were also calculated for two values of Δh (Fig. 5), equal to 10 cm and 1 cm, because of the estimation of

the average water surface elevation in the object pond for an average 3-hour rainfall in St. Petersburg (Δh = 10 cm) and the minimum experimentally determined value of water surface elevation (Δh = 1 cm).

As can be seen from Table 2, the average values of linear velocity of the SRW flow through the FC for Δh = 10 cm are in the zone corresponding to the laminar mode only for SR particles of 0.5 cm and less in size. The average values of linear filtration velocity $\overline{\upsilon}$ (m/h) given in Table 2 were determined as arithmetic averages between the values of linear filtration velocities in the inlet section ($h_1 \times B$, Fig. 5) and in the outlet section $(h_1 \times B)$.

Even for the minimum value of Δh = 1 cm, a laminar filtration mode can be ensured only for the SR particles of 1 cm or less in size. Loadings of the SR with particles larger than 1 cm in any case provide a guaranteed turbulent filtration mode. A similar conclusion can be drawn from the evaluation of the Reynolds number values given in Table 2. These values only for the SR particles smaller than 0.4 cm (at $\Delta h = 10$ cm) and 1.0 cm (at $\Delta h = 1$ cm) are less than the critical level Re = 5÷9 [51], which determines the limit of applicability of Darcy's law.

Thus, FC with SR at any inflows of SRW into the CW detention ponds operate in a purely turbulent mode and cannot provide any significant sorption treatment.

 Δh = 10 cm Δh = 1 cm d_g , cm K_f , cm/s $\overline{\upsilon}$, m/h Re $\overline{\upsilon}$, m/h Re Q_{tr} , m 3 /h Q_{tr} , m³/h 0.17 0.0007 0.05 0.06 0.011 0.025 0.052 0.007 0.20 0.10 0.25 0.045 0.68 0.0032 0.061 0.017 0.20 0.85 0.153 2.30 1.2 0.0108 0.206 0.114 0.40 2.2 0.396 5.94 6.8 0.0277 0.529 0.60 0.50 2.8 0.504 7.52 10.5 0.0353 0.674 0.95 1* 26 2.40 3.5 0.63 0.0443 0.846 9.45 1** 25.7 71 0.378 20 2.4 1.71 7.22 2 7.3 5.15 77.3 440 1.13 21.4 118 4 13.2 9.36 140.3 1560 2.05 39.2 432 5 16.5 11.7 176 2444 2.56 48.8 678 8 20.6 219 4880 1350 14.6 3.19 60.8

Table 2. Values of characteristics of hydraulic operation modes of the FC with SR loading.

23.5

10

Fig. 6 shows the depression curves calculated by formula (4) for a FC with a 0.3 cm grain size of SR and by formula (5) for a FC with a 3 cm grain size of SR. The areas under the curves (determined by the method described in [46]), corresponding in the actual process to the volume of the FC filled with water, are close to each other (the difference is not more than 4 %), which indicates that the degree of filling of the interparticle volume of the layer (about 70 %) is practically the same for laminar and turbulent modes. Thus, due to the continuity of the flow, the linear velocity varies significantly from the inlet section of the module to its outlet section, and a part of the loading volume (not filled with water) does not participate in the filtration and mass transfer process at all.

250

6990

3.64

69.40

1930

^{16.7} * The calculation is carried out under the condition of compliance with Darcy's law.

^{**} The calculation is carried out under the condition of non-compliance with Darcy's law.

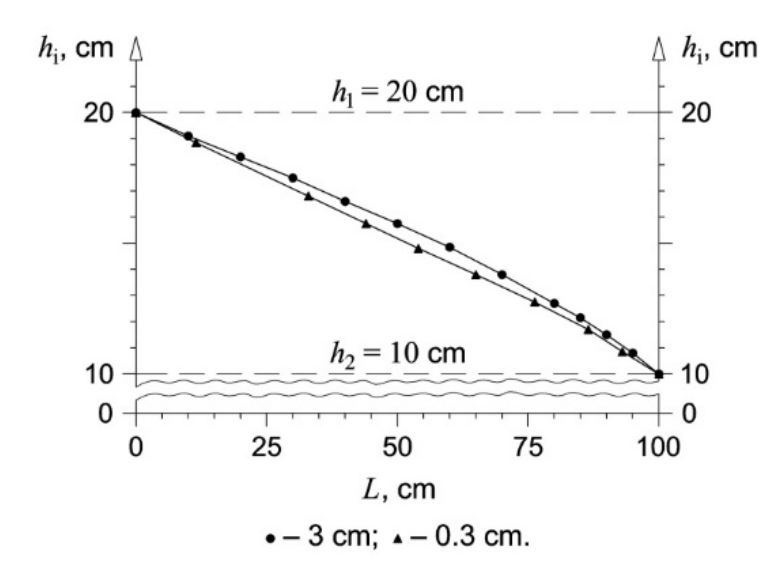


Figure 6. Depression curves calculated for a standard FC with a SR load of a different particle size distribution.

How can the situation with the actual treatment of the SRW on the SPb RR be improved? There are two ways.

The first way is to significantly increase the number of parallel FCs (as it was said earlier – by 16 times when they are filled with the SR of particles 2–4 cm in size) in order to reduce the linear filtration velocity to acceptable for laminar filtration values. However, in this case, the effective formation of the sorption front will require a FC 6–7 m in length (instead of 1 m in fact). In addition, the SR of particles 2–4 cm in size are practically not retained by any of the standard meshes (from 50÷70 mm to 100÷120 mm) of gabion structures currently used, and another structural solution is required to accommodate it.

The second way is to use fractions of the SR no more than 0.5 cm in size (and better from 0.1 to 0.3 cm). It is advisable to use ready-made products – FC, that allow easy manipulation with quantities of the SR of several tons, for the convenience of manipulation with significant amounts of the SR with a particle size from 0.1 to 0.3 cm (required for sorption treatment of SRW).

The FOPS® filters are considered to be the most developed filters of this type in practical terms [9–13].

The basic diagram of a possible facility for complex treatment of the SRW from the RR section under consideration is presented in Fig. 7.

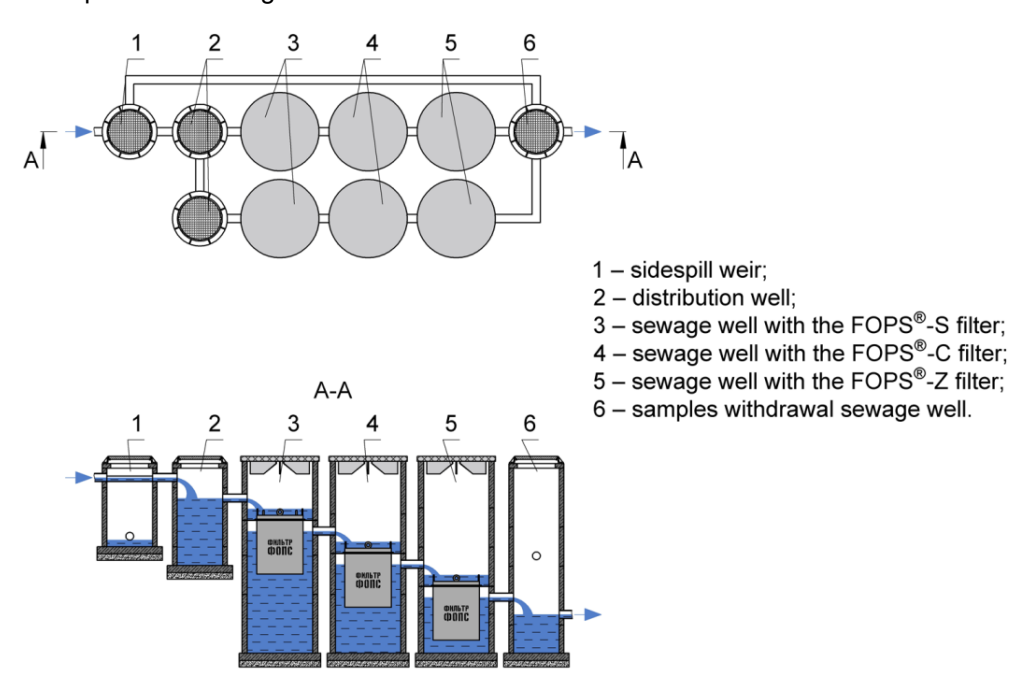


Figure 7. Schematic diagram of the facility for complex treatment of the SRW from the RR section under consideration based on the FOPS® filters.

The complexity of the treatment lies in the use of three cascade facility, in which the following are sequentially located: the filter-separator (FOPS®-S), the carbon filter (FOPS®-C) and the zeolite filter (FOPS®-Z). The required capacity of the facility is achieved by using of two parallel branches (3 filters in each) with a capacity of up to 8.0 m³/h each. The bed height in the filters is 1.8 m, which provides acceptable dynamics of the sorption process with a material grain size from 0.1–0.3 cm in size.

In this scheme FOPS®-C filter with activated carbon load can be replaced with a FOPS® filter with shungite-III loading (fraction 0.1–0.3 cm).

4. Conclusion

- 1. The use of SR in accordance with current regulatory documents in the form of crushed stone with particle size 2–4 cm and more for sorption post-treatment of SRW contradicts the generally accepted practice of sorption processes in liquid media, where materials with grain size of no more than 0.5 cm are used.
- The use of SR (fraction 2–4 cm) in FCs under real conditions provides a turbulent mode of SRW flow passage.
- 3. The placement of SR with particles 0.1–0.3 cm in size (optimal from the point of view of the sorption processes) is impossible with the FCs based on GC used in the existing SRW treatment facilities on the RR.
- 4. The implementation of the optimum conditions of SRW treatment process is possible when using SR with particles 0.1–0.3 cm in size, placed in water-permeable containers of industrial manufacture (filter cartridges), such as the FOPS® filters, convenient for treatment facilities operation.
- 5. The use of SR placed in filter cartridges (such as FOPS® filters) allows them to be used for complex treatment of surface runoff water as a part of multi-cascade treatment facilities.

References

- 1. Sweetapple, Ch., Webber, Ja., Hastings, A., Melville-Shreeve, P. Realising smarter stormwater management: A review of the barriers and a roadmap for real world application. Water Research. 2023. 244. Pp. 120505. DOI: 10.1016/j.watres.2023.120505
- Glukhov, V.V., Grekov, M.A., Kozinets, G.L., Triaskin, M.A., Chechevichkin, V.N., Chechevichkin, A.V., Iakunin, L.A. Disadvantages of using gabion grid constructions in hydraulic structures for treatment of surface runoff from highways. Ecology of Urban Areas. 2022. 2. S. 40–52. DOI: 10.24412/1816-1863-2022-2-40-52
- Dakhova, O.O., Khuchunayev, B.M., Kupovykh, G.V. Chemical and physical contamination of urban ecosystems by automobile transport. Izvestiya vuzov. Severo-Kavkazskii region. Natural science. 2016. 4(192). Pp. 67–72. DOI: 10.18522/0321-3005-2016-4-67-72
- 4. Gorodkov, A.V., Kozonogina, I.V. Research and assessment of environmental near trunk road areas of the city by the factor of pollution of automobile transport. Biosphere Compatibility: Man, Region, Technology. 2017. 1(17). Pp. 53–60.
- Borisochkina, T.I., Kolchanova, K.A. Heavy metals in natural-anthropogenic and agricultural landscapes of the impact zones of metallurgical complexes of the Tula industrial agglomeration. Ecology & Industry of Russia. 2023. 27(1). Pp. 66–71. DOI: 10.18412/1816-0395-2023-1-66-71
- 6. Sabanaev R.N., Nikitin O.V., Latypova V.Z., Lukoianov D.E., Stepanova N.Yu., Yakovleva O.G., Shagidullina R.A., Gorshkova A.T., Safiullin R.M. Nagruzka livnevogo stoka na poverkhnostnyye vody vnutrigorodskogo vodotoka [Stormwater runoff loading to surface waters of an inner-city watercourse]. Herald of Technological University. 2016. 19(19). Pp. 157–160.
- Prozhorina, T.I., Yakunina, N.I., Nagikh, T.V. Investigation of the surface runoff influence from residential areas on the Voronezh reservoir pollution. Proceedings of Voronezh State University. Series: Geography. Geoecology. 2018. 2. Pp. 115–120.
- 8. Vinokurov, K.I., Krestyaninova, A.Yu. The local treatment facilities for surface runoff on highways and bridge crossings. Ekologiya & Stroitelstvo. 2019. 4. S. 42–52. DOI: 10.35688/2413-8452-2019-04-005
- 9. Frolova, I.E., Sashin, N.K., Khlupin, V.S. Treatment of surface runoff from port hydraulic structures. Ekologiya & Stroitelstvo. 2021. 4. Pp. 25–36. DOI: 10.35688/2413-8452-2021-04-002
- 10. Madykhov, R.M., Khafizov, E.R. Application of filter cartridges for cleaning of superficial flows from municipal streets. Transport equipment and technology. 2020. 2(17). Pp. 19.
- 11. Chechevichkin, A.V. Engineering and application of local treatment facilities of a land runoff based on FOPS® filters. Saint-Petersburg.: Lyubavich, 2017. 176 p.
- 12. Glukhov, V.V., Grekov, M.A., Kozinets, G.L., Chechevichkin, V.N., Chechevichkin, A.V., Yakunin, L.A. Current state of surface runoff treatment facilities of the ring road of St. Petersburg and the possibility of their modernization. Ecology of Urban Areas. 2020. 4. Pp. 41–52. DOI: 10.24412/1816-1863-2020-4-41-52
- 13. Krivitskiy, S.V. Ochistka poverkhnostnykh stokov s ispolzovaniyem gidrobotanicheskikh ploshchadok. Ecology & Industry of Russia. 2007. 3. Pp. 20–23.
- Grafkina, M.V., Vitkovsky, D.V. Some aspects of designing phytotreatment facilities. Management of the Technosphere. 2023. 6(2). Pp. 158–169. DOI: 10.34828/UdSU.2023.72.29.003
- Chesalov, S.M., Lion, Iu.A., Ptitsyn, V.V., Malozemov, A.V. Gabion filtration facilities for surface runoff treatment. Water Supply and Sanitary Technique. 2014. 9. Pp. 69–76.
- Obertas, D.S., Lagutin, A.A. Rain garden an alternative to rain cap. Vestnik landshaftnoy arkhitektury [Herald of Landscape Architecture]. 2024. 37. Pp. 74–78.

- 17. Poskalniuk, K.A. Overview of wastewater treatment facilities by phytoremediation. Symbol of science: international scientific journal. 2024. 3(5-1). Pp. 116–119.
- 18. Liu, Sh., Zhang, Ya., Feng, X., Pyo, S.H. Current problems and countermeasures of constructed wetland for wastewater treatment: A review. Journal of Water Process Engineering. 2024. 57. Pp. 104569. DOI: 10.1016/j.jwpe.2023.104569
- 19. Luo, Sh., Zhao, J., Zhang, Sh., Yang, M., Fang, X., Xu, B., Han, J. A novel method for enhancing nitrogen removal from wastewater treatment plant tailwater by zeolite-supported nano zero-valent iron substrate constructed wetland. Desalination and Water Treatment. 2024. 317. Pp. 100128. DOI: 10.1016/j.dwt.2024.100128
- Ofiera, L.M., Bose, P., Kazner, Ch. Removal of heavy metals and bulk organics towards application in modified constructed wetlands using activated carbon and zeolites. Water. 2024. 16(3). Pp. 511. DOI: 10.3390/w16030511
- 21. Zhang, X., Li, Ch., Yao, D., Hu, X., Xie, H., Hu, Zh., Liang, Sh., Zhang, J. The environmental risk assessment of constructed wetlands filled with iron and manganese ores in typical antibiotic treatment. Environmental Research. 2024. 240. Pp. 117567. DOI: 10.1016/j.envres.2023.117567
- Jain, N., Yadav, Sh., Taneja, S., Ray, S., Haritash, A.K., Pipil, H. Phosphate removal from urban stormwater runoff using Canna lily and Cyperus alternifolius-based bioretention system. Sustainable Water Resources Management. 2024. 10(2). Pp. 65. DOI: 10.1007/s40899-024-01076-5
- 23. Choi, H., Geronimo, F.K., Jeon, M., Kim, L.H. Evaluation of bacterial community in constructed wetlands treating different sources of wastewater. Ecological Engineering. 2022. 182. Pp. 106703. DOI: 10.1016/j.ecoleng.2022.106703
- 24. Choi, H., Jeon, M., Geronimo, F.K., Kim, L.H., Min, J.H. Evaluation of the performance of nature-based constructed wetlands for treating wastewater from various land uses in Korea. Water. 2024. 16(3). Pp. 381. DOI: 10.3390/w16030381
- Hess, K.M., Sinclair, Ja.S., Reisinger, A.J., Bean, E.Z., Iannone, III B.V. Are stormwater detention ponds protecting urban aquatic ecosystems? A case study using depressional wetlands. Urban Ecosystems. 2022. 25(4). Pp. 1155–1168. DOI: 10.1007/s11252-022-01208-9
- Philippe, M., Le Pape, P., Resongles, E., Landrot, G., Freydier, R., Bordier, L., Baptiste, B., Delbes, L., Baya, C., Casiot, C., Ayrault, S. Fate of antimony contamination generated by road traffic – A focus on Sb geochemistry and speciation in stormwater ponds. Chemosphere. 2023. 313. Pp. 137368. DOI: 10.1016/j.chemosphere.2022.137368
- 27. Martirosyan, O.V. Dispute about the shungite. Zapiski Rossiyskogo mineralogicheskogo obshchestva [Notes of the Russian Mineralogical Society]. 2022. 151(3). Pp. 123–132. DOI: 10.31857/S0869605522030066
- Terebova, E.N., Oreshnikova, N.V., Pavlova, M.A., Starodubtseva A.A. Application of scots pine bark and shungite chips for growing oats (Avena sativa L.) in protected ground. Lesnoy Vestnik / Forestry Bulletin. 2024. 28(2). Pp. 55–69. DOI: 10.18698/2542-1468-2024-2-55-69
- 29. Shibaeva, T.G., Sherudilo, E.G., Pervunina, A.V., Kirilyuk, S.D., Titov, A.F. On the effect of shungites on plant growth development. Transactions of the Karelian Research Centre of the Russian Academy of Scinces. 2022. 7. Pp. 13–27. DOI: 10.17076/eb1641
- Sidorova, V.A., Yurkevich, M.G. Use shungite when growing potatoes. Agrochemical herald. 2022. 6. Pp. 43–48.
 DOI: 10.24412/1029-2551-2022-6-008
- 31. Sukhinina, N.S., Khodos, I.I., Zverkova, I.I., Turanov, A.N., Karandashev, V.K., Yemelchenko, G.A. Strukturnyye osobennosti i sorbtsionnyye svoystva mezoporistogo uglerodnogo materiala, poluchennogo iz prirodnogo shungita [Structural features and sorption properties of mesoporous carbon material obtained from natural shcungite]. Neorganicheskiye materialy [Inorganic materials]. 2022. 58(10). Pp. 1151–1159. DOI: 10.31857/S0002337X22100141
- 32. Gibadullina, N.N., Badamshin, A.G., Sunagatova, E.M., Guba, A.S. Environmentally friendly sorbent for oil spill response. Chemical Safety Science. 2023. 7(1). Pp. 103–115. DOI: 10.25514/CHS.2023.1.24008
- 33. Buz'ko, V.Yu., Ivanin, S.N., Shutkin, I.Yu., Goryachko, A.I., Udodov, S.A., Ozolin, A.V. Atomic composition, microstructure, and electromagnetic properties of schungite micropowder. Condensed Matter and Interphases. 2023. 25(1). Pp. 3–13. DOI: 10.17308/kcmf.2023.25/10970
- 34. Smirnova, E.V., Okunev, R.V., Giniyatullin, K.G. Influence of carbon sorbents on the potential ability of soils to self-cleaning from petroleum pollution. Georesursy [Georesources]. 2022. 24(3). Pp. 210–218. DOI: 10.18599/grs.2022.3.18
- 35. Vyrodova, K.S., Yadykina, V.V. The use of shungite to improve the quality of polymer-bitumen binder and asphalt concrete. Regional Architecture and Engineering. 2024. 2(59). Pp. 89–99. DOI: 10.54734/20722958_2024_2_89
- Kovaleva, E.I., Perebasova, P.M., Avdulov, D.A., Ladonin, D.V., Trofimov, S.Ya. The efficacy of ameliorants for remediation of soils contaminated with heavy metals, in a lab experiment. Lomonosov Soil Science Journal. 2024. 79(2). Pp. 105–118. DOI: 10.55959/MSU0137-0944-17-2024-79-2-105-118
- 37. Petrova, E.V., Obukhova, A.V., Gukovich, R.K., Otmakhov, V.I., Babenkov, D.E. Study of natural minerals as sorbents for drinking water treatment. Tomsk State University Journal of Chemistry. 2022. 26. Pp. 17–31. DOI: 10.17223/24135542/26/2
- Musina, U.Sh. Ecological properties of shale shungit in cleaning waste water of different technogenic origin. Sovremennyye
 problemy nauki i obrazovaniya [Modern problems of science and education]. 2015. 2-2. Pp. 12.
- 39. Tremasova, A.M., Larina, Yu.V. Shungit and zeolite for wastewater disposal. Scientific Notes Kazan Bauman State Academy of Veterinary Medicine. 2020. 243(3). Pp. 257–261. DOI: 10.31588/2413-4201-1883-243-3-257-261
- 40. Beryoza, I.G., Bryushkovskaya, T.S., Balakireva, K.A., Avanesova, T.P. The use of natural sorbents in the ship water purification equipment. Marine Intellectual Technologies. 2018. 1-1(39). Pp. 95–99.
- 41. Shchetinskaya, O.S., Soboleva, O.A. Ochistka stochnykh vod ot soyedineniy khroma s pomoshchyu shungita [Treatment of wastewater from chromium compounds using shcungite]. Herald of Technological University. 2017. 20(20). Pp. 128–132.
- 42. Matrosova, L.E., Tremasova, A.M., Tarasova, E.Yu., Erokhondina, M.A., Potekhina, R.M., Makayeva, V.I. Application of shungite for cleaning poultry wastewater. Scientific Notes Kazan Bauman State Academy of Veterinary Medicine. 2021. 247(3). Pp. 137–140. DOI: 10.31588/2413-4201-1883-247-3-137-140
- 43. Fomenko, A.I. Adsorption of iron cations from aqueous solutions by mineral sorbents. Voda: khimiya i ekologiya [Water: chemistry and ecology]. 2023. 10. Pp. 22–28. DOI: 10.58551/20728158_2023_10_22
- 44. Fomenko, A.I. Adsorption treatment of wastewater from phosphates. Voda: khimiya i ekologiya [Water: chemistry and ecology]. 2024. 3. Pp. 58–65.

- 45. Alekseyev, M.I., Kurganov, A.M. Organizatsiya otvedeniya poverkhnostnogo (dozhdevogo i talogo) stoka s urbanizirovannykh territoriy: uchebnoye posobiye [Organization of drainage of surface (rain and melt) runoff from urbanized areas: education guidance]. Moscow: Izd-vo ASV, 2000. 352 p.
- 46. Muslov, S.A., Zaytseva, N.V., Samosadnaya, I.L., Gavrilenkova, I.V. Three methods of measuring the area of plan figures of arbitrary form by program methods. International Journal of applied and fundamental research. 2017. 5-1. Pp. 89–93.
- 47. Chugayev, R.R. Gidravlika: uchebnik dlya vuzov [Hydraulics: textbook for universities]. 4-ye izd., dop. i pererab. Leningrad: Energoizdat. Leningr. otd-niye, 1982. 672 p.
- 48. Venetsianov, Ye.V., Rubinshteyn, R.N. Dinamika sorbtsii iz zhidkikh sred [Dynamics of sorption from liquid media]. Moscow: Nauka, 1983. 237 p.
- 49. Smirnov, A.D. Sorbtsionnaya ochistka vody [Sorption water treatment]. Leningrad: Chemistry. Leningr. otd-niye, 1982. 168 p.
- 50. Korchevskaya, A.M., Chechevichkin, V.N. Kharakteristiki sorbtsionnogo modulya gidrotekhnicheskogo sooruzheniya ochistki livnevykh stochnykh vod kladbishch [Characteristics of the sorption module of a hydraulic engineering structure for the treatment of stormwater runoff from cemeteries]. Magazine of Civil Engineering. 2009. 2(4). Pp. 43–45.
- 51. Leontiev, N.E. Fundamentals of fluid flows through porous media. Moscow: MAKS Press, 2017. 88 p.

Information about the authors:

Galina Kozinetc, Doctor of Technical Sciences ORCID: https://orcid.org/0000-0002-6877-8420

E-mail: kozinets gl@spbstu.ru

Victor Chechevichkin, PhD of Chemical Sciences ORCID: https://orcid.org/0009-0007-2285-3337

E-mail: chechevichkin vn@spbstu.ru

Mikhail Tryaskin,

E-mail: tryaskin ma@spbstu.ru

Aleksei Chechevichkin,

ORCID: https://orcid.org/0009-0002-2340-8693

E-mail: chechevichkin av@spbstu.ru

Leonid Yakunin,

ORCID: <u>https://orcid.org/0009-0007-3277-5037</u>

E-mail: yakunin la@spbstu.ru

Received 23.10.2024. Approved after reviewing 10.12.2024. Accepted 12.12.2024.



Magazine of Civil Engineering

ISSN 2712-8172

journal homepage: http://engstroy.spbstu.ru/

Research article UDC 69.04

DOI: 10.34910/MCE.132.2



Bearing capacity of lightweight steel concrete enclosure wall panels

V.A. Rybakov¹ , K. Usanova¹ , A.V. Seliverstov², A.A. Kislitcyna¹, A.A. Tsvetkova¹, S.V. Akimov¹

☑ fishermanoff@mail.ru

Keywords: lightweight steel concrete enclosure wall panels, fastenings, bearing capacity, self-tapping screw

Abstract. The object of this study is lightweight steel concrete enclosure wall panels consisting of light gauge steal profiles and foam lightweight cellular concrete filling in general and, in particular, their fastenings. The purpose of this study is to develop a methodology for calculating enclosure wall LSCS panels with partial resting on floor slabs fastened with self-tapping screws of the Harpoon type. Methods. The experimental study of behaviour of the sample of the LSCS panel fastened via galvanized plate with self-tapping screws to a metal tube, the rigidity of which is many times higher than the rigidity of the LSCS panel, from the action of a distributed load simulating wind pressure, is carried out. The density of foam concrete of the panel was measured during experiment and amounted to 370 kg/m3. Results. The methodology of calculating the bearing capacity of LSCS panel-to-slab fastenings is proposed and substantiated. The analytically calculated destructive load 28.25 kN is 9.3 % less than experimentally obtained destructive load 30.9 kN. It is shown that the loss of load-bearing capacity of the panel happens due to bearing of the steel sheet of the web of the light gauge steel profile of the panel. It is shown that the rigidity of the LSCS panel fastenings varies from the one corresponding to the fixed-support calculation scheme to the one corresponding to the hinged-support calculation scheme. The behaviour of the panel corresponds to the fixed-support calculation scheme before the load is 30 % of the value that gives the maximum allowable deflection, then the fasteners work as a finite stiffness support and turn into a plastic hinge when the load reaches 90 % of the abovementioned load. It is proposed to use the hinged-support calculation scheme in design practice.

Funding: The research was carried out with the support of the Russian Science Foundation grant, https://rscf.ru/project/23-29-00564/

Citation: Rybakov, V.A., Usanova, K., Seliverstov, A.V., Kislitcyna, A.A., Tsvetkova, A.A., Akimov, S.V. Bearing capacity of lightweight steel concrete enclosure wall panels. Magazine of Civil Engineering. 2024. 17(8). Article no. 13202. DOI: 10.34910/MCE.132.2

1. Introduction

Energy efficiency concerns are critical in modern construction, and therefore, the choice of an optimal wall structure plays an important role.

The most common technologies for producing enclosing structures can be divided into prefabricated structures and those constructed on site. The main disadvantage of structures built directly on site is the low speed of erection. Prefabricated structures are free from this disadvantage: prefabricated reinforced concrete panels, sheathed cold-formed steel (CFS) panels, and lightweight steel-concrete structural panels

© Rybakov, V.A., Usanova, K., Seliverstov, A.V., Kislitcyna, A. A., Tsvetkova, A.A., Akimov, S.V., 2024. Published by Peter the Great St. Petersburg Polytechnic University.

¹ Peter the Great St. Petersburg Polytechnic University, St. Petersburg, Russian Federation

² LLC "Sovbi", St. Petersburg, Russian Federation

(LSCS panels), consisting of LSCS (lightweight steel concrete structures). Thanks to factory assembly of panels, the labour intensity of their installation is reduced by 60% compared to the labour intensity of installing, for example, ventilated facades [1]. Moreover, prefabricated structures help reduce heating and cooling costs of the building [2].

External reinforced concrete wall panels typically consist of three layers: a load-bearing reinforced concrete layer, a middle thermal insulation layer, and an external protective reinforced concrete layer. The panels are connected to each other through embedded parts by welding or using key joints on reinforcement bar protrusions. High speed and low cost of construction as well as low cost of interior decoration due to smooth-faced walls make this technology attractive [3]. However, the low thermal insulation capacity of reinforced concrete, its high specific weight requiring the use of a crane, are obstacles to the use of this type of enclosing structures in low-rise construction.

Another type of enclosing structure is sheathed CFS panels – a multilayer structure consisting of a frame filled with insulation and clad with facing sheets [4]. One of the significant disadvantages of frame-sheathed walls is the flammability of mineral wool insulation, which reduces the fire resistance of the wall panel and limits the scope of application for this type of enclosing structure.

The third type of prefabricated structures is LSCS panels, consisting of light gauge steel profiles (LGSPs) and foam lightweight cellular concrete (LCC). The Fig. 1 shows a drawing of one type of this panel. These structures can serve both load-bearing and enveloping functions in buildings and are free from the aforementioned disadvantages. Construction of a two-story house from LSCS panels takes only 15 days. Photo on Fig. 2 shows a detached residential house made from LSCS panels on the 5th and 15th day of construction.

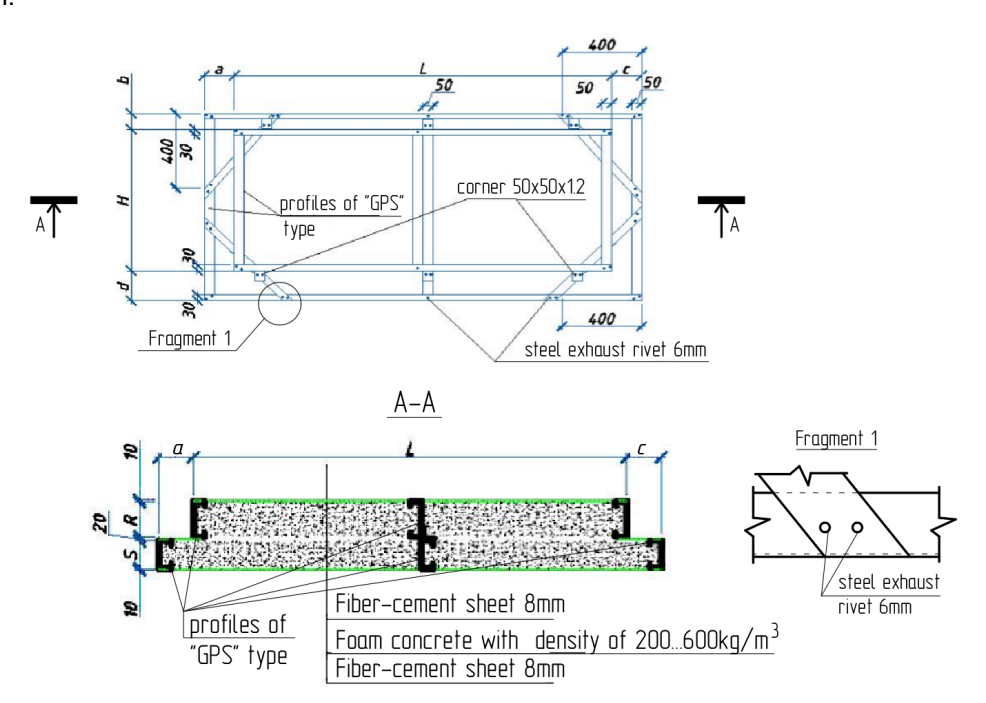


Figure 1. Composition of the wall panel and the general view.



Figure 2. a) Mounted panels of a LSCS house on the 5th day of construction; b) Finished house on the 15th day of construction.

The LSCS were described for the first time in [5]. It is based on constructing a structure from lightweight thin-walled steel profiles and filling the space between them with foam LCC .Prefabricated LSCS panels are a specific case of a structure built using LSCS technology.

When concrete and steel structures work together, the combined properties of the system exceed the sum of the individual properties of concrete and steel considered separately. This phenomenon is observed under various types of stress-strain conditions, such as deformations caused by temperature changes [6], cyclic loading [7], concentric [8, 9] and eccentric [10] compression, and bending [11].

Concrete, when working in combination with the steel structure, significantly increases both its local and overall stability [12, 13]. The fact of increased stability in composite LGS structures is also substantiated in the experimental study in [14], where the compressed chord of LGS truss was filled with concrete. Similarly, Jiqin Wang and his research team [15] conducted experimental studies on LGS and foam concrete panels under cyclic loading.

It has been experimentally proven that foam concrete, despite its extremely low strength class, actually contributes to structural performance, preventing effects, such as local buckling, failure, and warping of the steel profile elements [16]. Additionally, it increases the overall load-bearing capacity of the flooring by 20–25 % [5]. Study [17] established that the shear strength of a lightweight concrete sample is approximately the same as that of a sample made from regular concrete.

Foam concrete in the structure serves as a thermal and sound insulation material [18], and due to its adhesion to steel, it increases the load-bearing capacity of LGS profiles, preventing profile distortion and ensuring that there is no cross-sectional warping or bimoment, which are integral factors to the mechanics of thin-walled members and often lead to a twofold increase in stresses in the structure. In previous studies, the authors confirmed that the use of foam concrete allows for an increase in the structural performance factor [19]. Similar results were obtained for LGS profiles sheathed with oriented strand boards (OSBs) in [20].

The advantages of composite steel and concrete structures include improved fire resistance compared to steel structures [21–23], reduced steel intensity [24], and increased corrosion resistance [25].

However, in the regulatory documentation governing the use of LGS profile fasteners, there are no recommendations for calculating the fastening of LSCS panels to the load-bearing frame of the building, despite the practicality of using this type of structure, which complicates their design. Some studies, for example [26], reveal that failure of self-tapping screws is the most probable cause of LSCS structural failure. However, there are very few publications in the scientific literature specifically dedicated to the bearing capacity of self-tapping screws in LSCS [27, 28]. The few existing studies [29, 30], and [31] focus on the use of self-tapping screws for fastening LGS profiles to each other.

In light of the above, the aim of this study was formulated: to develop a method for calculating enclosure wall LSCS panels with partial resting on floor slabs fastened with self-tapping screws. To achieve this aim, the following tasks were set:

- 1. Experimental determination of behavior, load-bearing capacity and deflections of a sample of LSCS panel with density of foam concrete 370 kg/m³.
- 2. Analytical calculation of the load-bearing capacity of self-tapping screws fastening LSCS panels.
- 3. Calculation of the deflections of LSCS panels for both hinged and rigidly fixed panel supports.
- 4. Assessment of the impact of the fasteners on the calculation scheme.

2. Materials and Methods

Fig. 3 shows a constructive solution of supporting the enclosing wall panels on the building's load-bearing structures.

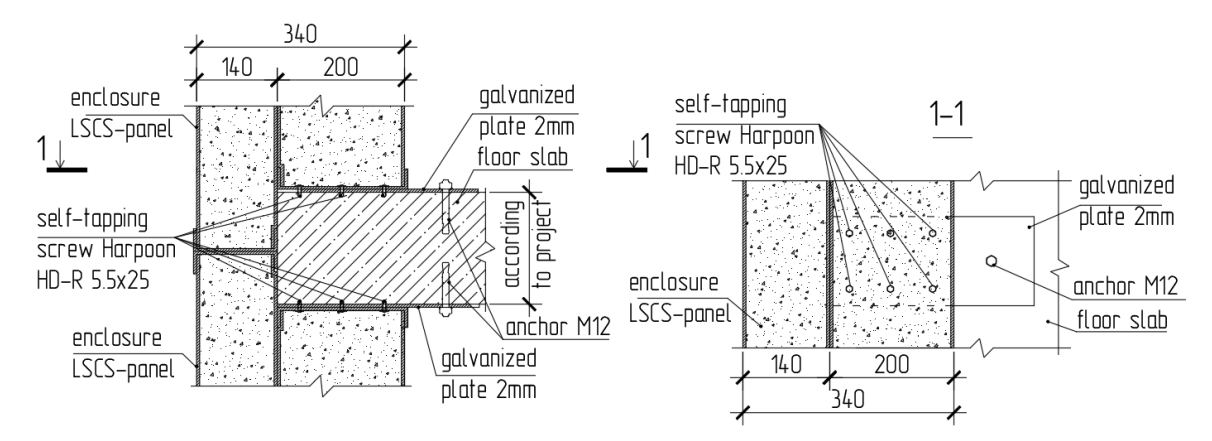


Figure 3. Fastening of the LSCS panel to a floor slab.

Let us model this type of panel support in an experimental study with the following assumption:

- the actual structure is analogous to the tested sample, preserving a 1:10 thickness-to-length ratio;
- the stiffness of the floor slab significantly exceeds that of the LSCS panel. Therefore, for the purposes of testing, the complex-to-manufacture floor slab will be replaced with a 150×150×8 mm profile steel tube;
- due to the constraints of the experimental setup, the test will be performed on a sample measuring 1500×360×170 mm, rather than a full-size panel.

Here is the description of the most important parts of the tested sample:

- self-tapping screws Harpoon HD-R 5.5x25 produced according to Organization Standard STO 0065-83135335-2014 Self-Tapping and Self-Drilling Screws for Wall and Roof Mounting Structures Made of Light Gauge Steel (https://www.snabmetiz.ru/UserFiles/Image/_Docs/STO_0065-2014_Harpoon.pdf) to fix the panel to the 150×150×8 profile steel tube;
- 2 pieces of galvanized mounting plates 120×290×2 mm made of steel with yield stress 275 MPa to fix the panel to the 150×150×8 mm profile steel tube;
- fiber-cement sheets 1500×360×8 mm at both sides of the panel;
- the LSCS frame of the panel made of "GPS-type" profiles 150×50×1.5 mm and filled with foam concrete with the density of 370 kg/m³;
- steel exhaust rivets to fix the elements of the LSCS frame to each other.

The sample was suspended from mounting plates attached to the load-bearing components of the setup and subjected to 4 forces spaced 300 mm apart, which can be considered as an approximation of a distributed load simulating wind pressure.

Here is the description of the most important parts of the experimental setup:

- channel bar 120 mm high, 650 mm long;
- channel bar 120 mm high, 400 mm long, 2 pieces;
- concrete prisms 360×100×100 mm with the density of 2500 kg/m³, 4 pieces;
- wood block filler 360×100×25 mm placed under concrete prisms to prevent local deformation of the steel profile under compression, 4 pieces;
- flexometers, 4 pieces, were placed in the middle of the panel and near the supports;
- hydraulic jack;
- hand-force hydraulic pump;
- dynamometer.

Table 1 shows the characteristics of the equipment.

Table 1. Equipment used for LSCS panel testing.

No	Designation of equipment	Brand	Vendor
1	Hydraulic equipment loading		
	Universal single-sided jack 50 tnf-150 mm	Enerpred	JSC Industrial group Hydromechanics
	Hand-force hydraulic pump 2 l	Enerpred	JSC Industrial group Hydromechanics
2	Compression dynamometer	Stroypribor	LLC Stroypribor
3	Flexometer	Stroypribor	JSC Industrial group Hydromechanics

Fig. 4 shows the configuration of the sample and the experimental setup. The total weight of the distribution system was 1.02 kN.

The tests were conducted on five panel samples.

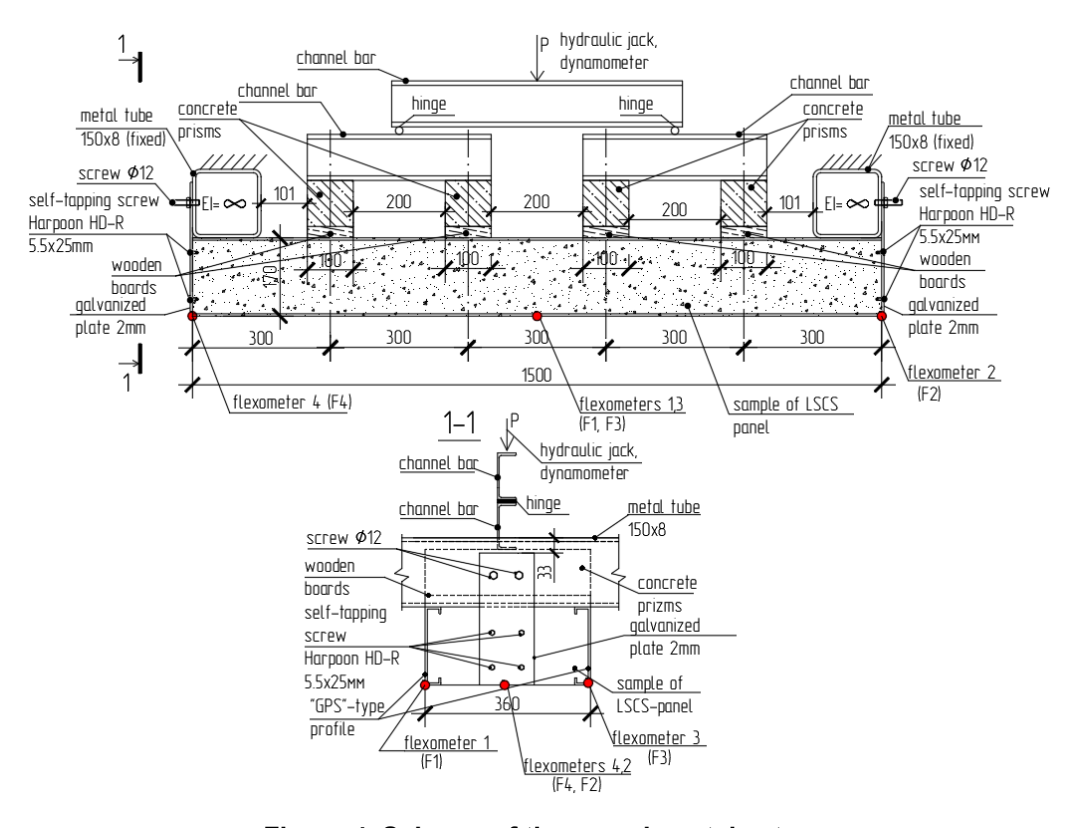


Figure 4. Scheme of the experimental setup.

The loading scheme adopted in the experimental study of the LSCS panel is shown in Fig. 5.

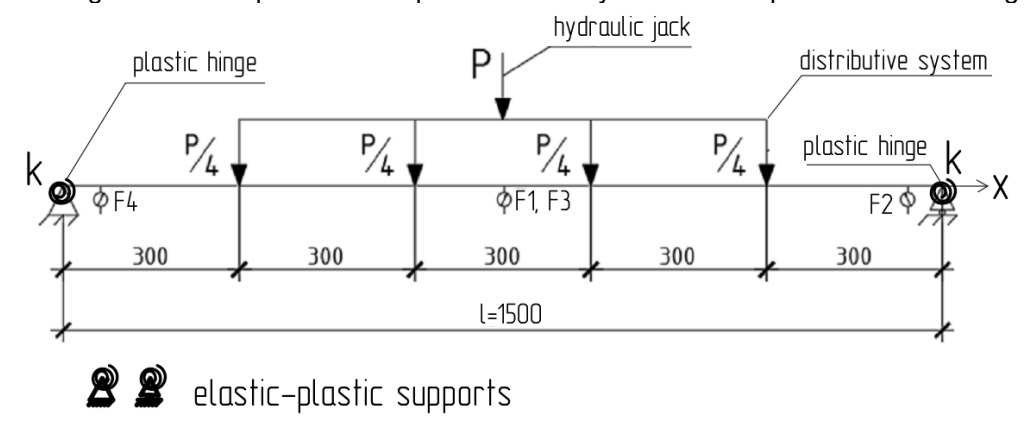


Figure 5. Loading scheme.

Photographs of the experiment and the fastening node before load application are presented in Figs. 6 and 7.

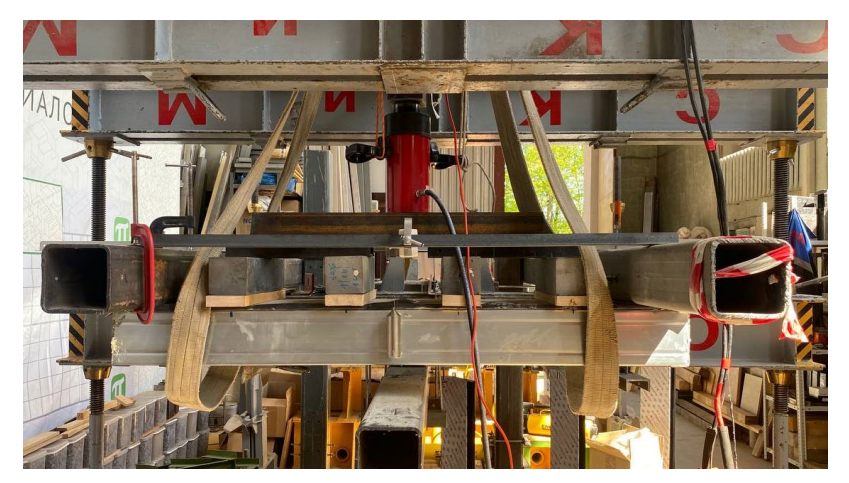


Figure 6. Experimental setup before the start of the test.

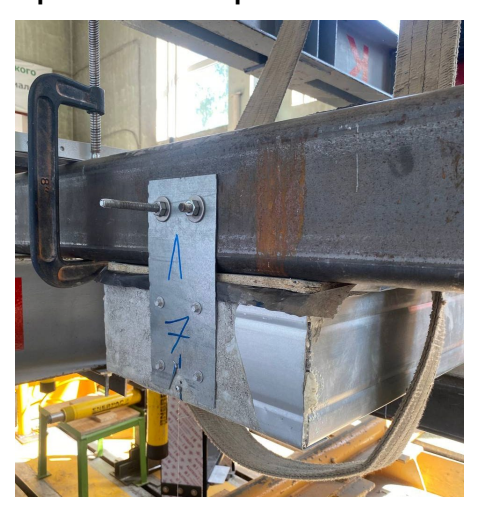


Figure 7. Fastening of the panel before the start of the test.

3. Results and Discussion

Figs. 8 and 9 show the nature of the sample failure.

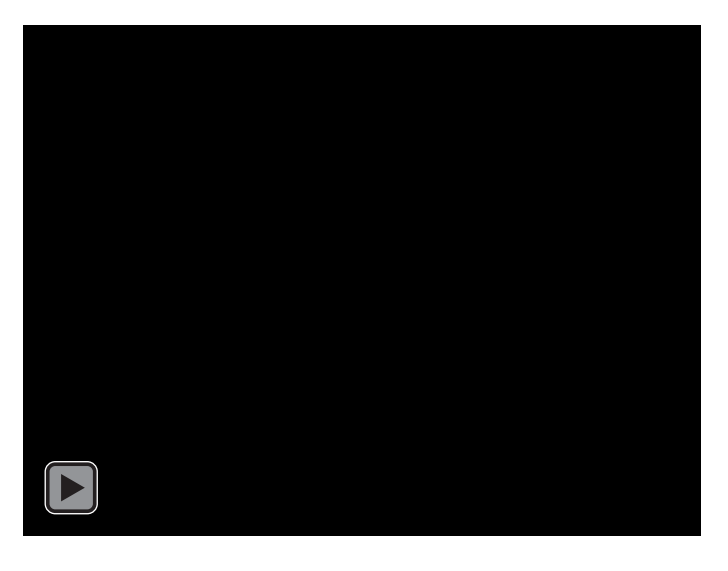


Figure 8. The process of the fastening of the panel failure. Side view. (For watching the video open the PDF in Adobe Acrobat and allow multimedia and 3D content.

DOI: https://doi.org/10.18720/SPBPU/2/VIDEO/z24-21).



Figure 9. The process of the fastening of the panel failure. Front view. (For watching the video open the PDF in Adobe Acrobat and allow multimedia and 3D content.

DOI: https://doi.org/10.18720/SPBPU/2/VIDEO/z24-20).

Table 2 shows values of the destructive loads for each sample.

Table 2. Destructive load values.

Sample designation	Destructive loads, kN
Panel No 1	31.39
Panel No 2	31.39
Panel No 3	31.39
Panel No 4	33.35
Panel No 5	27.47
Panel No 6	30.41
Average destructive load	30.9

Let us compare the value of the destructive load for the fasteners obtained in the experiment with the values of the destructive load calculated according to STO 0065-2014.

There are three types of connection failures for self-tapping screws subjected to shear:

- sheet bearing;
- sheet tearing along the net section;
- screw shear.

Let us determine the connection strength for each of the three types of connection failures.

The bearing strength of the base material by the screw is calculated by using formula (1):

$$F_b = \frac{\gamma_c \cdot \alpha \cdot R_{un}}{\gamma_m \cdot d \cdot t},\tag{1}$$

where F_b is design bearing strength of the base material; R_{un} is ultimate tensile strength of the base material in which the screw is installed; γ_m is safety factor for material strength equal to 1.25; γ_c is condition load effect factor equal to 0.8; t is thickness of the thinner of the connected sheets; d is nominal diameter of the screw, α is coefficient depending on the thickness ratio of the connected sheets and equal to 1.76.

Shear strength of the screw is calculated using formula (2):

$$F_{v} = \gamma_{c} \cdot \frac{F_{vn}}{\gamma_{m}},\tag{2}$$

where F_{v} is design shear strength of the screw; F_{vn} is screw strength according to the manufacturer's standard; γ_{m} is safety factor for material strength equal to 1.3; γ_{c} is condition load effect factor equal to 0.8.

Tensile strength of the sheet along the net section is determined using formula (3):

$$F_t = \gamma_c \cdot \frac{R_{yn}}{\gamma_m} A_{netto}, \tag{3}$$

where F_t is design tensile strength of the sheet along the net section; R_{yn} is yield strength of the material in which the self-tapping screw is installed; γ_m is safety factor for material strength equal to 1.25; γ_c is condition load effect factor equal to 0.9; A_{netto} is net section area of the connected elements.

Table 3 shows the results of the calculation.

Table 3. Destructive load for one self-drilling screw.

Type of connection failure	Destructive load per screw, kN			
Sheet bearing	28.25			
Sheet tearing along the net section	151.08			
Screw shear	40.63			

As we can see, the minimum destructive load for this fastener is the load that leads to the bearing failure of the sheet material. It amounts to 28.25 kN, which is 9.3 % less than 30.9 kN, the average destructive load according to the experimental results. The difference in the results is explained by the safety factors in the calculation formula. Thus, this method for determining the strength of the LSCS panel fastening to the floor slab can be considered reliable.

3.1. Displacements in the span

Deflections of the panel are determined as the difference between the average readings of deflectometers T1, T3, installed in the middle of the span, and deflectometers T2, T4, installed near the supports.

Let us analytically determine displacements for the hinged (Figs. 10, 11) and fixed on both ends (Fig. 12) calculation models.

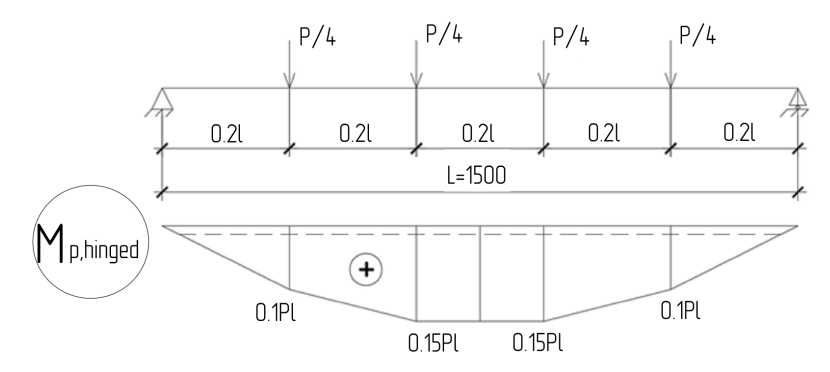


Figure 10. Bending moments in the hinged calculating model.

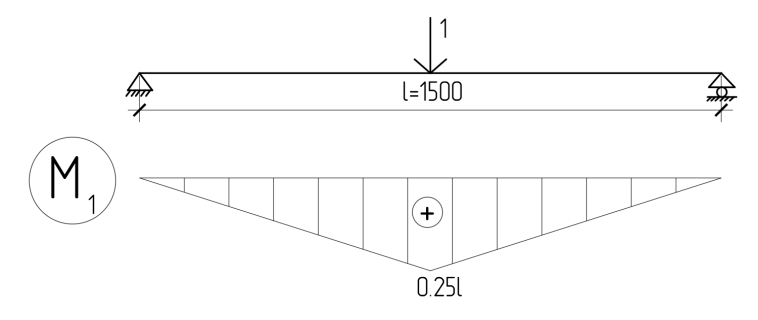


Figure 11. Auxiliary loading.

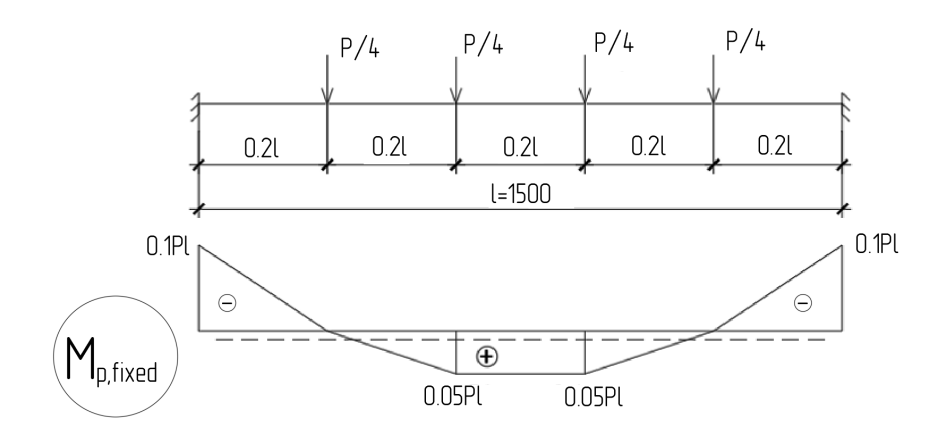


Figure 12. Bending moments in the rigidly fixed calculation model.

Displacements in the hinged model are determined by integration (4):

$$d_{hinged} = \int_{0}^{l} \frac{M_{p,hinged} M_1}{EI} dx = 0.01575 \frac{Pl^3}{EI},$$
 (4)

where $M_{p, hinged}$ is shown on Fig. 9, M_1 is shown on Fig. 10.

The Maxwell–Mohr integral (4) is obtained by multiplying the $M_{p,hinged}$ epure (Fig. 10) and M_1 (Fig. 11) using the Simpson formula (formula of parabolic trapezoids).

The bending stiffness of the beam is determined as the sum of the bending stiffnesses of the thin-walled profile and the foam concrete is determined by the formula (5):

$$EI = E_b I_b + E_s I_s = 691 \cdot \text{kN} \cdot \text{m}^2, \tag{5}$$

where E_b = 843 MPa – modulus of elasticity of the panel is taken according to Organization Standard (LLC Sovbi, Russian Federation) STO 06041112.002-2018 "Steel-Concrete structures made of thermal insulation non-autoclave foam concrete profile steel cladded with fiber cement sheets" (STO 06041112.002-2018), a density of 370 kg/m³, determined by weighing the panels after the experiment; I_b = 1.47·10⁴cm⁴ – moment of inertia of the panel; E_s = 2.1·10⁵ MPa – modulus of elasticity of steel; I_s = 282 cm⁴ – moment of inertia of two GPS-type profiles fabricated according to STO 06041112.002-2018. This document was developed on the basis of the research, conducted by us in 2018-2023 years [5, 21, 25].

Similarly, we obtain the formula for determining the displacements in the middle of the span in the fixed-supports model through integration (6):

$$d_{fixed} = \int_{0}^{l} \frac{M_{p,fixed} M_1}{EI} dx = 0.00325 \frac{Pl^3}{EI},$$
 (6)

where $\boldsymbol{M}_{p, hinged}$ is shown on Fig. 12, \boldsymbol{M}_1 is shown on Fig. 11.

The Maxwell–Mohr integral (6) is obtained by multiplying the $M_{p,hinged}$ epure(Fig. 12) and M_1 (Fig. 11) using the Simpson formula (formula of parabolic trapezoids).

For the nonrigid fastening of the walls of a multi-storey building within one floor, the maximum horizontal deflection of the concerned panel as of a separate structural element is calculated by formula (7):

$$f_u = \frac{h_s}{300} = \frac{1500}{300} = 5 \text{ mm},$$
 (7)

where $h_{\rm s}$ – the hight of the storey (in our research it is the length of the panel l=1500 mm).

The stresses in the tested sample were found to be 200 MPa for the hinged system and 65 MPa for rigidly fixed system, and they do not reach the yield strength of the steel which equals 220 MPa. The limitation of the profile operation happens due to exceeding the maximum deflection.

To conclude the study, let us examine the experimental deflection values and compare them with the calculated values. The results are presented in Fig. 13.

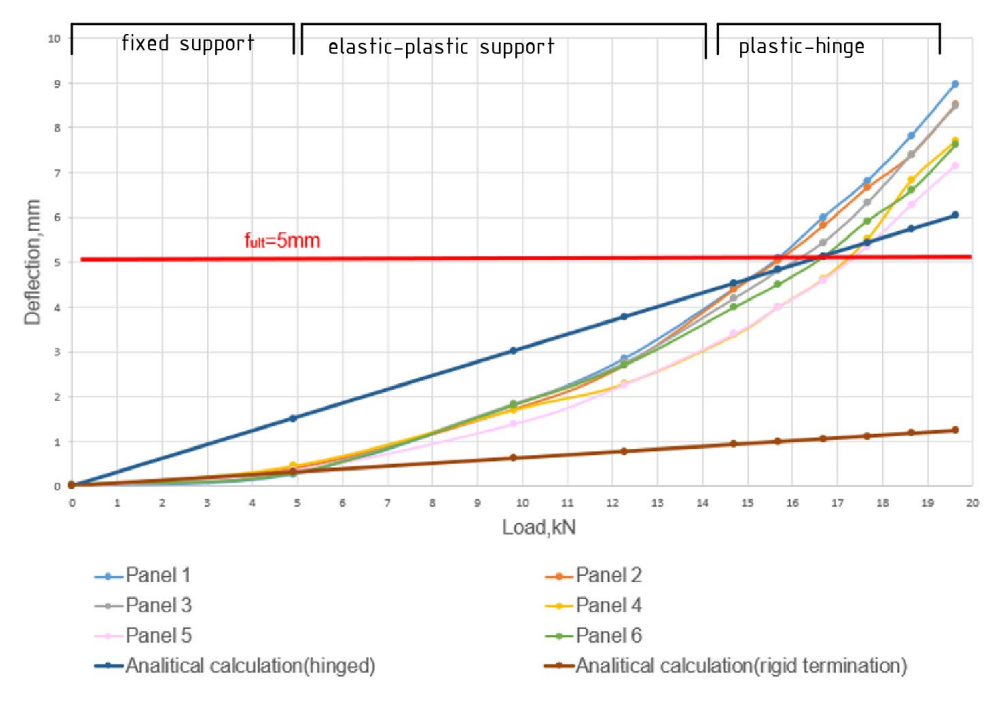


Figure 13. Deflection-load diagram.

We can observe a change in the behaviour of the panel. Initially, when the load is between 0 and 4.9 kN, the behaviour of the panel corresponds to that of a beam rigidly fixed on both ends. As the load increases, plastic hinges begin to form at the supports, and the behaviour of the specimen shifts toward that of a beam with hinged supports. Since the plastic hinges do not form instantaneously but over time, the behaviour of the structure changes gradually and is nonlinear. For the same reason, the deflection values of the panel from the applied load, as determined experimentally, are lower than those determined analytically for the hinged support case. The values start to correspond with the experimental results at a load of 16 kN, when the formation of plastic hinges in the fasteners is completed.

The maximum allowable deflection $f_{\mathcal{U}}$ = 5 mm is reached at a load ranging from 15.7 to 17.2 kN, which represents 50.8 to 55.7 % of the load-bearing capacity and corresponds to a deflection of 4.8 to 5.3 mm as determined analytically for the hinged support case, and a deflection of 1.0 to 1.1 mm as determined analytically for the rigid fixation case.

It is evident that the deflection values determined analytically for the rigid fixation case are significantly lower than the actual deflections in the structure. Therefore, it is recommended to perform an analytical calculation of the panel's deflections under external load for the hinged support case.

4. Conclusions

As a result of the study, the following outcomes were achieved:

- 1. It is shown that the loss of the load-bearing capacity of the panel happens due to bearing of the steel sheet of the web of the panel LGSP.
- 2. The method of calculating the bearing capacity of LSCS panel-to-slab fastenings is proposed and substantiated. The analytically calculated destructive load 28.25 kN is 9.3 % less than experimentally obtained destructive load 30.9 kN.
- 3. It is shown that the rigidity of the LSCS panel fastenings varies from the one corresponding to the fixed-support calculation scheme to the one corresponding to the hinged-support calculation scheme. The behavior of the panel corresponds to the fixed-support calculation scheme before the load is 30 % of the value that gives the maximum allowable deflection, than the fasteners work as

- an finite stiffness support and turn into a plastic hinge when the load reaches 90 % of the abovementioned load.
- 4. It is proposed to use the hinged-support calculation scheme in design practice.
- 5. The results of the research are implemented into the LLC "Sovbi" (Russian Federation, Saint Petersburg) activity.

References

- Danilov, N.D., Fedotov, P.A., Tretyakov, E.S., Gerasimova, V.S. Comparison of Options of Different Types of External Walls of Buildings. Zhilishnoye Stroitel'stvo [Housing Construction]. 2019. 5. Pp. 43–47. DOI: 10.31659/0044-4472-2019-5-43-47
- 2. Wasim, M., Wang, K., Yuan, Z., Jin, M., Abadel, A., Nehdi, M.L. An Optimized Energy Efficient Design of a Light Gauge Steel Building. Case Studies in Construction Materials. 2023. 19. Article no. e02398. DOI: 10.1016/j.cscm.2023.e02398
- 3. Efimchenko, M.I. Problems and Prospects of Modern Panel Housing Construction. Inzhenernyye Issledovaniya [Engineering Research]. 2022. 4(9). Pp. 17–25. URL: https://eng-res.ru/archive/2022/4/No9.pdf (date of application: 17.02.2025).
- Nazmeeva, T., Sivokhin, A. Stress-Strain State of Attachment Point of Curtain Frame Wall with Cladding on the Basis of Steel Cold-Bent Profile. Industrial and Civil Engineering. 2018. 10. Pp. 41–44. URL: http://www.pgs1923.ru/ru/index.php?m=4&y=2018&v=10&p=05 (date of application: 17.02.2025).
- 5. Rybakov, V., Kozinets, G., Vatin, N. Lightweight Steel Concrete Structures Technology with Foam Fiber-Cement Sheets. Magazine of Civil Engineering. 2018. 6(82). Pp. 103–111. DOI: 10.18720/MCE.82.10
- Wang, L., Yang, X.-J., Li, Z.-Q., Yin, P., Zhou, X.-F., Hu, Q. (2024) Experimental Study on the Interfacial Bonding Performance of Concrete-Filled Steel Tubes at Different Ambient Temperatures. Thin-Walled Structures, 205, 112368. DOI: 10.1016/j.tws.2024.112368
- Fan, J.-H., Wang, W.-D., Shi, Y.-L., Zheng, L. Low-Cycle Fatigue Behaviour of Concrete-Filled Double Skin Steel Tubular (CFDST) Members for Wind Turbine Towers. Thin-Walled Structures. 2024. 205(B). Article no. 112384. DOI: 10.1016/j.tws.2024.112384
- 8. Jamaluddin, N., Lam, D., Dai, X.H., Ye, J. An Experimental Study on Elliptical Concrete Filled Columns under Axial Compression. Journal of Constructional Steel Research. 2013. 87. Pp. 6–16. DOI: 10.1016/j.jcsr.2013.04.002
- 9. Dai, X., Lam, D. Numerical Modelling of the Axial Compressive Behaviour of Short Concrete-Filled Elliptical Steel Columns. Journal of Constructional Steel Research. 2010. 66(7). Pp. 931–942. DOI: 10.1016/j.jcsr.2010.02.003
- 10. Qiao, W., Zhang, X., Zhang, H., Zhang, L., Feng, H. Test Study on Eccentric Compression of Light Steel Concrete L-Shaped Composite Column in Modular Wall Prefabricated Building. Journal of Constructional Steel Research. 2024. 215. Article no. 108514. DOI: 10.1016/j.jcsr.2024.108514
- 11. Wang, X., Cheng, C., Wang, S., Wang, W. Study on the Flexural Behaviour of the Concrete Filled Square Steel Tube Beam with the Basic Magnesium Sulfate Cement-Based Composite Shell System. Construction and Building Materials. 2024. 424. Article no. 135968. DOI: 10.1016/j.conbuildmat.2024.135968
- 12. Cortés-Puentes, W.L., Palermo, D., Abdulridha, A., Majeed, M. Compressive Strength Capacity of Light Gauge Steel Composite Columns. Case Studies in Construction Materials. 2016. 5. Pp. 64–78. DOI: 10.1016/j.cscm.2016.08.001
- 13. Brian, Uy. Strength of Concrete Filled Steel Box Columns Incorporating Local Buckling. Journal of Structural Engineering. 2000. 126(3). Pp. 341–352. DOI: 10.1061/(ASCE)0733-9445(2000)126:3(341)
- Güldür, H., Baran, E., Topkaya, C. Experimental and Numerical Analysis of Cold-Formed Steel Floor Trusses with Concrete Filled Compression Chord. Engineering Structures. 2021. 234. Article no. 111813. DOI: 10.1016/J.ENGSTRUCT.2020.111813
- 15. Wang, J., Zhou, T., Wu, H., Guan, Y., Zhang, L. Cyclic Performance of Steel Frame Fabricated with Cold-Formed Steel Composite Wall Structure. Engineering Structures. 2022. 270. Article no. 114892. DOI: 10.1016/j.engstruct.2022.114892
- Chen, D., Wang, J., Pan, M., Zhou, J. Tests on Vertical Bearing Capacity of Steel-Foamed Concrete-Fiber Cement Pressure Plate Composite Walls. Shenyang Jianzhu Daxue Xuebao (Ziran Kexue Ban)/Journal of Shenyang Jianzhu University (Natural Science). 2018. 34(2). Pp. 275–285. DOI: 10.11717/j.issn:2095-1922.2018.02.10
- 17. Rassouli, B., Shafaei, S., Ayazi, A., Farahbod, F. Experimental and Numerical Study on Steel-Concrete Composite Shear Wall Using Light-Weight Concrete. Journal of Constructional Steel Research. 2016. 126. Pp. 117–128. DOI: 10.1016/j.jcsr.2016.07.016
- Yu, F., Kuang, G., Bu, S., Chen, L. Flexural Performance Tests and Numerical Analysis of Fabicated Light-Gauge Steel Reinforced Foam Concrete Filled Steel Mesh Formwork Wallboards. Structures. 2024. 66. Article no. 106813. DOI: 10.1016/j.istruc.2024.106813
- Rybakov, V. Condition Load Effect Factor of Profile Steel in Lightweight Steel Concrete Structures. Construction of Unique Buildings and Structures. 2020. 4(89). Article no. 8907. DOI: 10.18720/CUBS.89.7. 2023. 1(106). Article no. 10602. DOI: 10.4123/CUBS.106.2
- Xu, Y., Zhou, X., Shi, Y., Zou, Y., Xu, L., Xiang, Y., Ke, Ke. Lateral Resistance of OSB Sheathed Cold-Formed Steel Shear Walls. Thin-Walled Structures. 2021. 161. Article no. 107451. DOI: 10.1016/j.tws.2021.107451
- Rybakov, V., Seliverstov, A., Vakhidov, O. Fire Resistance of Lightweight Steel-Concrete Slab Panels under High-Temperature Exposure. E3S Web of Conference. 2021. 264. Article no. 02003. DOI: 10.1051/e3sconf/202126402003
- 22. Xiang, G., Song, D., Li, H., Zhou Y., Wang H., Shen G., Zhang, Z. Preparation of Steel Slag Foam Concrete and Fractal Model for Their Thermal Conductivity. Fractals. 2023. 7(8). Article no. 585. DOI: 10.3390/fractalfract7080585
- Kinoshita, T., Shintani, Y., Okazaki, T., Nishimura, T. Liew, J.Y.R. Effect of Steel-Fiber Reinforced Concrete on the Fire Resistance of Concrete-Filled Steel Tubular Columns under Simultanious Axial Loading and Double Curvative Bending. 11th International Conference on Structures in Fire (SiF2020). The University of Queensland. Brisbane, 2020. Pp.113–123. DOI: 10.14264/4767f7d
- 24. Zhuang, L.-D., Tao, M.-X., Zhao, J.-Z., Yang, K.-Y. Experimental and Numerical Investigations on the Mechanical Behaviour of Large-Span Circular Steel-Concrete Composite Slabs for Wind Power Tower. Thin-Walled Structures. 2024. 202. Article no. 112107. DOI: 10.1016/j.tws.2024.112107

- Rybakov, V., Seliverstov, A., Usanova, K. Steel Profile Corrosion Resistance in Contact with Monolithic Foam Concrete. E3S Web of Conferences. 2023. 365. Article no. 02001. DOI: 10.1051/e3sconf/202336502001
- Guan, Y., Zhou, X.-H., Shi, Y., Yao, X.-M. Experimental Study and Theoretical Analysis of Out-of-Plane and In-Plane Stiffness
 of Cold-Formed Thin-Walled Composite Floor. Gongcheng Lixue/Engineering Mechanics. 2023. 40(10). Pp. 21–32. DOI:
 10.6052/j.lssn.1000-4750.2022.01.0079
- 27. Yang, N., Bai, F., Liu, W., Ge, H. Unified Static-Fatigue Bearing Design Model for Self-Tapping Screw Joints in Light-Weight Steel Roofs under Typhoon Hazard I. Journal of Southeast University (Natural Science Edition). 2024. 54(1). Pp. 67–71. DOI: 10.3969/j.lssn.1001-0505.2024.01.009
- 28. Yang, N., Liu, W., Bai, F., Ge, H. Research on Time-Varying Reliability of Self-Tapping Screw Joints of Light-Weight Steel Roofs under Typhoon. Hunan Daxue Xuebao/Journal of Hunan University Natural Sciences. 2021. 48(11). Pp. 72–81. DOI: 10.16339/j.Cnki.Hdxbzkb.2021.11.008
- 29. Kurazhova, V.G., Nazmeeva, T.V. Node Connections of Cold-Formed Steel Structures. Magazine of Civil Engineering. 2011. 3. Pp. 47–52. URL: https://engstroy.spbstu.ru/userfiles/files/2011/3(21)/kurazhova_uzly.pdf (date of application: 17.02.2025).
- 30. Katranov, I.G. Tensile Testing and Calculation of Screw Joints of Light Thin-Walled Steel Structures. Vestnik MGSU [The Bulletin of Moscow State University of Construction]. 2010. 2. Pp. 89–93. URL: https://cyberleninka.ru/article/n/ispytaniya-i-raschet-vintovyh-soedineniy-legkih-stalnyh-tonkostennyh-konstruktsiy-na-rastyazhenie-1/viewer (date of application: 17.02.2025).
- 31. Wang, J., Qiu, Z., Liang, J. Experimental Investigations on the Lateral Performance of Foam Concrete Light Steel Keel Composite Wall. Journal of Building Engineering. 2023. 72. Article no. 106551. DOI: 10.1016/j.jobe.2023.106551

Information about the authors:

Vladimir Rybakov, Doctor of Technical Sciences ORCID: https://orcid.org/0000-0002-2299-3096

E-mail: fishermanoff@mail.ru

Kseniia Usanova, PhD in Technical Sciences ORCID: https://orcid.org/0000-0002-5694-1737

E-mail: plml@mail.ru

Anatoly Seliverstov,

ORCID: https://orcid.org/0000-0001-9735-9615

E-mail: sovbitex@mail.ru

Alexandra Kislitcyna,

ORCID: https://orcid.org/0000-0003-4310-2069

E-mail: alexandra.ak.13@gmail.com

Anna Tsvetkova,

ORCID: https://orcid.org/0000-0002-2993-6836

E-mail: annatsvetkova2014@mail.ru

Stanislav Akimov,

https://orcid.org/0000-0002-2908-4565

E-mail: akimov sv@spbstu.ru

Received 22.09.2024. Approved after reviewing 24.11.2024. Accepted 06.12.2024.



Magazine of Civil Engineering

ISSN 2712-8172

journal homepage: http://engstroy.spbstu.ru/

Research article UDC 639.42:539.42

DOI: 10.34910/MCE.132.3



Electrically conductive cement composites modified with weakly oxidized graphene

¹ North-Eastern Federal University, Yakutsk, Russian Federation

² V.P. Larionov Institute of the Physical-Technical Problems of the North of the Siberian Branch of the RAS, Yakutsk, Russian Federation

³ North-Eastern Federal University in Yakutsk, Yakutsk, Russian Federation

E.D. Vasileva¹ D.N. Popov^{1,2} , P.V. Vinokurov³ , A.L. Popov⁴

⁴ Institute of problems of oil and gas of the Siberian Branch of the Russian Academy of Sciences, Yakutsk, Russian Federation

⊠ vasilyeva_edm@mail.ru

Keywords: Concrete, cements, compressive strength, Portland cement, composite materials, multi-layer graphene oxide, cement composite, dispersion, self-diagnostics.

Abstract. This study investigates the influence of graphene on the electrical conductivity and mechanical properties of concrete composites, aiming to develop advanced materials for structural applications. Graphene's exceptional electrical conductivity can significantly enhance inert concrete matrices by forming a conductive network. Concrete samples were prepared with minimally oxidized graphene (MOG) at 0.2 and 0.5 % by weight of cement. Spectroscopic techniques, including Raman and infrared spectroscopy, were employed to characterize the interaction between graphene and the cement matrix. Results showed that the addition of MOG reduced electrical resistivity, with the 0.2 % sample decreasing from approximately 600 to 550 Ohm under compression. The yield point was around 40–50 kN, with a sharp decline in resistivity at this load. Compressive strength tests indicated a 48 % increase in strength with just 0.05 % graphene oxide. These findings suggest that graphene incorporation enhances both electrical conductivity and mechanical strength, making the composites suitable for applications in structural health monitoring and self-heating systems.

Funding: This study was supported by the Russian Science Foundation (project No. 24-21-20122).

Citation: Vasileva, E.D., Popov, D.N., Vinokurov, P.V., Popov, A.L. Electrically conductive cement composites modified with weakly oxidized graphene. Magazine of Civil Engineering. 2024. 17(8). Article no. 13203. DOI: 10.34910/MCE.132.3

1. Introduction

It is known that graphene has the highest electrical conductivity among known materials [1–4]. The addition of even a small amount of graphene can significantly increase the electrical conductivity of an initially inert dielectric concrete matrix due to the formation of a conductive network. A few works by authors, such as Sassani, Wang, Choi, Ghosh et al. [5–21, 26], are devoted to the study of the electrical properties of cement composites with the addition of graphene and graphene oxide, which show a sharp increase in electrical conductivity and the appearance of pronounced piezoresistive effects. The prospects for using such composites as self-sensing "smart" materials are discussed [27]. Such electrically conductive cement composites can be used in systems for heating road surfaces and airfields instead of traditional methods of removing ice and snow using chemicals. At the same time, in the study [7], the authors identified

© Vasileva, E.D., Popov, D.N., Vinokurov, P.V., Popov, A.L., 2024. Published by Peter the Great St. Petersburg Polytechnic University.

problems with the stability of electrical conductivity and energy consumption of heating systems based on carbon-cement composites during long-term operation.

The group of researchers [11–16] focused on studying the mechanical properties of graphene-cement composites. The addition of a small amount, from 0.1 to 1 %, by volume of carbon nanoparticles leads to a sharp increase in the electrical conductivity of cement composites by several orders of magnitude. Which is associated with the formation of a continuous conductive network through the cement matrix and also allows significantly improving the mechanical characteristics of cement composites by increasing compressive, tensile and flexural strength.

In the review works of Nochaiya and Schulte [17–18], the results of studies of graphene-cement composites are summarized, and the current state and application prospects in construction are analyzed. Various methods of dispersing graphene in a cement matrix are considered in detail – ultrasonic treatment, use of surfactants, and functionalization of graphene to improve wettability. The importance of obtaining a homogeneous and stable dispersion of graphene is shown.

Rostami [11] investigated the microstructure of composites using SEM, FTIR, XRD, TGA and revealed the effect of graphene on particle packing density, porosity reduction, change in hydrate composition, and acceleration of hydration processes. In the work of Li [20], an original approach is proposed for growing graphene directly on the surface of aggregates. This improves adhesion to the cement matrix while simultaneously imparting electrical conductivity.

The addition of carbon nanomaterials also improves the thermoelectric properties of cement composites by increasing the Seebeck coefficient [8–10, 14, 18, 24], which opens up ways for creating thermoelectric generators based on cement. Of particular interest are hybrid systems combining, for example, graphene and metal oxides, which make it possible to simultaneously increase electrical conductivity and the Seebeck coefficient. Oxidation of graphene improves its dispersion and adhesion to the cement matrix due to the formation of polar groups.

Du et al. and Konsta-Gdoutos [21–23, 4] considered the problem of the aggregation of graphene particles in the cement matrix, leading to heterogeneity and a decrease in the reinforcing effect. Solutions are proposed – the use of functionalized graphene as well as the application of graphene to the surface of aggregates.

For creating electrically conductive concretes, the selection of conductive additives is important, and for improving the stability and sensitivity of electrical characteristics to mechanical influences, the development of special composite concretes is required. Although the potential of graphene as a functional additive is very promising, the use of graphene concretes as "smart" materials for self-diagnostics is still at the research stage. The relevance of the work is due to the prospects for using such composites as self-sensing structural materials capable of monitoring stresses and strains during operation. This will improve the operational reliability and durability of concrete structures.

The aim of the work is to study the effect of graphene on the electrical conductivity of concrete composites, to determine the change in strength due to the inclusion of graphene, as well as to assess the potential for the use of graphene-modified concrete in various fields of mechanical engineering.

2. Methods

2.1. Spectroscopic Analysis and Microscopy

Raman spectroscopy, combined with atomic force microscopy (AFM) and confocal Raman/fluorescence microscopy and spectroscopy using the NTEGRA Spectra system, was employed to detect and identify graphene in concrete. This method allowed for the revelation of the interaction between graphene particles and the surrounding concrete matrix. Additionally, microphotographs and elemental analysis of the concrete surfaces were obtained using a scanning electron microscope (SEM) equipped with an EDS-WDS microanalysis system (JSM 6480LV INCA Energy 350, JEOL Ltd, Oxford Instruments, Japan, UK).

2.2. Preparation of Graphene-Modified Concrete

To experimentally confirm the use of an aqueous suspension of minimally oxidized graphene (MOG), obtained by electrochemical exfoliation of graphene as described in [28]. Minimally oxidized graphene (MOG) was obtained by electrochemical exfoliation in a 1.42 % aqueous sodium sulfate solution (Na₂SO₄). Two electrodes were used for this method: a gold electrode (6 mm wide and 0.015 mm thick) and a graphite electrode (ESA-16 grade with a diameter of 6 mm). The gold electrode acts as a cathode, and the graphite electrode acts as an anode. Both electrodes were immersed in 200 ml electrolyte to a depth of 60 mm, and the distance between them was 20 mm (Fig. 1, a). At a voltage of 12 V, the graphite electrode was

exfoliated for 60 minutes (Fig. 1, b). Then, using an ultrasonic homogeniser Up 200St (Hielscher Ultrasonics, Germany), large carbon particles were split into MOGs.



a



b

Figure 1. MOG synthesis: a – electrochemical exfoliation process; b – Electrochemical exfoliation process after 60 min.

As a binder for the concretes, Portland cement of the grade CEM I 32.5B, produced by AO PO "Yakutcement" in accordance with the interstate standard GOST 31108-2016, was used. River sand from the floodplain of the Lena River, corresponding to all characteristics of the group "very fine" in accordance with the interstate standard GOST 8736, was used as a fine aggregate in the concrete. Crushed stone from a mixture of fractions from 10 to 40 mm, produced by AO PO "Yakutcement" from limestone rocks in the village of Mokhsogollokh in accordance with the interstate standard GOST 8267-93, was used as a coarse aggregate.

As a plasticizing admixture for the concretes in this work, a highly concentrated superplasticizing admixture based on polyaryl and polycarboxylate ethers for concretes with enhanced retainability – MasterPolyheed 4001 to decrease retardation effects on cement hydration [29], in accordance with the organizational standard STO 70386662-309-2021, is used. The working composition of the concrete was adopted as the composition selected according to GOST 27006-2019 for the chosen materials for the normative strength corresponding to class B12.5 in accordance with the interstate standard GOST 26633-2015. The initial components, shown in Table 1, were mixed using an LS-CB-10 laboratory mixer and compacted in molds measuring $100 \times 100 \times 400$ mm using a VM-6.4 vibration table, following interstate standard GOST 10180-2012. The weighing of the components was performed on A&D GF-6100 electronic scales. The concretes was prepared in the "Building Materials" laboratory of the Engineering and Technical Institute of NEFU (Yakutsk, Russia).

Table 1. Composition of the concrete mix.

Composition	Mass, kg			
Portland cement CEM I 32,5	5.62			
Limestone aggregate 10–20 and 20–40 mm	16.16			
Water	2.76			
River sand	7.73			
Plasticizer + liquid glass	0.114			
Reduced oxidized graphene (MOG) 0.2 и 0.5 %	0.011 и 0.031			

2.3. Electrical Resistivity Measurements

To measure the resistivity of concretes in a free state, a digital multimeter FAZA MAS830L (Russia) was used. The specific resistivity of concrete during loading was measured using a programmable power supply AKTAKOM APS-7151 (Finland). For this purpose, 4 mesh electrodes made of stainless steel, sized 8×12 cm, were embedded into the samples in the form of prisms measuring $40 \times 10 \times 10$ cm during molding. Analysis of the behavior of the electrical resistivity of concrete under deformation was carried out according to interstate standard GOST 10180-2012.

2.4. Mechanical Testing

The concrete samples were tested for compression on a hydraulic press IP-1250M-auto (Russia) according to interstate standard GOST 10180-2012 (Fig. 2). The samples were loaded after 7, 14 and 28 days. The test was completed when a crack appeared on two sides of the sample.



Figure 2. Photo of mechanical testing and electrical resistivity measurements.

3. Results and Discussion

Based on the conducted Raman spectroscopy studies (Fig. 3) of concretes after 28 days with minimally oxidized graphene (MOG), the presence of hydroxyl groups (–OH) in the wavenumber range of 3200–3400 cm⁻¹ enhances bonding within the cement matrix, reducing porosity and increasing resistance to water penetration [30]. Carbonyl groups (C=O), observed in the range of 1600–1800 cm⁻¹, participate in forming additional bonds, thereby improving the concrete's strength and chemical resistance [31]. Additionally, the presence of unsaturated carbon bonds (C=C) in the range of 1400–1600 cm⁻¹ enhances flexibility and crack resistance, crucial for maintaining structural integrity [32].

Further modifications include the presence of C–H bonds, noted in the range of 2800–3000 cm⁻¹ which are associated with organic components that reduce brittleness and improve resilience to mechanical stresses [33]. Peaks observed in the 2200–2400 cm⁻¹ range suggest the presence of C≡C bonds or nitriles, indicating potential organic additives [34]. These functional groups collectively contribute to a denser microstructure, enhancing the material's overall durability and resistance to environmental degradation [35].

The unusual appearance of the red spectrum for MOG can be attributed to several factors. Structural heterogeneity in minimally oxidized graphene (MOG) leads to diverse spectral features, as different regions of the material interact variably with infrared radiation. Additionally, defects, such as vacancies or incomplete bonds in the graphene structure, cause scattering and anomalies, resulting in the spectrum's "unusual" appearance. Variations in oxidation levels influence the presence and intensity of functional groups like –OH and –COOH, creating complex spectra with multiple peaks [36].

The multilayered structure of MOG can induce complex vibrational modes, causing additional peaks and spectral anomalies in the intensity and line positions of moisture or other substances in the sample. These factors collectively contribute to the complexity of the MOG spectrum, reflecting its unique physical and chemical properties, and making interpretation challenging.

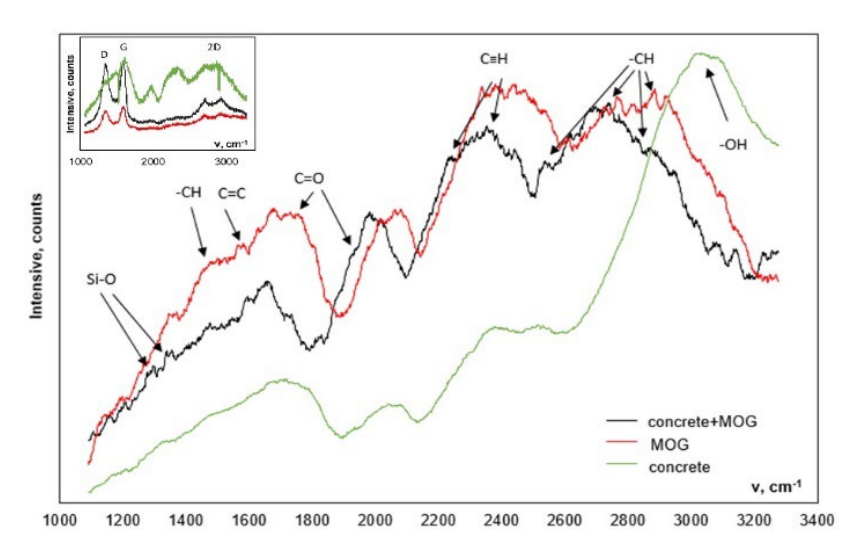


Figure 3. Raman spectrum of concrete modified with MOG after 28 days.

To reveal a more complete molecular picture of the concrete composition, an additional study was carried out by IR spectroscopy on an FTS 7000 IR Fourier step-scan spectrometer (Varian, USA) using an ATR attachment (Fig. 4).

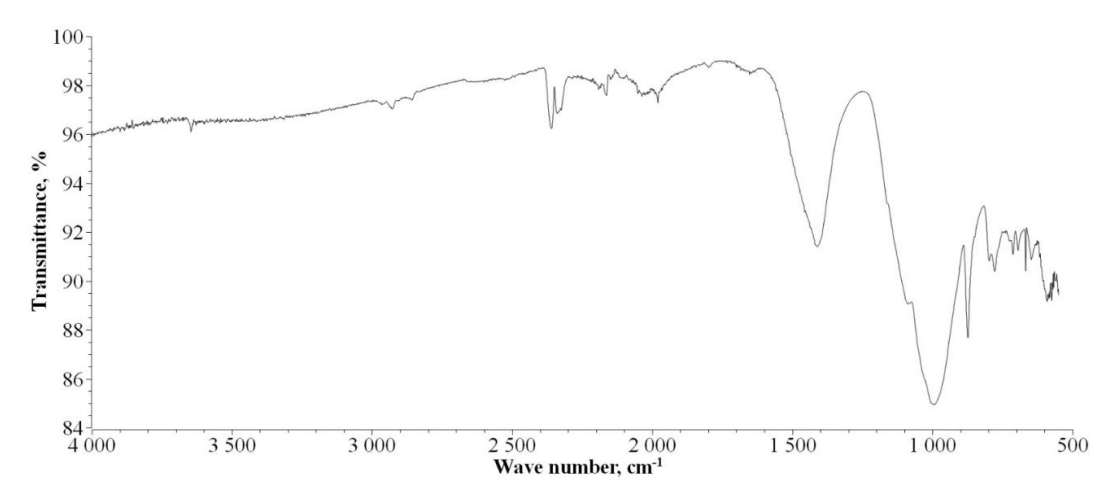


Figure 4. IR spectrum of concrete modified with MOG after 28 days.

From the IR spectrum of the concrete mix, the presence of organic impurities of polymer can be confirmed by the bands at 2930 and 2860 cm $^{-1}$, which may substantiate the hypothesis about the possible contribution of C–H vibrations to the peak at 2750 cm $^{-1}$ in the Raman spectrum. The appearance of a peak at 2165 cm $^{-1}$ from triple C \equiv C bonds is likely due to combination scattering on the triple C \equiv C bonds in graphene fragments. That is, this may be a characteristic peak of graphene itself, included in the composite material formulation. The intensity of this peak in the IR spectrum is usually low due to the selection rules for vibrations with an even number of atoms in the molecule. But nevertheless, it can be observed. The broad intense band at 1000 cm $^{-1}$ and peaks in the 500–800 cm $^{-1}$ region are due to vibrations of various mineral components of the cement stone.

Based on a comprehensive analysis of Raman and infrared spectra, it was found that the introduction of graphene is confirmed by the appearance of characteristic G (1600 cm⁻¹) and D (1350 cm⁻¹) peaks indicating the incorporation of graphene particles into an inert mineral matrix. The spectra were recorded using a laser at wavelengths of 633 and 514 nm. Signs of component interaction were detected – gas adsorption, possible functionalization of the graphene surface. The presence of additional organic impurities from the source materials was also revealed. In general, the study demonstrated the promise of the studied approach for evaluating the effectiveness of modifying concrete properties with carbon nanomaterials using a set of spectroscopic techniques.

According to the microphotographs (Fig. 5) of concrete, it can be seen that the concrete structure is heterogeneous, consisting of various phases and inclusions [37]. Both large inclusions up to 100 μ m in size and smaller submicron particles are observed. The shape of the particles is predominantly rounded. From Table 2, the main elements are oxygen, silicon, carbon and calcium. This corresponds to the composition of cement stone based on calcium hydrosilicates and hydroaluminates. Mineral additives containing

sodium, magnesium, aluminum, sulfur, potassium and iron are also present. These are likely sand, ash and other fillers. The distribution of elements is quite uniform, no significant accumulations of any phases are observed. This indicates uniform mixing of components during concrete production. The absence of chlorine indicates the use of low-chloride cement, which has a positive effect on the corrosion resistance of concrete. By the carbon distribution, it can be assumed that there is no aggregation in the obtained samples, and the ratio of carbon to the total number of components exceeding 15–30 % indicates the sensitivity of the method for detecting MOG.

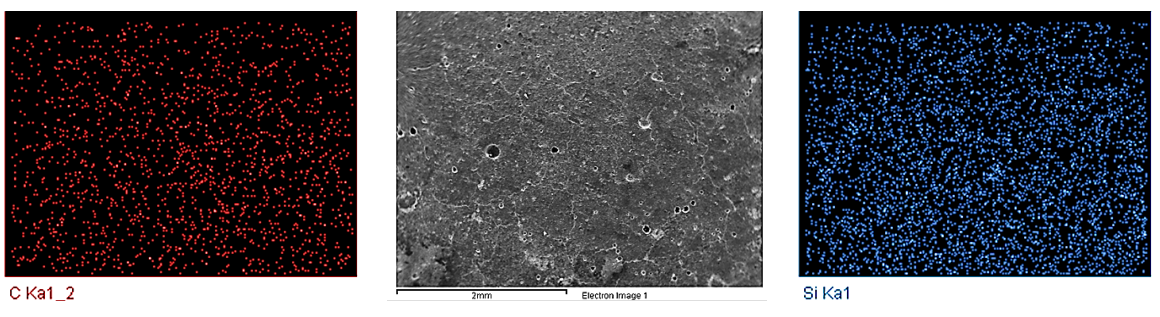


Figure 5. Microphotographs of the concrete 28 days surface showing the distribution of C and Si atoms.

Table 2. Distribution of components in the studied sample (Fig. 5).

Spectrum	С	Na	Mg	Al	Si	CI	K	Ca	Fe	Total
Sum Spectrum	47.05	1.41	1.00	2.11	11.19	0.00	1.86	33.37	1.18	99.18
Mean	47.05	1.41	1.00	2.11	11.19	0.00	1.86	33.37	1.18	99.18
Std. deviation	0.00	0.00	0.00	0.00	0.00	0.00	0.00	0.00	0.00	_
Max.	47.05	1.41	1.00	2.11	11.19	0.00	1.86	33.37	1.18	_
Min.	47.05	1.41	1.00	2.11	11.19	0.00	1.86	33.37	1.18	_

^{*}All results in compound, %

Figs. 6 and 7 show graphics of the compressive strength of concrete at different concentrations of MOG 7, 14 and 28 days and photographs of concrete samples after compression tests. The load applied to the concrete was calculated in kN per base area of the prism, equal to 10,000 mm². According to the test results of B12.5 grade concrete (strength up to 12.5–15.5 MPa) with 0.2 and 0.5 % MOG content by cement weight, it was revealed that when MOG is added to the concrete mix, the resistivity of the finished product decreases with increasing external load (compression). The rate of change in the resistivity of concrete decreased with increasing compression of the sample (Fig. 8). A sharp drop in resistivity when reaching the critical load level indicates high sensitivity to mechanical deformation. The yield point of concrete was observed in the range of 40–50 kN for all concrete ages.

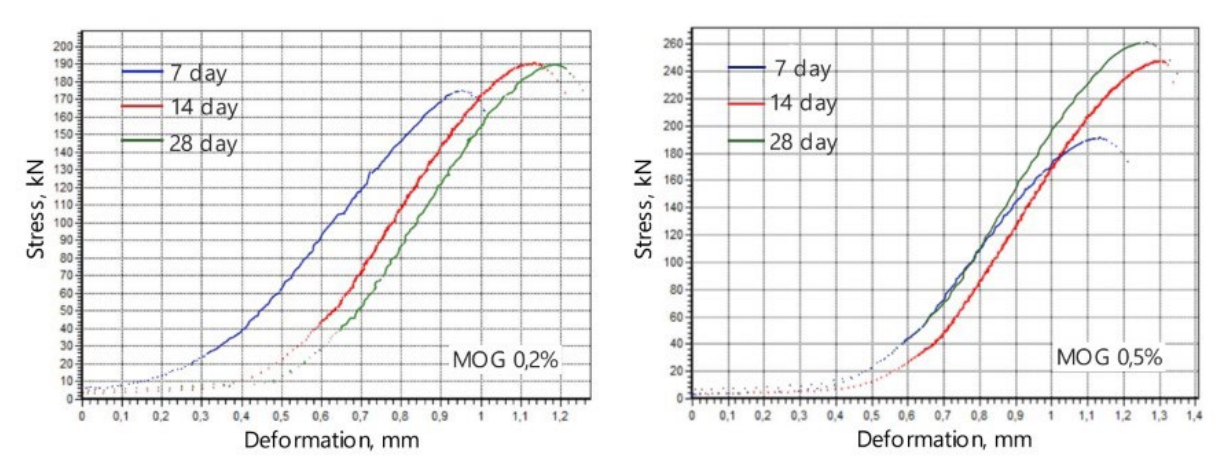


Figure 6. Compressive strength at different concentrations of MOG 7, 14 and 28 days.

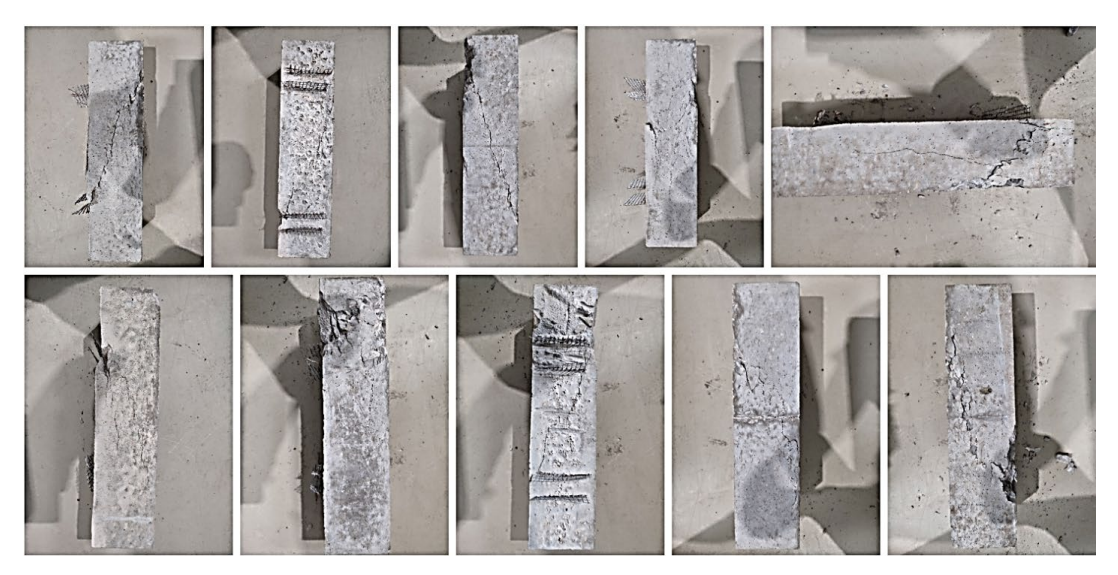


Figure 7. Photographs of modified concrete after testing.

The samples showed traces of vibration compaction in the concrete mixture due to molding. The nature of the destruction of the samples indicates brittle destruction without plastic deformation. The shape of the cracks allows us to estimate the stress-strain state of the samples during failure. The cracks propagate perpendicular to the direction of the applied compressive load, which corresponds to the laws of fracture mechanics of brittle materials. The absence of curved or inclined cracks indicates the isotropy of concrete properties in different directions. The clear, straight edges of the cracks indicate the brittle nature of destruction without plastic deformation. The relatively flat surface of the cracks without waviness or irregularities indicates a homogeneous concrete structure. The splitting of the sample into two parts along one plane confirms the brittle destruction under compressive load. The absence of spall, chips and delamination indicates sufficient strength of the aggregate bond with the cement stone. The color of the samples is uniform; no visible defects or delamination are observed.

The results obtained in this work on the mechanical properties of graphene oxide-modified cement composites are in agreement with previous studies. Pan et al. at work [38] reported an increase in compressive strength of 48 % with graphene oxide adding only 0.05 % to the weight of cement. Peng et al. at work [39] also showed that small additions of graphene oxide up to 0.05 % enhanced the flexural and compressive strengths of cement mortars.

The destruction of the concrete samples occurred from the side in contact with the plate until a crack reached the edge of the electrode sides (deformation). Thus, to measure the samples during loading, it is necessary to replace the 4-probe method with the 2-probe method, eliminating the influence of external factors on the stability of the resistivity value (material, conductive adhesive, drying rate of the adhesive, moisture content of the material itself).

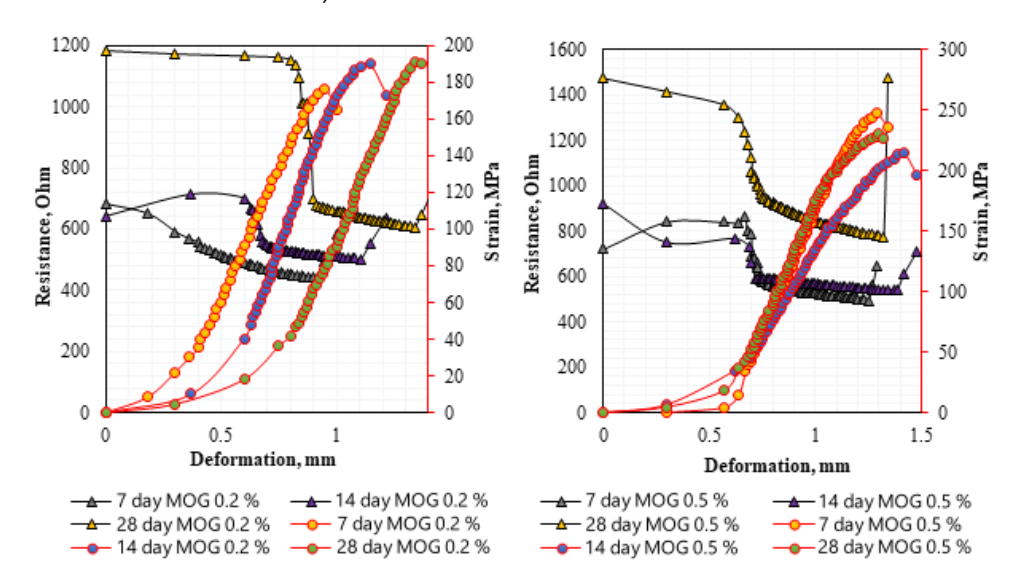


Figure 8. Graphs of the dependence of the change in the internal resistance of samples with 0.2 % MOG content (left) and 0.5 % MOG content (right) on deformation and load for 7, 14 and 28 days of curing.

Fig. 9 shows graphs of the dependence of the electrical resistivity of concrete samples on load. The electrical resistivity decreases with increasing load for all samples, which indicates the sensitivity of concrete to compression deformation. The electrical resistivity drops fastest at the beginning of loading, and then the decrease slows down. For the sample with 0.2 % graphene, the electrical resistivity drops more sharply (by 2 orders of magnitude) than for the sample with 0.5 % graphene (by 10 times). The sensitivity to deformation is higher for 7-day-cured samples compared to 14- and 28-day-cured ones. When the ultimate strength is reached, there is a sharp jump in electrical resistivity associated with sample failure. The behavior of the dependencies is similar for all curing times, indicating the reproducibility of the results. Thus, the introduction of graphene increases the sensitivity of concrete to compressive deformation. These graphs illustrate the possibility of using graphene-modified concrete as a self-sensing "smart" material.

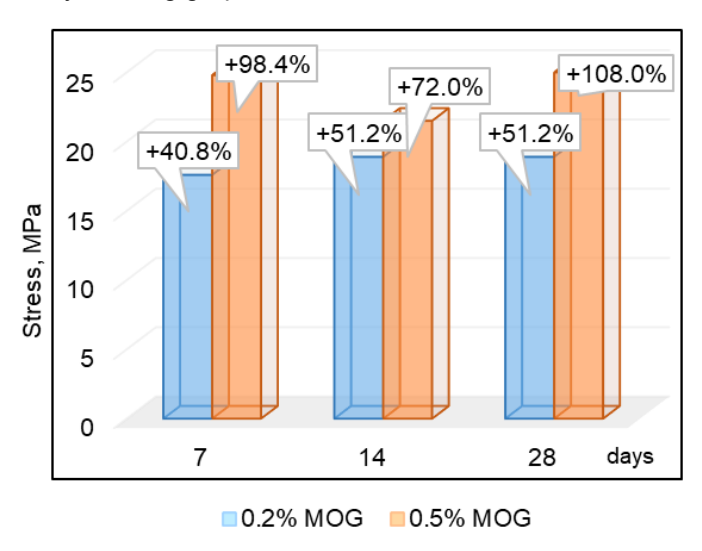


Figure 9. Graph of maximum breaking load for 7, 14, 28 days of curing of concrete samples modified with MOG.

4. Conclusion

- 1. The studies conducted using Raman and IR spectroscopy confirmed the successful incorporation of graphene nanoparticles into the inert mineral matrix of concrete. Structural distortions and various defects observed in graphene indicate its interaction with the cement composite components.
- 2. When MOG was added at 0.2 % of the cement weight, the resistivity decreased with increasing external load due to the compression of graphene sheets, which enhanced conductivity. The resistivity change rate decreased with further compression, and a sharp drop was noted at a certain load level, showing high sensitivity to mechanical deformation.
- 3. Concrete samples of grade M15 demonstrated a decrease in resistivity from the start of loading to 550–600 Ohm, returning to their initial values. The yield point was around 40–50 kN (plate pressure per 100 cm²). For cubic samples, increasing sensitivity to external loads required moistening. Measurements, taken both by the 2-probe method and with a digital multimeter, showed that moistened material could detect loads even with finger pressure (1 N).
- 4. The introduction of reduced oxidized graphene significantly improved the electrically conductive properties of concrete, offering broad application prospects:
 - Electromagnetic Shielding: Creates structures for protection against electromagnetic fields, useful in residential and industrial buildings [40, 41].
 - Self-Heating Concrete: Enables cost-effective heating for road surfaces, indoor floors, and prevents icing [42–48].
 - Sensory Structures: Detects mechanical stresses and deformations [49], aiding in structural integrity and operational optimization.
 - Corrosion Protection: Provides protection in reinforced concrete structures exposed to aggressive environments [50, 51].
 - Energy Storage: Enhances capacitive properties, paving the way for concrete batteries and supercapacitors [52, 53].

 Wireless Charging Roads: Facilitates the wireless charging of electric vehicles, increasing range and reducing charging time [54–56].

References

- 1. Krystek, M., Ciesielski, A., Samorì, P. Graphene-based cementitious composites: Towards next generation construction technologies. Advanced Functional Materials. 2021. 31(27). Pp. 2101887. DOI: 10.1002/adfm.202101887
- Chung, D.D.L. Cement reinforced with short carbon fibers: a multifunctional material. Composites Part B: Engineering. 2000. 31(6–7). Pp. 511–526. DOI: 10.1016/S1359-8368(99)00071-2
- Reddy, P., Ravi Prasad, D. Graphene oxide reinforced cement concrete A study on mechanical, durability and microstructural characteristics. Fullerenes, nanotubes and carbon nanostructures. 2023. 31(3). Pp. 255-265. DOI: 10.1080/1536383X.2022.2141231
- 4. Suo, Y. et al. A Review of graphene oxide/cement composites: Performance, functionality, mechanisms and prospects. Journal of Building Engineering. 2022. 53. Pp. 104502. DOI: 10.1016/j.jobe.2022.104502
- 5. Sassani, A., Arabzadeh, A., Ceylan, H. et al. Carbon fiber-based electrically conductive concrete for salt-free deicing of pavements. Journal of Cleaner Production. 2018. 203. Pp. 799–809. DOI: 10.1016/j.jclepro.2018.08.315
- Wang, X. et al. Mechanical and Electrical Properties of Multilayer Graphene Composite Conductive Concrete. Journal of Cold Regions Engineering. 2023. 37(3). Article no. 04023015. DOI: 10.1061/JCRGEI.CRENG-680
- 7. Arabzadeh, A. et al. Electrically conductive asphalt concrete: An alternative for automating the winter maintenance operations of transportation infrastructure. Composites Part B: Engineering. 2019. 173. Pp. 106985. DOI: 10.1016/j.compositesb.2019.106985
- 8. Choi, K., et al. Nanostructured thermoelectric composites for efficient energy harvesting in infrastructure construction applications. Ceramics International. 2022. 128. Pp. 104452. DOI: 10.1016/j.cemconcomp.2022.104452
- 9. Ghosh, S., Harish, S., Ohtaki, M., Saha, B.B. Enhanced figure of merit of cement composites with graphene and ZnO nanoinclusions for efficient energy harvesting in buildings. Energy. 2020. 198. Article no. 117396. DOI: 10.1016/j.energy.2020.117396
- 10. Kashif Ur Rehman, S. et al. A review of microscale, rheological, mechanical, thermoelectrical and piezoresistive properties of graphene based cement composite. Nanomaterials. 2020. 10(10). Pp. 2076. DOI: 10.3390/nano10102076
- 11. Rostami, H., Shao, Z., Boyd, M., He, Z. Mechanical properties of graphene oxide cement paste. Architecture, Civil Engineering, Environment. 2019. 12(1). Pp. 99–105. DOI: 10.21307/ACEE-2019-008
- 12. Jiang, S., Shang, Z., Hou, C. et al. Piezoresistive properties of ultra-high-performance fiber-reinforced concrete incorporating few-layer graphene. Construction and Building Materials. 2021. 305. Pp. 124362. DOI: 10.1016/j.conbuildmat.2021.124362
- 13. Pei, C., Ueda, T., Zhu, J. Investigation of the effectiveness of graphene/polyvinyl alcohol on the mechanical and electrical properties of cement composites. Materials and Structures. 2020. 53. Pp. 1-15.DOI: 10.1617/s11527-020-01508-6
- 14. Dimov, D. et al. Ultrahigh performance nanoengineered graphene–concrete composites for multifunctional applications. Advanced functional materials. 2018. 28(23). Pp. 1705183. DOI: 10.1002/adfm.201705183
- 15. Wang, S., Singh, A., Liu, Q. Experimental study on the piezoresistivity of concrete containing steel fibers, carbon black, and graphene. Frontiers in Materials. 2021. 8. Pp. 652614. DOI: 10.3389/fmats.2021.652614
- Kedir, A., Gamachu, M., Alex, A. G. Cement-based graphene oxide composites: a review on their mechanical and microstructure properties. Journal of Nanomaterials. 2023. 2023(1). Pp. 6741000. DOI: 10.1155/2023/6741000
- 17. Li, W. et al. A comprehensive review on self-sensing graphene-cement composites: a pathway to next-generation smart concrete. Construction and Building Materials. 2022. 331. Pp. 127284. DOI: 10.1016/j.conbuildmat.2022.127284
- 18. Schulte J. et al. Graphene-reinforced cement composites for smart infrastructure systems. The Rise of Smart Cities. 2022. Pp. 79–114. DOI: 10.1016/B978-0-12-817784-6.00008-4
- 19. Chen, R. Preparation, property determination and bridge health monitoring applications of self-sensing cement nanocomposites. Alexandria Engineering Journal. 2023. 66. Pp. 891-900. DOI: 10.1016/j.aej.2022.10.061
- 20. Lu, D. et al. Growing nanocrystalline graphene on aggregates for conductive and strong smart cement composites. ACS nano. 2023. 17(4). Pp. 3587-3597. DOI: 10.1021/acsnano.2c10141
- Polverino, S. et al. Few-layers graphene-based cement mortars: production process and mechanical properties //Sustainability. 2022. 14(2). Pp. 784. DOI: 10.3390/su14020784
- 22. Papanikolaou, I., Arena, N., Al-Tabbaa, A. Graphene nanoplatelet reinforced concrete for self-sensing structures—A lifecycle assessment perspective. Journal of Cleaner Production. 2019. 240. Pp. 118202. DOI: 10.1016/j.jclepro.2019.118202
- 23. Gokhale, D. G. K., Kaish, A. B. M. Recent trends in incorporating graphene coated sand in self-sensing cementitious composites. Materials Proceedings. 2023. 14(1). Pp. 48. DOI: 10.3390/IOCN2023-14544
- 24. Wang, Z., Wang, Z., Ning, M. et al. Electro-thermal properties and Seebeck effect of conductive mortar and its use in self-heating and self-sensing system. Ceramics International. 2017. 43(12). Pp. 8685–8693. DOI: 10.1016/j.ceramint.2017.03.202
- 25. Hu, Y. G. et al. Experimental study of the electrical resistance of graphene oxide-reinforced cement-based composites with notch or rebar. Journal of Building Engineering. 2022. 50. pp. 104331. DOI: 10.1016/j.jobe.2022.104331
- 26. Lavagna, L. et al. Cement-based composites containing oxidized graphene nanoplatelets: effects on the mechanical and electrical properties. Nanomaterials. 2023. 13(5). Pp. 901. DOI: 10.3390/nano13050901
- Papanikolaou, I., Al-Tabbaa, A., Goisis, M. An Industry Survey on the Use of Graphene-Reinforced Concrete for Self-Sensing Applications. International Conference on Smart Infrastructure and Construction 2019 (ICSIC): Driving data-informed decision-making. ICE Publishing, 2019. Pp. 613–622. DOI: 10.1680/icsic.64669.613
- 28. Syama, S., Mohanan, P.V. Safety and biocompatibility of graphene: A new generation nanomaterial for biomedical application. International Journal of Biological Macromolecules. 2016. 86. Pp. 546–555. DOI: 10.1016/j.ijbiomac.2016.01.116
- Xia L., Zhou M., Ni T., Liu, Z. Synthesis and characterization of a novel early strength polycarboxylate superplasticizer and its performances in cementitious system. Journal of Applied Polymer Science. 2020. 137(30). Article no. 48906. DOI: 10.1002/app.48906
- 30. Sobczyk-Guzenda, A. et al. Micro-and Nanoparticulate Hydroxyapatite Powders as Fillers in Polyacrylate Bone Cement A Comparative Study. Materials. 2020. 13(12). Article no. 2736. DOI: 10.3390/ma13122736
- Pang, B. et al. Ultraductile cementitious structural health monitoring coating: waterborne polymer biomimetic muscle polyhedral oligomeric silsesquioxane-assisted c-s-h dispersion. Advanced Functional Materials. 2022. 32(51). Article no. 2208676. DOI: 10.1002/adfm.202208676

- 32. Leonovich, S.N., Sadovskaya, E.A. Strength Indicators of Fiber Reinforced Concrete with Carbon Nanomaterials. Science & Technique. 2024. 23(3). Pp. 219–224. DOI: 10.21122/2227-1031-2024-23-3-219-224
- 33. Malakar, A. et al Mussel-inspired double cross-linked interpenetrating network with unique mechanical properties using di-diol complexation. SPE Polymers. 2023. 4(3). Pp. 83–92. DOI: 10.1002/pls2.10088
- 34. Shen, T., Wang, T., Qin, C., Jiao, N. Silver-catalyzed nitrogenation of alkynes: a direct approach to nitriles through C≡ C bond cleavage. Angewandte chemie international edition. 2013. 125(26). Article no. 6677–6680. DOI: 10.1002/anie.201300193
- 35. Bai, T., Li, H. Revealing the Mechanism of Alcohol Dehydroxylation and C–C Bond Formation through Concerted Catalysis by Ir/Cu Bimetallic Complexes. The Journal of Organic Chemistry. 2024. 89(8). Pp. 5363–5370. DOI: 10.1021/acs.joc.3c02740
- 36. Iranifam, M. MOFs-, COFs-and MOGs-assisted chemiluminescence methods. Microchemical Journal. 2024. 199. Article no. 110096. DOI: 10.1016/j.microc.2024.110096
- Beskopylny, A.N., Shcherban', E.M., Stel'makh, S.A., Mailyan, L.R., Meskhi, B., Razveeva, I., Kozhakin, A., Beskopylny, N., El'shaeva, D., Artamonov, S. Method for Concrete Structure Analysis by Microscopy of Hardened Cement Paste and Crack Segmentation Using a Convolutional Neural Network. Journal of Composites Science. 2023. 7(8). Article no. 327. DOI: 10.3390/jcs7080327
- 38. Peng, H., Ge, Y., Cai, C. S., Zhang, Y., Liu, Z. Mechanical properties and microstructure of graphene oxide cement-based composites. Construction and Building Materials. 2019. 194. Pp. 102–109. DOI: 10.1016/j.conbuildmat.2018.10.234
- 39. Zhang, N., She, W., Du, F., Xu, K. Experimental Study on Mechanical and Functional Properties of Reduced Graphene Oxide/Cement Composites. Materials. 2020. 13(13). Article no. 3015. DOI: 10.3390/ma13133015
- Khalid, T., Albasha, L., Qaddoumi, N.N., Yehia, S. Feasibility Study of Using Electrically Conductive Concrete for Electromagnetic Shielding Applications as a Substitute for Carbon-Laced Polyurethane Absorbers in Anechoic Chambers. IEEE Transactions on Antennas and Propagation. 2017. 65(5). Pp. 2428–2435. DOI: 10.1109/TAP.2017.2670538
- 41. Yehia, S., Qaddoumi, N.N., Hassan, M.S., Swaked, B. Conductive Concrete for Electromagnetic Shielding Applications. Advances in Civil Engineering Materials. 2014. 3(1). Article no. ACEM20130107. DOI: 10.1520/ACEM20130107
- 42. Wang, X. et al. Road use and electrothermal performance of graphene-conductive asphalt-recycled pervious concrete under severe cold environment. Construction and Building Materials. 2023. 400. Article no. 132829. DOI: 10.1016/j.conbuildmat.2023.132829
- 43. Maleki, P., Iranpour, B., Shafabakhsh, G. Investigation of de-icing of roads with conductive concrete pavement containing carbon fibre-reinforced polymer (CFRP). International Journal of Pavement Engineering. 2019. 20(6). Pp. 682–690. DOI: 10.1080/10298436.2017.1326235
- 44. Mingqing, S. et al. Experimental studies on the indoor electrical floor heating system with carbon black mortar slabs. Energy and Buildings. 2008. 40(6). Pp. 1094–1100. DOI: 10.1016/j.enbuild.2007.10.009
- 45. Yinfei, D. et al. Using silicon carbide to increase thermal conductivity of cement composite for improving heating efficiency of floor heating system. Construction and Building Materials. 2022. 325. Article no. 126707. DOI: 10.1016/j.conbuildmat.2022.126707
- 46. Heinlein, U., Freimann, T. Industrial concrete floors: evaluation of electrostatic dissipative properties according to IEC 61340-4-1. Construction and Building Materials. 2022. 329. Article no. 127162. DOI: 10.1016/j.conbuildmat.2022.127162
- 47. Lee, H., Yu, W., Loh, K.J., Chung, W. Self-heating and electrical performance of carbon nanotube-enhanced cement composites. Construction and Building Materials. 2020. 250. Article no. 118838. DOI: 10.1016/j.conbuildmat.2020.118838
- 48. Farcas, C. et al. Heating and de-icing function in conductive concrete and cement paste with the hybrid addition of carbon nanotubes and graphite products. Smart Materials and Structures. 2021. 30. Article no. 045010. DOI: 10.1088/1361-665X/abe032
- 49. Qin, H. et al. Revolutionizing infrastructure: The evolving landscape of electricity-based multifunctional concrete from concept to practice. Progress in Materials Science. 2024. 145. Article no. 101310. DOI: 10.1016/j.pmatsci.2024.101310
- 50. Sharma, N. et al. Evaluation of corrosion inhibition capability of graphene modified epoxy coatings on reinforcing bars in concrete. Construction and Building Materials. 2022. 322. Article no. 126495. DOI: 10.1016/j.conbuildmat.2022.126495
- 51. Sohn, H. et.al. Operation of battery-less and wireless sensor using magnetic resonance based wireless power transfer through concrete. Smart Structures and Systems. 2016. 17(4). Pp. 613–646. DOI: 10.12989/SSS.2016.17.4.631
- 52. Tian, Z. et al. Analysis and Optimization of Asymmetric Wireless Power Transfer in Concrete. Wireless Communications and Mobile Computing. 2020. 2020(1). Article no. 8841210. DOI: 10.1155/2020/8841210
- 53. Basha, S.I. et al. Construction building materials as a potential for structural supercapacitor applications. The Chemical Record. 2022. 22(11). Article no. e202200134. DOI: 10.1002/tcr.202200134
- 54. Nguyen, D.H. Dynamic optical wireless power transfer for electric vehicles. IEEE Access. 2023. 11. Pp. 2787–2795. DOI: 10.1109/ACCESS.2023.3234577
- 55. Behnamfar, M., Tariq, M., Sarwat, A. Novel combined inductive and capacitive wireless power transfer system to reduce power pulsation for dynamic charging of electric vehicles. 2023 IEEE Industry applications society annual meeting (IAS), Nashville, 2023. Pp. 1–6. DOI: 10.1109/IAS54024.2023.10406764
- 56. Yang, L. et al. Differentiated speed planning for connected and automated electric vehicles at signalized intersections considering dynamic wireless power transfer. Journal of Advanced Transportation. 2022. Article no. 5879568. DOI: 10.1155/2022/5879568

Information about the authors:

Elena Vasileva,

ORCID: https://orcid.org/0000-0001-8953-9309

E-mail: vasilyeva edm@mail.ru

Dmitry Popov,

ORCID: <u>https://orcid.org/0000-0001-9639-7601</u>

E-mail: dmiitryy09@gmail.com

Pavel Vinokurov,

ORCID: https://orcid.org/0000-0003-2004-6631

E-mail: pv.vinokurov@s-vfu.ru

Aleksandr Popov, PhD in Technical Scieneces ORCID: https://orcid.org/0000-0002-7829-6839

E-mail: surrukin@gmail.com

Received 25.01.2024. Approved after reviewing 26.11.2024. Accepted 30.11.2024.



Magazine of Civil Engineering

ISSN 2712-8172

journal homepage: http://engstroy.spbstu.ru/

Research article UDC 691.1

DOI: 10.34910/MCE.132.4



Construction of coconut shell column for the enhancement of expansive soil

Universiti Malaysia Pahang Al-Sultan Abdullah, Kuantan, Pahang, Malaysia

Keywords: expansive clay, coconut shell, ground improvement, shear strength, foundation, stiffness, experimental investigation, sustainable development, reinforcement

Abstract. The authors used the crushed coconut shell to make granular columns which were obtained from the market area of Kuantan, Pahang. The coconut was crushed into a similar size of coarse aggregate for the replacement of non-renewable resources like sand and gravel. From its general properties, a coconut shell is hard and can withstand a certain value of exerted value regardless of compression or tension. Besides, the coconut shell is an agricultural product and is found abundantly after human consumption. For this research, the stone-column method was used. The installation of a single coconut shell column was implemented through the Vibro-replacement technique on the soft clay soil. Before accessing the shear strength parameters, the evaluation of the physical and mechanical properties of coconut shells and kaolin was executed via the appropriate geotechnical laboratory approaches. The shear strength parameters were analysed with the control and reinforced specimens through the Unconfined Compression Test (UCT). For the shear strength value, the average value from 4 specimens was utilized as the final value. A total of 16 samples were constructed for all the specimens, reinforced design comprised of 13 mm column diameter, and column heights of 60 mm and 80 mm were categorized as partially penetrated columns while 100 mm was a fully penetrated column. The highest shear strength improvement was recorded when the column height was 100 mm, resulting in 28.51 %, whereas the least was recorded when 60 mm of height was constructed, only 17.28 %. Conclusively, the positive results of shear strength improvements were yielded by the utilization of coconut shells and proved that it was practical and economical.

Funding: UMPSA Research Grant. RDU223309, Post Graduate Research Scheme (PGRS). PGRS2303122, MYBRAIN 2.0 Scholarship by the Ministry of Higher Education of Malaysia

Citation: Shen, N.J., Hasan, M., Anuar, N.N. Construction of coconut shell column for the enhancement of expansive soil. Magazine of Civil Engineering. 2024. 17(8). Article no. 13204. DOI: 10.34910/MCE.132.4

1. Introduction

Kaolin is a claystone composed mostly of kaolin minerals that are white or nearly white and can be beneficiated or fired to become white or nearly white [1]. Kaolin is a type of fine aggregate that has higher moisture content, and higher compressibility as compared to coarse aggregate like gravel. Higher moisture content with compressibility is likely to link with low soil bearing capacity which can cause soil settlement if a structure is placed on it. As reported by Karkush et al. [2], the authors discovered that soft clay soil possesses an undrained shear strength value of below 40 kPa, compressibility index value of 0.19 to 0.44, and moisture content of 40 % to 60 % to its total mass. Furthermore, Al-Ani et al. [3] defined the expansive soil as the rise in volume when subjected to moisture content. When the soil or ground-bearing capacity is not ample for catering to the structure [4], the selection of the best alternatives for a building from the available techniques depends on whether the decision-makers are owners, contractors, or other stakeholders [5]. Ground improvement techniques to improve the soil are often implemented at the preconstruction stage so that the mentioned issue can be addressed providing a safe structure to the

© Shen, N.J., Hasan, M., Anuar, N.N., 2024. Published by Peter the Great St. Petersburg Polytechnic University.

occupants. The increase of soil's strength or bearing capacity by developing effective solutions can be executed through the correct design of the foundation system [6]. Jawad et al. [7] mentioned the shear strength of soil is dependent on the interaction of soil particles and its pore fluid, which is expressed at the microscopic level. Without a proper geotechnical case study of the site condition, the wrong choice may be implemented regarding the type of foundation of the structure, which can lead to excessive material waste [8]. Construction of stone columns is a technique for stabilizing the considered weak clay, silt, or loose sands so that it is suitable for the building of embankments, bridge abutments, and other buildings [9]. The principle of the Vibro-replacement method involves the radial displacement of soil through a deep vibrator and further refilling the specific coarse aggregate or granular material to the pre-drilled diameter [10]. This can be further explained as about 10–40 % of soft clay soil will be replaced with compacted granular material, which provides better strength and stiffness than the original soil [11]. This is done to release the excess pore water pressure flowing within the subsoil as the constructed granular column acts as a drainage path to discharge the additional water content [12].

In recent years, many Southeast Asia countries including Malaysia have been actively developing the country. Some famous projects that are handled by foreign investors in Malaysia include the East Coast Rail Line (ECRL), Malaysia-China Kuantan Industrial Park (MCKIP), and Bandar Malaysia [13]. Huge infrastructure projects in Malaysia have covered a larger area and mostly intersect from state to state, using the different conditions of land for the entire project like the Lebuhraya Pantai Timur 2 (LPT 2) between Kuantan and Kuala Terengganu, where the geotechnical works like soil improvement and ground improvement of the existing foundation have been done before the construction project [14], [15].

Historically, the ground improvement technique is used for soil stabilization, but it depends on the nature of the strata. The techniques comprising soil improvement using additives, mechanical methods, admixtures, electrokinetic and thermal methods [16], [17]. Karkush et al. [18] deployed the grouting cement gel and silica fume in stabilizing the soft clay soil, by leveraging the cementitious properties of concrete and pozzolanic activity induced by silica fume. Previous researchers like Karkush et al. [19] altered the properties of soft clay soil via the mixture of crushed concrete and produced a positive result of shear strength improvement. Among these methods, the construction of stone columns is under the category of mechanical methods, where the substitution of foreign granular materials such as Polypropylene (PP) and bottom ash to replace the coarse aggregate regardless of the type of coarse aggregate used, this technique is to increase the soil bearing capacity at the same time decreasing the settlement of shallow footings as well as slabs [20]. Referring to the above materials, bottom ash, and PP materials are found to increase the shear strength of kaolin within 30-60 % [21], [22]. Other than these materials, the utilization of coconut shells which behave like coarse aggregate has the potential to replace gravel at reduce the natural resource depletion by producing a better environmentally friendly structure in civil engineering applications [23]. From other perspectives, coconut shell is a naturally biodegradable material, improving the performance of structure has become a significant interest for many researchers, where the addition of coconut shell in concrete increases its tensile strength [24]. Researchers have also studied environmentally friendly techniques for the usage of recycled sludge in soil improvement [25], even the consolidation of soil using drained-timber rods [26]. However, the selected coarse-aggregate type material must be free-draining, hard, and inert [27]. The selection of a coconut shell to construct the granular column is predicted to have increased the shear strength improvement rate as the coconut shell has durability characteristics, high toughness, and abrasion-resistant properties [28]. Sujatha et al. [29] verified the durability of coconut shell, which is comprised of lignin content that causes it to be more weather resistant, low cellulose content within the structure causes it to absorb less water. Coherent to that, recycled aggregate is also much easier due to low-cost issues as well as wide availability rather than natural resources [30]. To comply with the sustainability concept practice in construction, increasing the greenery index, application of coconut shell can be a potential and practical material in replacing the coarse aggregate for the granular column construction.

2. Methods

This chapter discussed the methods and materials used to conduct the relevant laboratory works by complying with the American Society for Testing and Materials (ASTM) and British Standard (BS) in order to achieve the objectives of this study as tabulated in Table 1. The first part focused on the materials involved, followed by the experiment setup.

Table 1. Relevant laboratory works and its standard.

Objective	Experiment	Standard
Determination of engineering	Atterberg limit	
properties of kaolin clay S300 and	Liquid limit	BS 1377: Part 2: 1990: 4.3
crushed coconut	Plastic limit	BS 1377: Part 2: 1990: 5.3
shell	Pycnometer	BS 1377: Part 2: 1990: 9.6
	Sieve analysis	BS 1377: Part 2: 1990: 9.6
	Hydrometer	BS 1377: Part 2: 1990: 8.3
	Relative density	ASTM D 4052
	Standard compaction	BS 1377: Part 2: 1990: 3.3
	Constant head	ASTM D 2434
	Falling head	ASTM D 2434
Determination of shear strength parameter by reinforcing the kaolin clay with crushed coconut shell column	Unconfined compression	ASTM D 2166

2.1. Materials

In this research, the vibro-replacement method as a ground improvement method was first determined after considering the estimated amount of materials to utilise and the restricted condition, small-scale laboratory test. The primary material of the study, Kaolin Clay S300 which was purchased from Kaolin (M) Sdn. Bhd, Selangor, Malaysia. The main intention of Kaolin Clay S300 selection was due to its natural properties, where it can easily be broken when in contact with the hydrogen (H⁺) and hydroxide ion (OH⁻), and it is a hydrophilic substance [31]. It was made available in powder form and white as shown in Fig. 1. This material was used for the column preparation and the nature properties of this material show that it was suitable to meet the research objective as shown in Table 2 [32]. The analysis showed that it comprised silt and clay, with no sand content and thus, it can first be classified as fine aggregate. Besides, the reinforcement material, coconut shell was selected as it met the requirements of being a granular-type material. A typical coconut shell is tough and hard to withstand physical loading, with a shell thickness of approximately 2–8 mm [33]. From Table 3, it was crucial to notice the natural moisture content of a coconut shell was low having a value of 4.20 % therefore can be a potential material to reduce the effect of water accumulation in kaolin clay. It was taken from Kuantan, Pahang, and then processed by grinding it in a machine into small pieces.



Figure 1. Kaolin clay S300 [22].

Table 2. Properties of kaolin clay \$300 [32].

No.	Physical Parameters	Value
1	Colour	White
2	Natural water content (%)	1.58
3	Specific gravity	2.59
	Atterberg limits:	
4	Liquid limit, $w_{\rm L}$ (%)	78
	Plastic limit, w_p (%)	39
	Plastic Index, I_p (%)	39
	Sieve analysis:	
5	Sand (%)	0
	Silt (%)	47
	Clay (%)	53

Table 3. Properties of coconut shell [24].

•		
No	Physical and Mechanical Properties	Coconut Shell
1	Maximum size (mm)	12.5
2	Moisture content (%)	4.20
3	Water absorption (24h) (%)	24.00
4	Specific gravity	1.05 to 1.20
	SSD * apparent	1.40-1.50
5	Impact value (%)	8.15
6	Crushing value (%)	2.58
7	Abrasion value (%)	1.63
8	Bulk density (kg/m³)	650
	Compacted loose	550
9	Fineness modulus	6.26
10	Shell thickness (mm)	2–8
11	Impact value (%)	8.15

2.2. Laboratory Works

The flow of the laboratory works was referred to in Fig. 2. The first objective of the study was to assess the general properties of both materials, kaolin clay S300 and crushed coconut shell. The relevant tests were conducted by complying with the suitable standard to classify its physical and mechanical properties which included the Atterberg limit test, pycnometer test, sieve analysis test, hydrometer test, relative density test, standard compaction or standard proctor test, constant head test and falling head test. The second objective was achieved by conducting the UCT, where the crushed coconut shell column was built beneath the kaolin clay. All the relevant information was tabulated in Table 1.

The Atterberg limit test was mainly designed for fine-grained soil where the soil can exist depending on the volume of water and it had a liquid limit test and plastic limit test, based on BS 1377: Part 2: 1990: 4.3 and BS 1377: Part 2: 1990: 5.3. By using cone-penetration method, the liquid limit for the prepared kaolin clay which passed through the 425 μ m sieve was determined. After the liquid limit test, the procedure was followed by moulding the kaolin into a spherical mould to determine the plastic limit. For specific gravity, was determined by a small pycnometer test based on BS 1377: Part 2: 1990: 9.6. This test was applied for both materials, where the materials were put inside a chamber after the preparation process. Fig. 2 (a) showed the determination of crushed coconut shells of specific gravity using kerosene. The particle size was determined by conducting sieve analysis or dry mechanical sieve analysis for crushed coconut shell based on BS 1377: Part 2: 1990: 9.6 while hydrometer test was carried out for kaolin clay S300 in accordance to BS 1377: Part 2: 1990: 8.3. Sieve analysis was for coarse type material, where the sieve sizes used were 200 mm, 14 mm, 10 mm, 5 mm, 3.35 mm, 2 mm, 1.18 mm, 0.6 mm, 0.3 mm, 0.15 mm and 0.0063 mm as shown in Fig. 2 (b). The kaolin clay was analysed under hydrometer as shown in Fig. 2 (c) as more than 50 % of the particles were finer than 63 μ m.

Furthermore, the Standard Compaction Test was carried out based on BS 1377: Part 2: 1990: 3.3. A 2.5 kg hammer with a 1 litre capacity of mould was deployed during the process as shown in Fig. 2 (d). The amount of kaolin clay used in this test was approximately 3.0 kg of oven-dried kaolin clay that passed through the 4.75 mm sieve size. Before accessing the shear strength parameters, the permeability which split into the constant head test and falling head test which shared both standards, ASTM D 2434 were conducted as depicted in Fig. 2 (e). Both tests determined the permeability using measuring both heads of water and the volume of water that flew through.

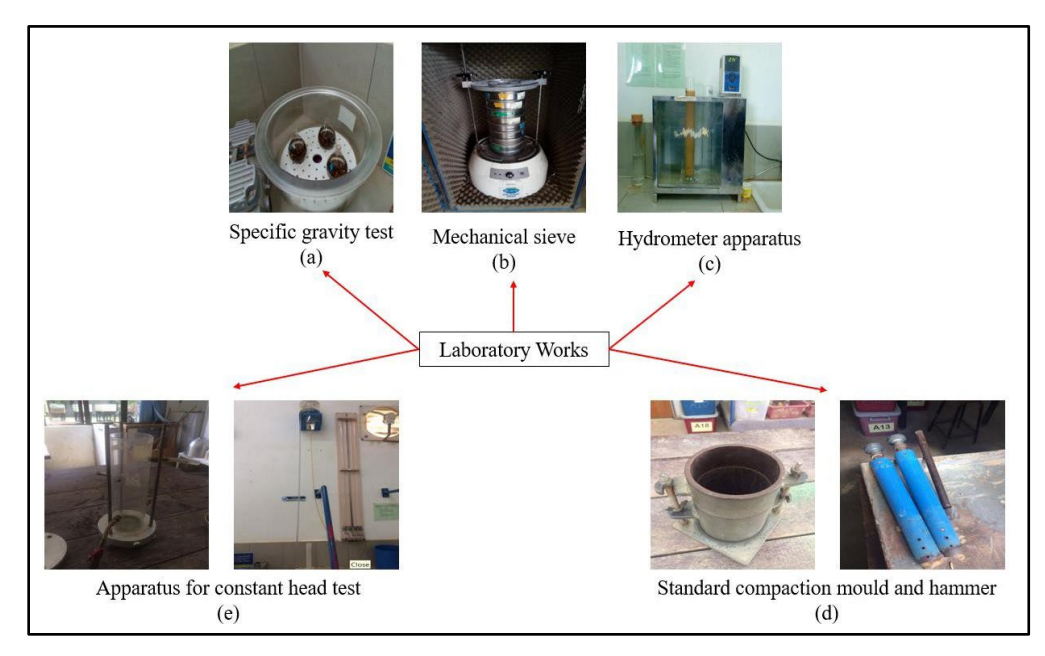


Figure 2. Flow of laboratory works (a) Pycnometer test (b) Dry sieve analysis (c) Hydrometer test (d) Standard compaction test (e) Constant head test.

The second objective was based on the UCT based on ASTM D 2166 by exerting the axial compression from the top towards the specimen at a constant deformation rate as shown in Fig. 3. Before conducting the UCT, the crushed coconut shell column was properly designed by considering the column parameters as well as the sieve size of the coconut shell. The column parameters which included column penetrating ratio (H_c/H_s), column height to column diameter ratio (H_c/D_c), and volume replacement ratio (V_c/V_s) were tabulated in Table 4. The granular column which was made up of crushed coconut shell, was split into the partially penetrated column and the fully penetrated column. Besides, the D/d ratio which indicated the Diameter of the column, D divided by the Diameter of the crushed coconut shell, d was also determined beforehand so that it was compared with another set of data. A similar study that used the polypropylene (PP) columns as reinforcement with the D/d value of 8.47 and 13.55 recorded shear strength improvement [22]. In this study, the D value was fixed at 14 mm, and the d value used in was 2 mm thus producing the ratio of D/d was 7. After several considerations and calculations, the detailed arrangement of the column built within the 50 mm kaolin column was drawn and illustrated in Fig. 4.



Figure 3. The specimen was compressed under UCT machine.

Table 4. Design dimension of crushed coconut shell column.

No.	No. of Column	Design	Diameter	Height (mm)	H _c /H _s	H _c /D _c	V _c /V _s
1	1	Control	NA	100	-	-	-
2	1	S1360		60	0.6	4.6153	0.0405
3	1	S1380	14	80	8.0	6.1538	0.0540
4	1	S13100		100	1.0	7.6923	0.0676

^{*}S1360 – "S" indicates as single column, "13" indicates the column diameter and "60" indicates the column height. All the dimensions are expressed in mm. NA – Not Available

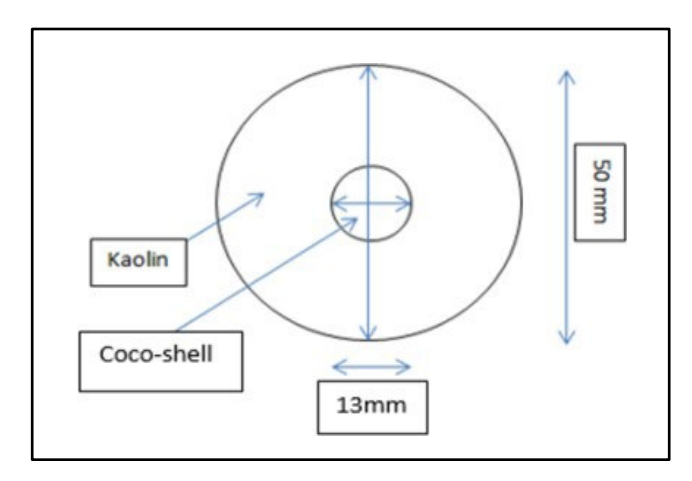


Figure 4. Arrangement details of a crushed coconut shell column.

For the process of column construction, it was shown in Fig. 5. The kaolin clay was mixed with approximate 20 % of water to its total weight, 300 g based on the value obtained from Standard Compaction Test. The prepared kaolin was transferred to the customized mould and compacted, followed by the drilling process. A 13 mm drilling bit was used to drill a hole in the middle of the prepared specimen based on the arrangement as shown in Fig. 4. The specimen had been prepared and the crushed coconut shell was poured inside through a filter funnel by raining method.

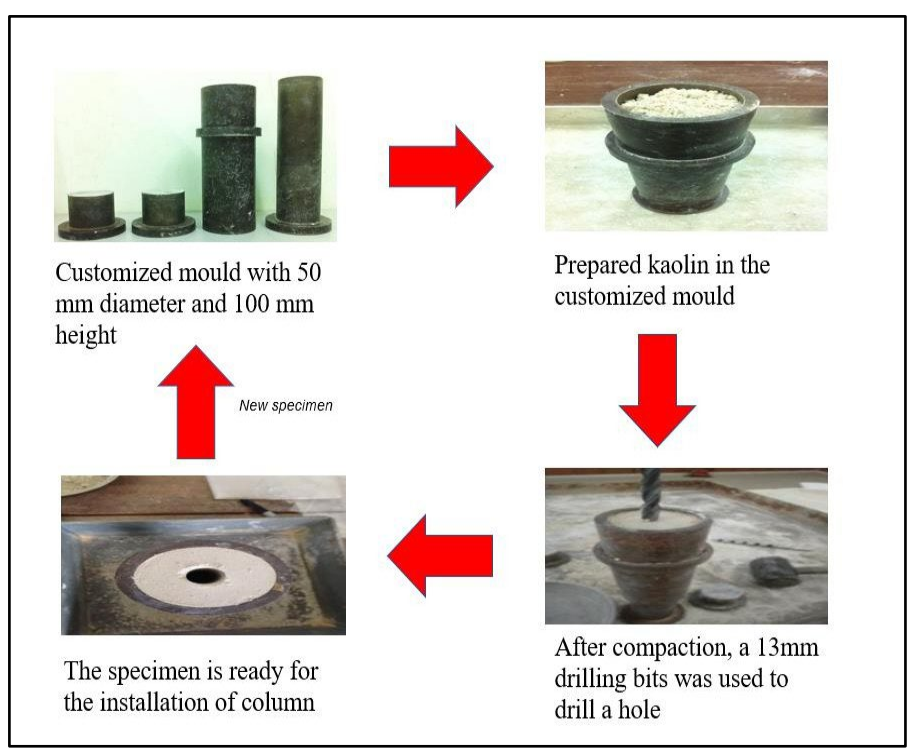


Figure 5. Crushed coconut shell column preparation process.

3. Results and Discussion

This chapter focused on the value obtained after conducting the related laboratory works, it was split into the engineering properties of kaolin clay S300 and the crushed coconut shell, efficiency of the materials used and the correlation of shear strength parameters in accordance to the specific parameters.

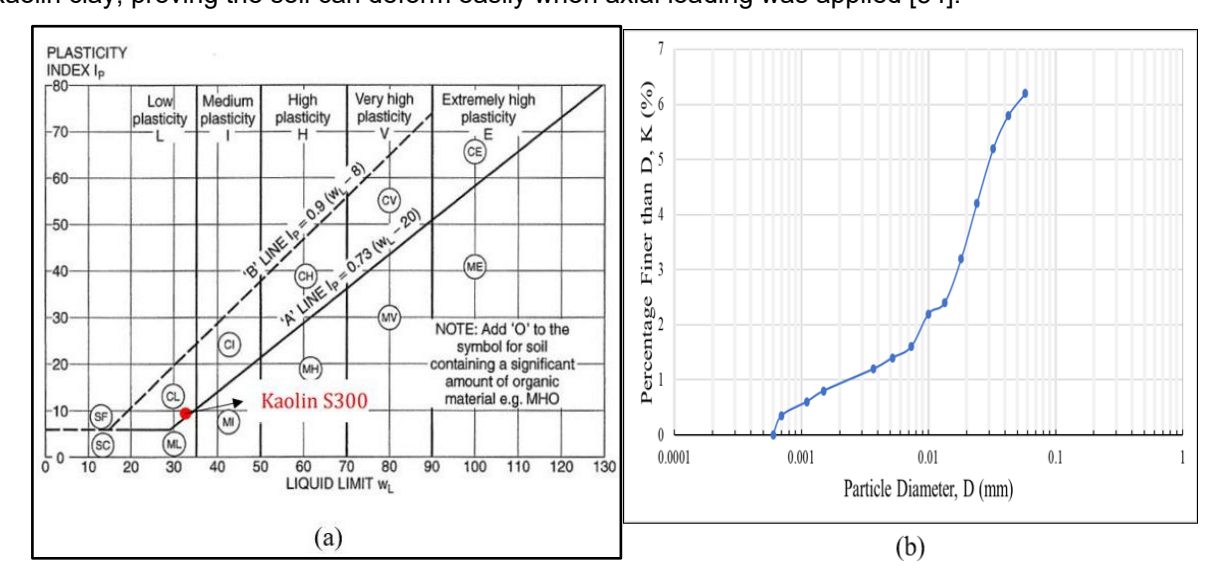
3.1. Engineering Properties of Kaolin Clay S300 and Crushed Coconut Shell

The engineering properties of these materials involved in the research were determined based on the tests as stated in Table 3. The properties of kaolin clay S300 was tabulated in Table 5 while crushed coconut shell properties was tabulated in Table 6.

Table 5. Kaolin clay \$300 properties.

Test	Parameter	Value
Soil Classification	AASHTO	A-6
	USCS (Plasticity Chart)	ML
Atterberg Limit	Plastic Limit, w_p (%)	26
	Liquid Limit, w _L (%)	36
	Plastic Index, Ip (%)	10
Standard Compaction	Optimum Moisture Content, w_{opt} (%)	19.40
	Maximum Dry Density, $\rho_d(max)$ (Mg/m³)	1.55
Small Pycnometer	Specific Gravity, Gs	2.62
Falling Head Permeability	Coefficient of Permeability, k (m/s)	8.96 x 10 ⁻¹²

From this table, it was noticed that the kaolin clay was a soft clay soil. In terms of its particle size, it fell under ML based on the USCS chart, or inorganic silt with very fine sands as shown in Fig. 6 (a). The results were inferred referring to the plastic limit value of 26 % and a liquid limit value of 36 % and hence, obtaining the value of the plastic index was 10 %. Referring to AASHTO, it had A-6 value. This value indicated that kaolin was a clayey soil. Although it was a clayey soil, it was a well-graded soil with more than 75 % of the amount passed through the #200 sieve size based on the hydrometer test as depicted in Fig. 6 (b). The above findings were significant as compared to the results by Syamsul et al. [21], which reported the similar results by inferring kaolin clay S300 was a highly compressible soil. Regarding the Maximum Dry Density (MDD) and Optimum Moisture content (OMC), the compaction graph was plotted and the values were determined according to the graph in Fig. 6 (c). The association of the MDD and OMC values in the coconut shell column preparation process demonstrated a vital role as it provided the fundamental reference between the relationship of water volume required and the kaolin clay to acquire the highest efficiency of product. The falling head permeability test proved that the kaolin clay S300 was less permeable with the value of 8.96 x 10⁻¹² m/s, where it was susceptible to water accumulation issue. As reported by previous results, the authors obtained the value of permeability value at 8.89 x 10⁻¹² m/s from kaolin clay, proving the soil can deform easily when axial loading was applied [34].



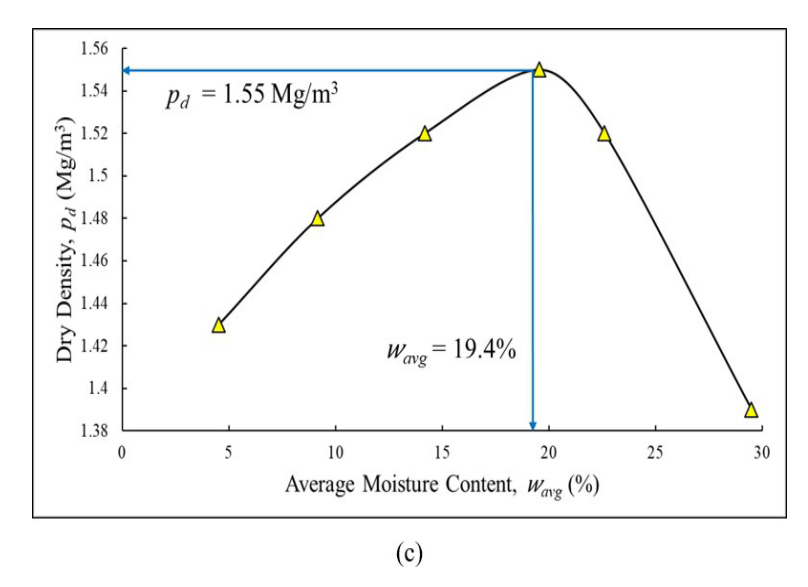


Figure 6. Kaolin clay S300 properties (a) USCS chart (b) Particle size distribution (c) Compaction curve from standard compaction test.

For crushed coconut shell, it was a well graded particle and behaved like gravel or sand type, with A-2 value based on the AASHTO. A-2 signified that this material was a clayey gravel sand, and the majority of the particle size was ranging within 2–9 mm as shown in Fig. 7. The constant head permeability test showed it was a highly permeable material with the value of 2.32 x 10⁻³ m/s, promoting a good drainage system for discharging the excessive accumulated water within itself. The minimum and maximum dry density value of coconut shell obtained from the study were 0.497 g/cm³ and 0.596 g/cm³ respectively, and the values were utilized in the column preparation process. From the obtained values, the in-situ density was generated by applying the raining method, where the average density of coconut shell obtained was 0.58 g/cm³ and therefore, the relative density was approximately 87.50 %. Nonetheless, an average higher value of relative density did not only accelerate the dissipation of excessive pore water pressure generated within the soil, but the compacted coarse material of crushed coconut shell potentially acted a stiffer reinforcement beneath the soil.

Table 6. Crushed coconut shell properties.

Test	Parameter	Value
Soil Classification	AASHTO	A-2
Small Pycnometer	Specific Gravity, Gs	1.70
Relative Density Test	$ ho_{d(min)}$ (g/cm³)	0.497
	$ ho_{d(max)}$ (g/cm³)	0.596
Constant Head Permeability	Coefficient of Permeability, k (m/s)	2.32 x 10 ⁻³

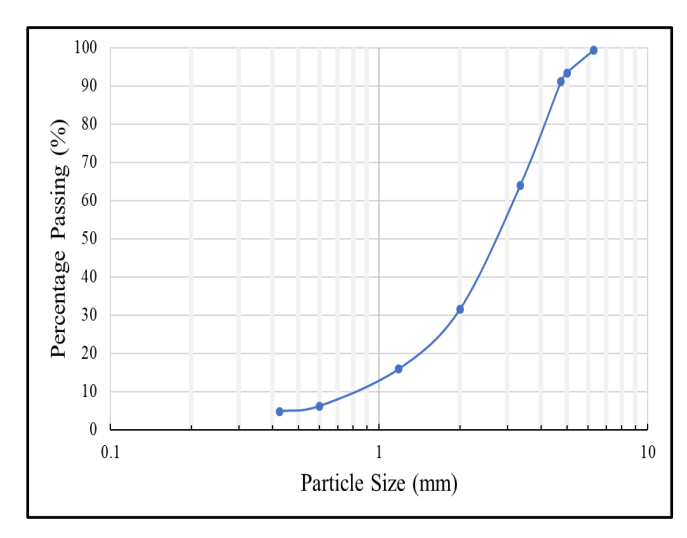


Figure 7. Particle size distribution curve of coconut shell.

3.2. Analysis of Shear Strength Parameters

The shear strength values were obtained from UCT, and further parameters were calculated and analysed. The average deviator stress, exerted loading, strain, stress and shear strength values were analysed with the appropriate graphs and tables. For Table 7, it demonstrated the strain, stress and exerted loading on the control sample, and the reinforced specimens of S1360, S1380, and S13100. The variation of stress with strain against in responds to the exerted load by the UCT machine was plotted in Fig. 8.

Table 1. Parameters	rable 1. Farameters of shear strength for stress, strain and exerted load					
Specimen	Strain (%)	Stress (kPa)	Exerted load (kN)			
Control	1.85	7.12	0.0586			
S1360	2.79	8.35	0.0870			
S1380	2.88	8.98	0.0930			
S13100	2.71	9.15	0.0880			

Table 7. Parameters of shear strength for stress, strain and exerted load

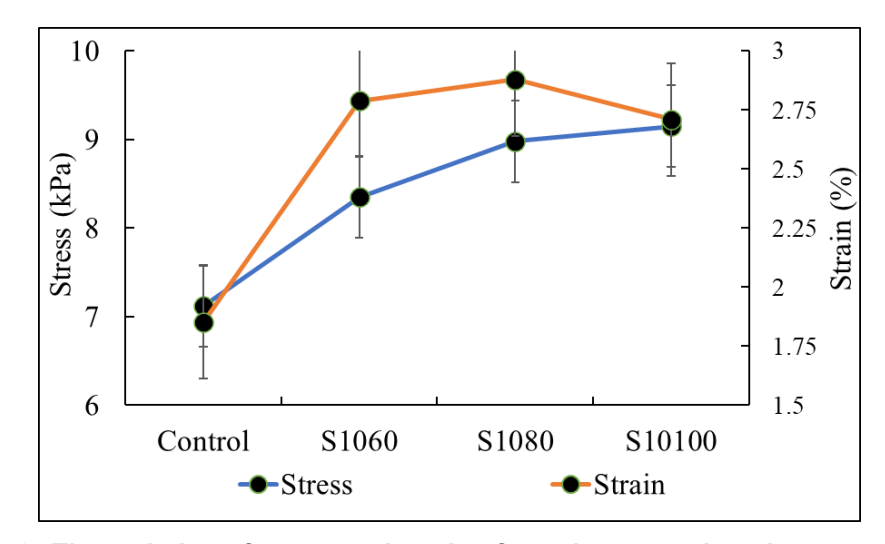


Figure 8. The variation of stress and strain of specimens against the exerted load.

Table 7 showed that the S13100 column was able to withstand the largest stress, 9.15 kPa while the least was by S1360, only recorded 8.35 kPa. The increase in the content of replaced coarse material, crushed coconut shell will directly result in the enhancement of stress. Although the increment trend was observed by increasing the column height, the increment of stress only recorded 0.17 kPa from the S1380 column to the S13100 column which was lesser compared to the increment from the S1360 column to the S1380 column, recorded 0.63 kPa. This may be due to the disturbance of the nature state of kaolin clay, where it was replaced with foreign material, crushed coconut shell and thus causing the reduction of shear strength [35]. From Table 7, it was inferred that the increase of strain value halted at 2.88 %, then decreased to 2.71. The above phenomena was interpreted as the S13100 column was not sheared completely and failure occurred before the axial loading was effectively transferred to the bottom part of the reinforced column. Although the S1380 column was not reinforced thoroughly, the bottom part of the unreinforced soil performed better than the reinforced part of the S13100 column which was attributed to the coarse coconut shell substitution that did not cancel out the effect of soil disturbance during the drilling process. For both strain and exerted load category, the value increased as the column height increased, but showed reduction after the peak value by the S1380 column. The detailed performance of reinforced column was analysed by interpreting the data of shear strength parameter in Table 8. All the shear strength improvement of reinforced specimens, S1360, S1380, and S13100 were computed in accordance to the shear strength value of control specimen.

Table 8. Parameters of shear strength deviator stress, shear strength and its improvement.

	_		
Specimen	Deviator stress (kPa)	Shear strength (kPa)	Shear strength improvement (%)
Control	14.24	7.12	-
S1360	21.36	8.35	17.28
S1380	23.71	8.98	26.12
S13100	21.89	9.15	28.51

As mentioned previously, the shear strength of soil was reduced by the replacement of foreign material, the shear strength values and its improvement were affected by the substitute effect. By using the control sample as the calculation reference, the shear strength improvement showed an increment from 17.28 % to 26.12 %, then increased again to 28.51 %. As reported by the previous study, the authors utilised the single and group bottom ash columns resulted in an identical trend [21]. Coherent to that, the difference between the shear strength improvement rate between the 80 mm and 100 mm column height marked a smaller rate as compared to the 60 mm and 80 mm respectively, where the loosened particles of kaolin soil that incurred by the drilling activity contributed to the reduction of strength of the entire specimen [36]. From the perspective of column parameters, the column height, column diameter, and the amount of replaced coarse material can exert immense influence on the performance of the column through its shear strength value. The analysis continued with the correlation techniques by correlating the shear strength parameters in sub topic 3.3, where it simplified the complexity of the relationship between the dependent and independent variable of an engineering system by statistical method [37].

3.3. Correlation of Shear Strength Improvement versus Column Penetrating Ratio

Referring to Table 8, the highest shear strength improvement was recorded at S13100 column with the value of 28.51 % with the H_c/H_s value of 1.0, followed by the S1380 column with 0.8 H_c/H_s resulted in 26.12 % of improvement rate. The increment of shear strength improvement was directly proportional to the column penetrating ratio, from 0.6 to 1.0 produced the improvement rate of 17.28 % to 28.51 % respectively. Similarly, the S1380 column with a 0.8 of H_c/H_s recorded a moderate value of improvement, with only 26.12 %. This was due to the bulging of the column occurring at the top part of the column extended to 80 mm, whilst the remaining part of the column was less functional to receive the load from the reinforced section. Precisely, a column height with 100 mm coconut shell reinforcement can produce the highest value of improvement, whereas the 60 mm produced the least improvement with 13 mm diameter of kaolin clay. The regression method with the correlation equation of R^2 = 0.9857 was presented in equation (1). Fig. 9 showed the correlation of shear strength improvement versus column penetrating ratio.

$$\Delta Su = 29.693(H_c/H_s) + 0.1618. \tag{1}$$

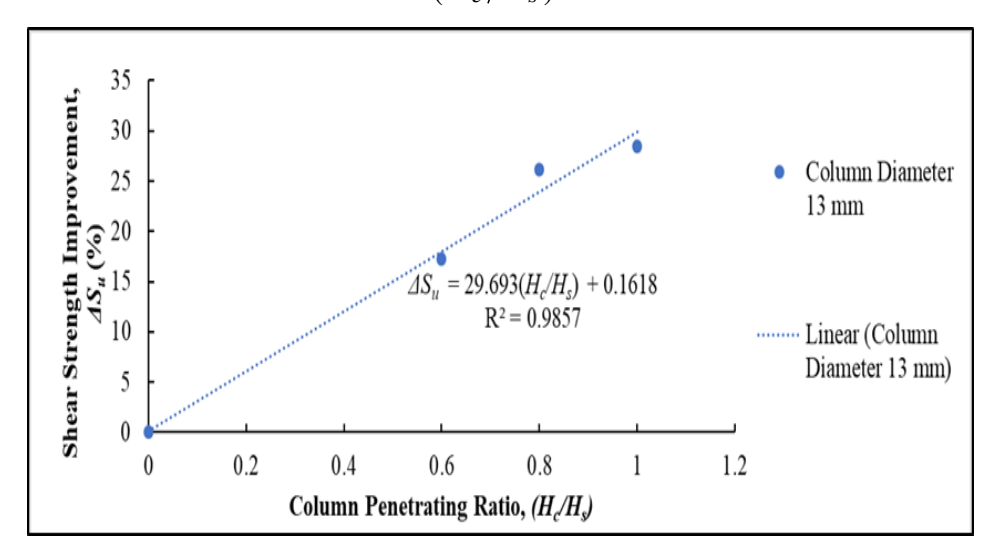


Figure 9. Correlation of shear strength improvement versus column penetrating ratio.

3.4. Correlation of Shear Strength Improvement versus Column Penetrating Ratio

For this sub-topic, the column penetrating height was examined in accordance to the width of the column. The $H_{\rm C}/D_{\rm C}$ ratio varied from 4.6153 to 6.1538, then increased to 7.6923. The favourable value of column height to column diameter ratio lied within the range of 4–6 [38], where in this study it did not really indicate in the range values, where 7.6923 of $H_{\rm c}/D_{\rm c}$ produced the largest shear strength improvement and thus, further study on this specific ratio is required to determine the behaviour of column parameters. Previous research explained the above situation by considering the critical column length factor and the suggested value was within approximately 6 times its diameter value [39], where this study presented about 7.69 times. The obtained ratio of this value was classified as the nature of the coarse material, crushed coconut shell which performed differently as compared to other potential materials for instance bottom ash. Equation (2) showed the correlations of the crushed coconut shell column in accordance with the kaolin clay shear strength improvement with $R^2 = 0.9857$. Fig. 10 showed the correlation of shear strength improvement against column height to column diameter ratio.

$$\Delta Su = 3.8601(H_c/D_c) + 0.1619. \tag{2}$$

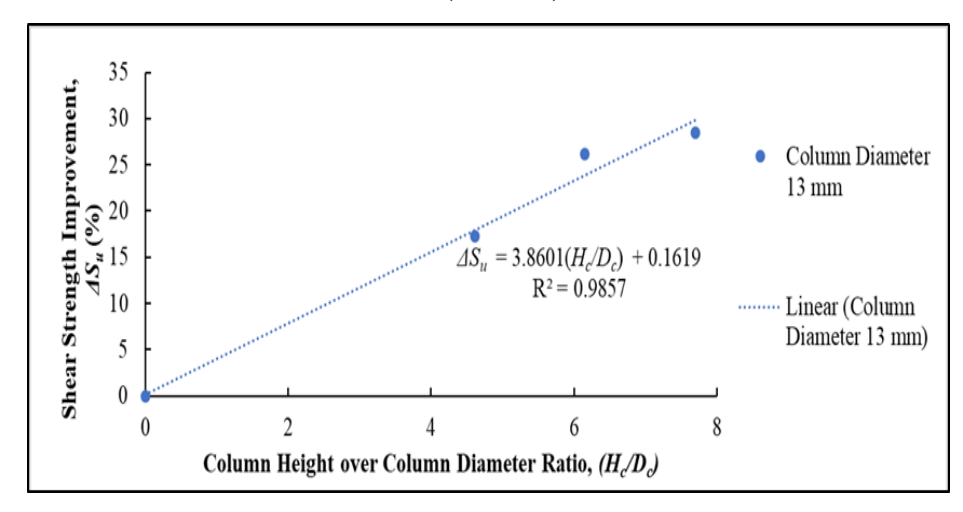


Figure 10. Correlation of shear strength improvement versus column height over column diameter ratio.

3.5. Correlation of Shear Strength Improvement versus Volume Replacement Ratio

Based on Table 4 and 8, the volume replacement ratio with the value of 0.0676 showed the highest rate of shear strength improvement while the least was recorded when the value was 0.0405, yielding a different of shear strength improvement of 11.23 %. From both values, it was noticed that the volume alteration of column was from 2535 π cm³ to 4225 π cm³ or an increment of 66.91 % which produced the shear strength difference of 2.03 kPa. This result data was supported by the study using PP column as a reinforcement material in enhancing the soil bearing capacity of kaolin, where the authors reported the change of about 66.81 % of the volume will generate the additional shear strength value of 4.05 kPa [22]. The additional substituted amount of coarse material where in this study crushed coconut shell increased the capacity of the penetrating column, enhanced the stiffness of the column, and promoted the ability to carry additional load. The more particles of crushed coconut shell inside the specimen, the higher the ability to withstand a larger pressure from the axial loading hence, preventing the earlier failure of the column from occurring during the shearing process. The regression equation (3) showed the value of R^2 = 0.9854. Fig. 11 demonstrated the correlation of shear strength improvement against volume replacement ratio.

$$\Delta Su = 439.38 (V_c/V_s) + 0.1718. \tag{3}$$

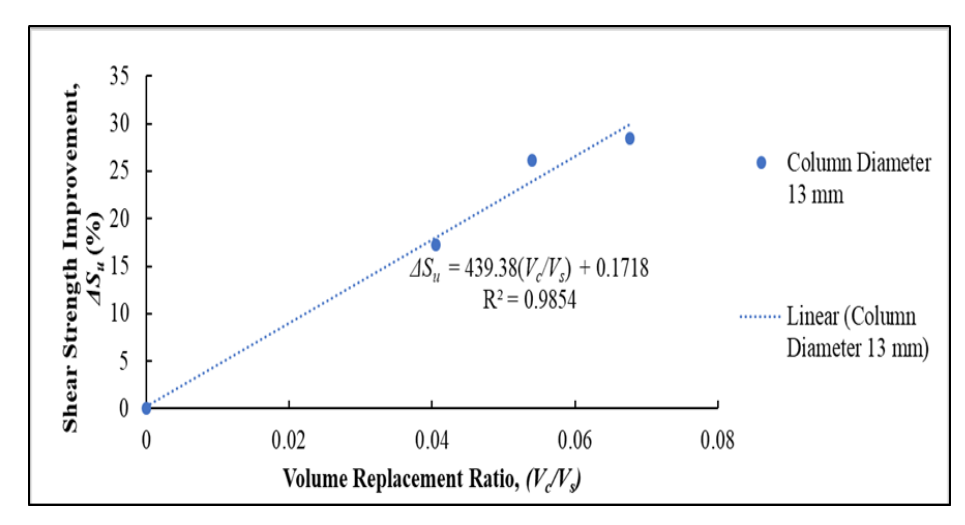


Figure 11. Correlation of shear strength improvement versus volume replacement ratio.

4. Conclusion

This chapter summarised the results gathered from the respective geotechnical tests, which encompassed the determination of the physical and mechanical properties of research materials, kaolin clay S300, and coconut shell, together with the investigation of reinforced specimens via the implementation of UCT. Both of the objectives were achieved and the deduced conclusions were as follows:

- 1. The kaolin clay soil, type S300 was a problematic soft clay soil, which was examined by the soil classification through the AASHTO and USCS plasticity chart. Both standards concluded the kaolin soil was an inorganic silt soil with slight plasticity. In addition, the deployment of standard compaction test verified the kaolin had the OMC of 19.40 %, and a MDD value of 1.55 Mg/m³, produced from the proctor curve. The coefficient of permeability of kaolin also signified it can cause the water accumulation issue, by having an extremely low value of 8.96 x 10⁻¹² m/s.
- 2. The coconut shell that was grinded was analysed through geotechnical approaches and found to behave like a coarse aggregate with the AASHTO value of A-2. This value verified it was a gravel-sand type material, with the coefficient of hydraulic conductivity value of 2.32 x 10⁻³ m/s. The computed relative density value was 87.50 % following the minimum, maximum, and in-situ dry density, suggesting it was a very dense material. Thus, the association of this material was a potential substitute for resolving the soil swelling matter through the provision of additional drainage to the kaolin soil.
- 3. The fabrication of a singular coconut shell column beneath the kaolin clay soil recorded positive results, with the range of shear strength enhancement from 1.23 kPa to 2.03 kPa in reference to the control specimen shear strength value. This study verified the insertion of a singular coconut shell column can prolong the failure of soil, by raising the soil-bearing capacity to 28.51 %. Therefore, the current research suggested the optimum design of reinforced specimen possessed the values H_c/H_s =1.0, H_c/D_c = 7.6923, and V_c/V_s = 0.0676. Coherently, the fully penetrated column design delivered the highest value of improvement, showing that a larger amount of grinded coconut shell was able to distribute the axial load effectively.

References

- Pruett, R.J. Kaolin deposits and their uses: Northern Brazil and Georgia, USA. Applied Clay Science. 2016. 131(2015). Pp. 3–13. DOI: 10.1016/j.clay.2016.01.048
- 2. Karkush, M., Jabbar, A. Improvement of Soft Soil Using Linear Distributed Floating Stone Columns under Foundation Subjected to Static and Cyclic Loading. Civil Engineering Journal (Iran). 2019. 5(3). Pp. 702–711. DOI:10.28991/cej-2019-03091280.
- 3. AL-Ani, S.M.A., Karkush, M.O., Zhussupbekov, A., Al-Hity, A.A. Influence of Magnetized Water on the Geotechnical Properties of Expansive Soil. Lecture Notes in Civil Engineering. 112. Springer Science and Business Media Deutschland GmbH, 2021. Pp. 30–50
- 4. Nicholson, P.G. In Situ Reinforcement2015. 371-387 p. ISBN:9780124080768.
- 5. Turskis, Z., Daniūnas, A., Zavadskas, E.K., Medzvieckas, J. Multicriteria Evaluation of Building Foundation Alternatives. Computer-Aided Civil and Infrastructure Engineering. 2016. 31(9). Pp. 717–729. DOI:10.1111/mice.12202.
- 6. Maltseva, T., Bai, V., Erenchinov, S., Esipov, A., Chumanova, N. Bearing capacity of frame-gantry pile foundations. Magazine of Civil Engineering. 2023. 122(6). DOI:10.34910/MCE.122.7.
- Jawad, S., Karkush, M. Shear strength and chemical properties of soft clayey soil treated with magnetized water. Magazine of Civil Engineering. 2023. 124(8). DOI:10.34910/MCE.124.6.

- 8. Sánchez-Garrido, A.J., Navarro, I.J., Yepes, V. Evaluating the sustainability of soil improvement techniques in foundation substructures. Journal of Cleaner Production. 2022. 351(March). DOI:10.1016/j.jclepro.2022.131463.
- 9. Piccinini, I.D. Ground Improvement with Stone Columns Methods of Calculating Settlement Improvement Factor. University of Glasgow. 2015. (April). DOI:10.13140/RG.2.1.2159.2486.
- 10. Mani, K., Nigee, K. Focus on Ground Improvement. International Journal of Innovative Research in Science, Engineering and Technology. 2013. 2(11). Pp. 6451–6456. URL: www.ijirset.com.
- Boumekik, N.E.I., Labed, M., Mellas, M., Mabrouki, A. Optimization of the ultimate bearing capacity of reinforced soft soils through the concept of the critical length of stone columns. Civil Engineering Journal (Iran). 2021. 7(9). Pp. 1472–1487. DOI:10.28991/cej-2021-03091737.
- 12. Wang, W., Deng, X., Wang, Y., Peng, L., Yu, Z. Impacts of infrastructure construction on ecosystem services in new-type urbanization area of North China Plain. Resources, Conservation and Recycling. 2022. 185(April). Pp. 106376. DOI:10.1016/j.resconrec.2022.106376. URL: https://doi.org/10.1016/j.resconrec.2022.106376.
- Lim, G., Li, C., Ji, X. Chinese financial statecraft in Southeast Asia: an analysis of China's infrastructure provision in Malaysia. Pacific Review. 2022. 35(4). Pp. 647–675. DOI:10.1080/09512748.2020.1868556. URL: https://doi.org/10.1080/09512748.2020.1868556.
- 14. bin Hasan, M., binti Yusuf, N., binti Noor Shahrudeen, N.A., Kassim, A.M.H. Strength of soft clay reinforced with group crushed polypropylene (PP) columns. Electronic Journal of Geotechnical Engineering. 2015. 20(22). Pp. 12291–12308.
- 15. Aljanabi, Q.A., Chik, Z., Kasa, A. Construction of a new highway embankment on the soft clay soil treatment by stone columns in Malaysia. Journal of Engineering Science and Technology. 2013. 8(4). Pp. 448–456.
- Bilal, M., Talib, A. A study on advances in ground improvement techniques. Advances in Geotechnical Engineering. 2016. (April). Pp. 322–330. DOI:10.13140/RG.2.1.4865.4965.
- 17. Karkush, M., Ali, N.A. Electrokinetic enhancement of microbial induced calcite precipitation used in improving the shear strength of soft clay. Smart Geotechnics for Smart Societies. CRC Press, 2023. Pp. 155–163.
- 18. Karkush, M.O., Ali, H.A., Ahmed, B.A. Improvement of unconfined compressive strength of soft clay by grouting gel and silica fume. Springer Series in Geomechanics and Geoengineering. 2018. Pp. 546–550. DOI:10.1007/978-3-319-97112-4_122.
- 19. Karkush, M.O., Yassin, S. Using Sustainable Material in Improvement the Geotechnical Properties. 15(4)2020. 2208–2222 p.
- BRÛLÉ, S., SERANAJ, A., PIQANI, A. Seismic Behavior of a Building Founded on Loose Soil Improved by Stone Columns. Researchgate.Net. 2020. (December). URL: https://www.researchgate.net/profile/Stephane-Brule/publication/347648602_Seismic_Behavior_of_a_Building_Founded_on_Loose_Soil_Improved_by_Stone_Columns_INTE_RNATIONAL_SYMPOSIUM_ON_DURRES_EARTHQUAKES_AND_EUROCODES/links/5fe2f160299bf1408837574d/Seismic-Beh
- Syamsul, M., Zaini, I., Hasan, M., Nursyafiqah, W., Wan, B. Utilization of bottom ash waste as a granular column to enhance the lateral load capacity of soft kaolin clay soil. Environmental Science and Pollution Research. 2023. (February). DOI:10.1007/s11356-023-25966-x. URL: https://doi.org/10.1007/s11356-023-25966-x.
- 22. Hasan, M., Zaini, M.S.I., Hong, N.A.W., Wahab, A., Masri, K.A., Jaya, R.P., Hyodo, M., Winter, M.J., Sholichin, M., Haribowo, R. Sustainable ground improvement method using encapsulated polypropylene (PP) column reinforcement. IOP Conference Series: Earth and Environmental Science. 2021. 930(1). DOI:10.1088/1755-1315/930/1/012016.
- Verma, S.K., Shrivastava, S. Use of coconut shell as partly substitution of coarse aggregate An experimental analysis. AIP Conference Proceedings. 2019. 2158(September). DOI:10.1063/1.5127145.
- 24. Gunasekaran, K., Kumar, P.S., Lakshmipathy, M. Mechanical and bond properties of coconut shell concrete. Construction and Building Materials. 2011. 25(1). Pp. 92–98. DOI:10.1016/j.conbuildmat.2010.06.053. URL: http://dx.doi.org/10.1016/j.conbuildmat.2010.06.053.
- 25. Mochida, Y., Olabamiji, O.J., Kasahara, K. Study on Development of Soil Improvement Pile Method Using Recycled Soil. International Journal of GEOMATE. 2021. 20(82). Pp. 28–33. DOI:10.21660/2021.82.Gx249.
- 26. Chai, X.J., Deng, K., He, C.F., Xiong, Y.F. Laboratory model tests on consolidation performance of soil column with drained-timber rod. Advances in Civil Engineering. 2021. 2021. DOI:10.1155/2021/6698894.
- 27. Zukri, A., Nazir, R. Sustainable materials used as stone column filler: A short review. IOP Conference Series: Materials Science and Engineering. 2018. 342(1). DOI:10.1088/1757-899X/342/1/012001.
- 28. Gunasekaran, K., Kumar, P.S., Lakshmipathy, M. Study on properties of coconut shell as an aggregate for concrete Self-compacting lightweight concrete View project Coconut shell concrete View project .Study on Pruperties of Goconut Shell as an gate fur Concrete. 2011. (January 2011). URL: https://www.researchgate.net/publication/284088249.
- 29. Sujatha, A., Balakrishnan, S.D. Properties of Coconut Shell Aggregate Concrete: A Review. 2021. 83. Pp. 759–769. DOI:10.1007/978-981-15-5644-9 60.
- Gupta, A., Gupta, N., Shukla, A., Goyal, R., Kumar, S. Utilization of recycled aggregate, plastic, glass waste and coconut shells in concrete - A review. IOP Conference Series: Materials Science and Engineering. 2020. 804(1). DOI:10.1088/1757-899X/804/1/012034.
- 31. Zaini, M.S.I., Hasan, M. Effect of Optimum Utilization of Silica Fume and Lime On the Stabilization of Problematic Soils. International Journal of Integrated Engineering. 2023. 15(1). Pp. 352–366. DOI:10.30880/ijie.2023.15.01.032.
- 32. Damoerin, D., Prakoso, W.A., Utami, Y. Improving shear strength of clay by using cement column reinforcement under consolidated undrained test. International Journal of Technology. 2015. 6(4). Pp. 709–717. DOI:10.14716/ijtech.v6i4.1206.
- 33. Gunasekaran, K., Annadurai, R., Kumar, P.S. Plastic shrinkage and deflection characteristics of coconut shell concrete slab. Construction and Building Materials. 2013. 43. Pp. 203–207. DOI:10.1016/j.conbuildmat.2013.02.019. URL: http://dx.doi.org/10.1016/j.conbuildmat.2013.02.019.
- 34. Hoque, M.I., Hasan, M., Mim, N.J. Shear Strength of Soft Clay Reinforced With Single Encased Stone Dust Columns. Jurnal Teknologi. 2023. 85(5). Pp. 27–34. DOI:10.11113/jurnalteknologi.v85.19879.
- Najjar, S.S. A State-of-the-Art Review of Stone/Sand-Column Reinforced Clay Systems. Geotechnical and Geological Engineering. 2013. 31(2). Pp. 355–386. DOI:10.1007/s10706-012-9603-5.
- 36. Hasan, N.M., Yee, M. Stabilization of Soft Clay Soil by the Reinforcement of Single Bottom Ash Silica Fume (BASF) Column. Journal of Rehabilitation in Civil Engineering. 2024. 12(3). Pp. 117–131. DOI:10.22075/jrce.2024.32181.1925. URL: https://creativecommons.org/licenses/by/4.0/.

- 37. Egbe, J.G., Ewa, D.E., Ubi, S.E., Ikwa, G.B., Tumenayo, O.O. Application of multilinear regression analysis in modeling of soil properties for geotechnical civil engineering works in Calabar South. Nigerian Journal of Technology. 2018. 36(4). Pp. 1059. DOI:10.4314/njt.v36i4.10.
- 38. Hasan, M., Jusoh, W.N.W., Chee, W.S., Hyodo, M. The undrained shear strength of soft clay reinforced with group encapsulated lime bottom ash columns. International Journal of GEOMATE. 2018. 14(46). Pp. 46–50. DOI:10.21660/2018.46.45208.
- 39. Najjar, S.S., Sadek, S., Maakaroun, T. Effect of Sand Columns on the Undrained Load Response of Soft Clays. Journal of Geotechnical and Geoenvironmental Engineering. 2010. 136(9). Pp. 1263–1277. DOI:10.1061/(asce)gt.1943-5606.0000328.

Information about the authors:

Ng Jun Shen, PhD

ORCID: https://orcid.org/0000-0002-6113-1237

E-mail: jshenng98@gmail.com

Muzamir Hasan, PhD

ORCID: <u>https://orcid.org/0000-0002-2700-236X</u>

E-mail: muzamir@ump.edu.my

Nurrul Nisya Anuar,

E-mail: <u>nurrulnisyaanuar@gmail.com</u>

Received 10.11.2023. Approved after reviewing 26.11.2024. Accepted 29.11.2024.



Magazine of Civil Engineering

ISSN 2712-8172

journal homepage: http://engstroy.spbstu.ru/

Research article UDC 539:519.3:624.04 DOI: 10.34910/MCE.132.5



Energetic basis in rational constructions projection

L.A. Panchenko¹ 🖾 🔟 . T.Y. Druzhinina² 🔟





- ¹ Belgorod State Technological University named after V.G. Shukhov, Belgorod, Russian Federation
- ² National Research Irkutsk State Technical University, Irkutsk, Russian Federation
- ∠ Panchenko.bstu@mail.ru

Keywords: ecologic approach, industrial problems, durability, load-bearing structures, variational principles, configuration, material module

Abstract. The theory of designing rational load-bearing structures from the standpoint of strength, durability, manufacturability, and material consumption has too much of an energy basis. New variational principles operate at all levels of designing the configuration of load-bearing structures: topology, geometry, parameters of elements with parallel selection of materials. They can also be used for rational distribution of load on the structure. The study examined the foundations of new variational principles of synthesis of supporting structures with the content of an objective criterion of optimality of their practical application. Based on this, a rational energy principle was selected in the design of supporting structures, as well as algorithms for the development of rational systems focused on software design. The obtained dependencies as a result of the study allow to obtain a rational solution in strength, durability, manufacturability, and material consumption, which in turn helps to reduce the cost of construction of buildings and structures, as well as the costs of their reconstruction. Also, the proposed algorithms for the development of rational systems are aimed at software design.

Funding: This work was realized in the framework of the Program "Priority 2030" on the base of the Belgorod State Technological University named after V. G. Shukhov. The work was realized using equipment of High Technology Center at BSTU named after V. G. Shukhov.

Citation: Panchenko, L.A., Druzhinina, T.Y. Energetic basis in rational constructions projection. Magazine of Civil Engineering. 2024. 17(8). Article no. 13205. DOI: 10.34910/MCE.132.5

1. Introduction

The object of this study is new variation principles for the synthesis of load-bearing structures with the content of an objective criterion for the optimality of their practical application.

Technical progress is driven by the development of scientific knowledge in advanced industries. The art of construction primarily ensures the load-bearing capacity of structures associated with the rational use of the materials used. On this basis, optimal design of structures was developed [1].

In creating harmony between the environment and human society, an important role is played by the design of technical systems and structures based on the natural principles of structure formation. The design of rational load-bearing structures should be associated with the direct use of the principles that govern the deformation of a solid body. Common to artificial and natural systems is the principle of stationary action [2-4].

The natural constants π , e, Φ can be considered as discrete manifestations of the laws of structure formation arising from the mentioned principle [5].

The presence of round bodies in nature led to the birth of the number π , which expresses the ratio of the circumference to the diameter. The well-known isoperimetric problem of Dido is associated with the shape of a thread of a given length, covering the largest area. The desired line is a circle (in the case of a closed thread) and an arc of a circle (in the case of an open thread).

Equally widespread is the number e – the base of natural logarithms. In technology, a formula is known for the cross-sectional area of beam of equal resistance, stretched by force and its own weight.

The constants π and e are related by the Euler formula:

$$e^{2\pi i} = 1, (1)$$

which testifies to their natural unity.

The golden ratio used in the creations of man and present in the organization of nature has a long history. It corresponds to such a division of an integer into two parts when the ratio of the larger part to the smaller one is equal to the ratio of the whole to the larger part $(\Phi = 1.618033...)$.

In the 13th century, the Italian mathematician L. Fibonacci discovered a sequence of numbers, in which each subsequent component is equal to the sum of the two previous ones. I. Kepler supplemented this discovery with the fact that the ratio of adjacent components of this sequence in the limit tends to the golden ratio.

The golden ratio is an irrational value (like π , e) and symbolizes irrationality in natural proportions, while the Fibonacci numbers emphasize the wholeness in the organization of nature. In general, both patterns reflect the dialectical unity of heterogeneous principles – continual and discrete.

Formula

$$\Phi = 2\cos\frac{\pi}{5},\tag{2}$$

together with formula (1) testify to the organic unity of the three constants.

Ancient architects, not having a scientific explanation of the properties of the golden ratio, rather applied it intuitively under the influence of the harmony and beauty of nature's creations. There is a hypothesis of informational resonance: if the shape of the perceived object contains the golden ratio, then the brain is "tuned" to it. The purpose of the analysis of the uncertainty of the state of a technical system is to translate the uncertainty of the initial parameters and assumptions used when the risk assessment into the uncertainty of the results.

Relevance lies in the fact that the ratios obtained during the study allow us to obtain a rational solution from the standpoint of strength, durability, manufacturability, and material consumption, which in turn helps to reduce the cost of constructing buildings and structures, as well as the costs of their reconstruction.

The purpose of the study is to present the foundations of new variation principles for the synthesis of load-bearing structures with the content of an objective criterion for the optimality of their practical application.

The following objectives were addressed within the study:

- 1. Consideration of new variation principles of structure formation and load arrangement in terms of their practical application;
- 2. Selection of a rational energy principle in the design of load-bearing structures;
- 3. Selection of algorithms for the development of rational systems that are focused on software design.

2. Methods

To create a fundamental theory of the structure formation of load-bearing structures, a high level of development of mathematics, in particular, the calculus of variations, was necessary. It works effectively in mechanics. Variational principles have a deep theoretical significance, denoting the energy basis of the organization of matter.

The energy gives a synergistic understanding of the golden ratio. The level of organization of matter is estimated by the ratio of chaos and order in an entropy measure. Harmony function

$$P = \frac{S}{S_{\text{max}} - S},\tag{3}$$

includes the entropy S, determined by the Boltzmann-Shannon formula, and the maximum entropy of the system S_{max} , corresponding to the equiprobability of all its states (chaos). The function P varies from zero to infinity.

Limitation function

$$R = \frac{S_{\text{max}} - S}{S_{\text{max}}},\tag{4}$$

decreases from 1 to 0. Harmony corresponds to the intersection of the curves P and R. In this case, the proportion of chaos is 0.382, and the proportion of order is 0.618 (golden proportion).

The unity of the physical forms of the motion of matter reflects the general physical principle, from which particular laws follow. This is the principle of stationary action (according to Hamilton). Differences in the forms of motion of matter reflect the Lagrange functions chosen on the basis of generalization of experimental data. These functions have energy content.

A special case of the principle of stationary action is the principle of possible work, the mathematical expression of which is:

$$\delta U - \delta T = 0, (5)$$

where δT and δU are variations of the functionals of the introduced mechanical energy and potential strain energy. They depend on the increments of a number of parameters: 1) displacements, 2) internal forces, 3) body configuration, 4) material moduli, 5) load. The first two factors are taken into account when formulating the principle of possible displacements (the Lagrange principle) and the principle of possible changes in the stress state (the Castigliano principle). Both are extreme principles and are used to analyze the stress-strain state of structures.

The remaining three factors are aimed at the formulation of variational principles related to the problem of structure formation and the rational distribution of the load assessment into the uncertainty of the results.

3. Results and Discussion

The functional aspect of analyzing the stress-strain state of a structure involves Euler-Lagrange equations and natural boundary conditions derived from established deformation theory equations and boundary conditions. However, for novel problem types, additional equations are introduced into the functional framework to account for variations in system energy concerning changes in configuration, material elastic moduli, and load distribution. Ensuring functional stationarity concerning variable parameters necessitates the incorporation of additional conditions, typically in the form of coupling equations, imposed on the desired functions ψ. These conditions encompass factors, such as stress-strain state functions, configuration, material elastic moduli, and load distribution, thereby facilitating a comprehensive analysis of structural behavior under varying conditions:

$$\varphi(\overrightarrow{\psi}) = 0, \tag{6}$$

$$\varphi(\overrightarrow{\psi}) = 0, \tag{6}$$

$$\int_{\omega} \varphi(\overrightarrow{\psi}) d\omega = c, \tag{7}$$

where ω is the admissible region of integration, c is a given constant.

Conditions (6) and (7) encompass geometric constraints, design specifications, load restrictions, and functional requirements for the structure, expressed through a combination of algebraic, differential, and integral equations. To address a variational problem with these additional conditions, the Lagrange multiplier method is employed to transform it into an equivalent free variational problem.

A variational problem with additional conditions is reduced to a free variational problem by means of the Lagrange multiplier method. In this case, this can be interpreted as a generalization of the principles of Lagrange and Castigliano for cases of expanding the functional space due to configuration, material moduli, and load fields.

If $J_1(J_2)$ is a functional corresponding to the Lagrange (Castigliano) principle, and λ is the Lagrange multiplier, then the functionals of generalized principles have the form:

$$J_1^* = J_1 + \int_V \vec{\lambda}^T \vec{\varphi} dV, \tag{8}$$

$$J_2^* = J_2 + \int_V \vec{\lambda}^T \vec{\varphi} dV, \tag{9}$$

where V is the volume of the body. Under condition (6), the Lagrange multiplier λ is a variable. Under condition (7), the multiplier λ is a constant value (isoperimetric problem).

Following the theory of the calculus of variations, the possible variations of the configuration functions, material moduli, and load are infinitesimal changes in these functions that satisfy the directive requirements for the construction, material, load, and differentiability requirements.

Consequences arising from the stationarity of the functional (J_1) include: 1) equilibrium equations within the body's volume and static boundary conditions; 2) coupling equations (6) or (7); 3) equations governing structure formation or loading systems.

The variational principle of structure formation based on the Lagrange principle has the following formulation: the potential energy of the system in the position of stable equilibrium reaches an absolute minimum in terms of displacements in the functional space, expanded due to the fields of configuration functions and (or) material moduli. This corresponds to the moment when the load-bearing structure acquires maximum rigidity indicators, so that at the stationarity point the functional has a minimax, namely minimum in terms of displacement functions of maxima in terms of the configuration and (or) material moduli function.

The formulation of new variational principles for the synthesis of load-bearing structures and the formation of the load in the presented form was carried out by A.G. Yuriev in 1982 [6]. The special cases that took place included the formulation of isoperimetric problems of determining the geometric parameters of structures [7].

The new approach to solving design problems excludes the adoption of any criterion a priori. Its role is played by the equation of structure formation (location of the load), which, as mentioned above, is a consequence of the stationarity of the functional of the variational problem under consideration.

Thus, the criterion of minimum volume (mass, cost) in the established optimal design loses its force. With it, there is no guarantee that the goal functional will achieve a global extremum due to the possible absence of the convexity property.

A sufficient condition for achieving this objective can only be attained through integrating an energy based approach into the optimal design process, aligning with the duality inherent in constrained extremum problems with integral constraints [8–10]. Consequently, formulating the volume minimization problem aligns precisely with the overarching physical principle of stationary action, albeit under restricted circumstances. The new variational principles ensure a global minimum in the volume (or cost) of homogeneous material. In specific instances, the structure can exhibit uniform stress distribution throughout its entirety. As per Vasyutinskii's theorem [11], applicable to linearly elastic bodies, the structure possesses a minimum potential energy of deformation. Given this energy is directly proportional to the body's volume, minimizing volume serves as a rational criterion in this context.

The need to put into circulation a new method of structure formation is confirmed by comparison using another, the ordinary criterion [12–14].

Example 1. The console, having a length of I = 2 m, is loaded at the end with a moment M = 50 kN·m. The cross section of the beam is presupposed in the form of an I-beam with the given: wall thickness 2.2 cm (= $2t_1$) and shelf height t_2 = 1 cm. The relative deflection of the console end is set

 f_0/l = 0.006. The modulus of elasticity of the material E = 2·105 MPa. It is required to determine the height of the section h and the width of the shelf b.

It is known that the deflection at the end of the console is:

$$f_0 = \frac{MI^2}{2EI},\tag{10}$$

where I is the moment of inertia of the section. The absolute value of stresses in the extreme longitudinal fibers is equal to:

$$\sigma_0 = \frac{M}{I} \frac{h}{2}.\tag{11}$$

Consequently,

$$\frac{f_0}{l} = \frac{\sigma_0 l}{Eh},\tag{12}$$

$$\sigma_0 = \frac{f_0}{I} E h \frac{1}{I} = 60h. \tag{13}$$

Substituting expression (13) into the formula

$$\sigma_0 = \frac{M}{W},\tag{14}$$

where W is the moment of resistance of the cross-section during bending, we find the expression b, and then the area of the cross-section (taking into account formula (13)):

$$A = 2t_1h + \left[0.1Mt_2 - 2t_1t_2\left(h - 2t_2\right)^3\right] \left(3h^2t_2 - 6ht_2^2 + 4t_2^3\right)^{-1} - 4t_1t_2.$$
 (15)

From the condition of minimum cross-sectional area (15) for given values of M, t_1 , t_2 follows the equation:

$$h^4 - 4h^3 + 6h^2 - 22730h + 22730 = 0, (16)$$

whence h = 29.32 cm. In this case, b = 1.07 cm, A = 62.24 cm².

The same values of b and h will be obtained by solving the isoperimetric problem for $A = 62.24 \text{ cm}^2$. Let us determine the value b = 33.32 - 1.1h and substitute it into the expression for the moment of inertia I, which we will introduce into the energy functional:

$$J_2 = \frac{M^2 l}{2EI}. ag{17}$$

From the condition $\frac{\partial J_2}{\partial h} = 0$ follows the equation:

$$h^2 - 30.29h + 28.95 = 0$$
.

whence h = 29.32 cm. In this case, b = 1.07 cm (the confluence of I-beam).

In this case, the direct use of the $\,J_2\,$ – functional turned out to be acceptable. Therefore, there was no need to use the method of Lagrange multipliers.

Example 2. In the condition of example 1, instead of the given value f_0/l , we introduce the admissible stress σ_{adm} = 160 MPa.

From the strength condition, the expression $\,b\,$ can be derived, so that the cross-sectional area is equal to

$$A = 2t_1h + \left[\frac{6Mt_2h}{\sigma_{adm}} - 2t_1t_2\left(h - 2t_2\right)^3\right] \left(3h^2t_2 - 6ht_2^2 + 4t_2^3\right)^{-1} - 4t_1t_2.$$
 (18)

The condition $\partial A/\partial h=0$ implies an equation that, for given values of $M,\ t_1,\ t_2,\ \sigma_{adm}$ takes the form:

$$h^4 - 4h^3 - 420.13h^2 - 6h + 568.18 = 0,$$
 (19)

whence h = 22.6 cm In this case, b = 8.26 cm, A = 61.84 cm², moment of inertia I = 3530.9 cm⁴.

Let us now solve the isoperimetric problem for $A = 61.84 \text{ cm}^2$. Having determined the value b = 33.32 - 1.1h, let us substitute it into the expression for the moment of inertia I, which we introduce into the functional (17).

From the condition $\frac{\partial J_2}{\partial h} = 0$ follows the equation:

$$h^2 - 30.11h + 28.77 = 0, (20)$$

whence h = 29.13 cm. In this case, b = 1.08 cm, = 4088.7 cm⁴, σ_{adm} = 178.1 MPa.

The solutions do not coincide, since in the case of minimizing the cross-sectional area, the condition σ_{adm} = 160 MPa has no energy meaning, which eliminates the duality of the problem statement. The problem statement in example 1 is deprived of this deficiency.

Yuriev's variational principles and the theory of structure formation of load-bearing structures based on them changed the nature of design. The subjective design criteria, which are speculative in nature, have been replaced by the laws of structure formation arising from the general physical principle of stationary action.

Designing a structure configuration within the specified requirements includes determining its topology, geometry, and element parameters [15, 16].

The topology of rod systems provides for the mutual arrangement of nodes and the way they are connected to each other to form a geometrically unchanging structure. The variational principles of structure formation make it possible to reveal a rational construction from the allowed variants by studying the corresponding energy functionals.

In the case of a linear-elastic formulation of the problem, the values of the potential strain energy are compared for directive geometric parameters. The problem statement can be extended by varying some geometric parameters within each topology variant.

In rod systems, it is possible to change the sign of longitudinal forces in some rods by varying the geometric parameters. When a stretched rod passes into a compressed one, in addition to strength, it is necessary to ensure the stability of its equilibrium.

In the case of an isoperimetric problem for a truss under the generalized variational Castigliano principle, the functional has the form [17–20]:

$$J_2^* = \sum_{i=1}^n \frac{N_i^2 l_i}{2E\varphi_i^2 A_i} + \lambda \sum_{i=1}^n A_i l_i,$$
 (21)

where n is the number of rods of length l_i , having a cross-sectional area A_i and longitudinal forces N_i , ϕ_i is the coefficient of reduction of the design resistance.

This problem is solved in an iterative way. The coefficient φ is assigned in accordance with the regulatory requirements for ensuring of the stability of the belt and lattice rods.

Based on Yuriev's variational principles [6], the problem of structure formation of dispersely and discretely reinforced material was solved [21–26]. In the case of dispersed reinforcement, the desired is the modulus of longitudinal elasticity of the composite material, which corresponds to a certain nature of fiber reinforcement [27–30].

In the case of discrete (bar) reinforcement, the generalized functional J_1^* contains the term $\frac{1}{2}\sum_i S_i q_i$, where S_i is the internal force in the reinforcing bar, q is the corresponding displacement. The

generalized functional J_2^* contains the term $\sum_i \frac{S_i^2 l_i}{2B_i}$, where l_i is the length of the reinforcing bar, B_i is

the stiffness of its cross-section, which has a specific expression depending on the type of deformation (in tension $B_i = EA_i$, where E is the modulus of longitudinal elasticity of the reinforcing material, A_i is the cross-sectional area of the rod) [31–34].

4. Conclusion

Based on the conducted research, the following has been established:

- The considered new variational principles of structure formation and load location have a strict physical basis – the principle of stationary action. The solution of practical problems based on them does not require the introduction of any criterion, which is typical for pre-existing design methods. First of all, this concerns the formulation of design tasks with an especially economic criterion (minimum volume, mass, cost).
- 2. The proposed energy principle in the design of load-bearing structures makes it possible to obtain a rational solution from the standpoint of strength, durability, manufacturability, and material consumption and helps to reduce the cost of constructing buildings and structures, as well as the costs of their reconstruction. In turn, this contributes to the implementation of an ecological approach to the habitat with the effective use of building materials, energy, space, and the entire ecological system.
- 3. Rational systems development algorithms aimed at software design are considered.

References

- Korobko, V.I., Morozov, S.A. Optimal design of plates with step-variable stiffness in the limit state. Building and reconstruction. 2007. 4/16(538). Pp. 39–43.
- 2. Yuriev, A.G. Yestestvennyy faktor optimizatsii konstruktsii [Natural factor of optimization of constructions]. Belgorod: Publishing house of BSTU named after V.G. Shukhov, 2003. 109 p.
- Kulikova, E.Yu., Balovtsev, S.V., Skopintseva, O.V. Complex estimation of geotechnical risks in mine and underground construction. Sustainable Development of Mountain Territories. 2023. 15(1). Pp. 7–16. DOI: 10.21177/1998-4502-2023-15-1-7-16
- Kulikova, E.Yu., Konyukhov, D.S. On the determination of buildings technological deformations in geotechnical construction. Sustainable Development of Mountain Territories. 2022. 14(2). Pp. 187–197. DOI: 10.21177/1998-4502-2022-14-2-187-197
- 5. Korobko, V.I., Emelianov, S.T., Chernyaev, A.A. Korobko, V.I., Emelianov, S.T., Chernyaev A.A. Golden proportion and problems of harmony of systems [Golden proportion and problems of harmony of systems]. Kursk: The Southwest State University, 2013. 444 p.
- 6. Yuriev, A.G. Mekhanika sooruzheniy: sintez konstruktsiy [Structures mechanics: synthesis of constructions]. Moscow: Publishing house of MISI, 1982. 100 p.
- Berdichevsky, V. Variational Principles of Continuum Mechanics. Springer. Berlin, Heidelberg, 2009. 430 p. DOI: 10.1007/978-3-540-88469-9
- Klyuev, R.V. System analysis of calculation methods for power supply systems in quarry points. Sustainable Development of Mountain Territories. 2024. 16(1). Pp. 302–310. DOI: 10.21177/1998-4502-2024-16-1-302-310
- Zhukov, I.A., Golikov, N.S., Martyushev, N.V. Design rationalization of the scraper conveyor section by means of an automated method of strength characteristics analysis. Sustainable Development of Mountain Territories. 2022. 14(1). Pp. 142–150. DOI: 10.21177/1998-4502-2022-14-1-142-150
- Klyuev, R.V., Khetagurov, V.N., Gavrina, O.A., Plieva, M.T. Integrated analysis of electric energy demand of autogenous grinding mills at concentration factories. MIAB. Mining Information and Analytical Bulletin. 2023. 5–1. Pp. 145–156. DOI: 10.25018/0236_1493_2023_51_0_145
- Wasiutyński, Z. On the congruency of the forming according to the minimum potential energy with that according to the equal strength. Bulletin de L'Academie Polonaise des Sciences. Series des Sciences Techniques. 1960. 6. Pp. 259–268.
- Yuriev, A.G. Variatsionnyye printsipy mekhaniki konstruktsiy [Variational principles of structures mechanics]. Belgorod: Publishing House of BelgTASM, 2002. 90 p.
- Tamrazyan, A.G., Alekseytsev, A.V. Multi-criteria optimization of reinforced concrete beams using genetic algorithms. IOP Conference Series: Materials Science and Engineering. 2020. 869(5). Article no. 052027. DOI: 10.1088/1757-899X/869/5/052027
- Yuriev, A.G., Zinkova, V.A. Loading optimization of the metal trusses. Bulletin of Belgorod State Technological University named after V.G. Shukhov. 2020. 5(2). Pp. 56–61. DOI: 10.34031/2071-7318-2020-5-2-56-61

- Teplyakova, A.V., Zhukov, I.Al., Martyushev, N.VI. Application of drilling machines with impact cam mechanism in various mining and geological conditions. Sustainable Development of Mountain Territories. 2022. 14(3). Pp. 501–511. DOI: 10.21177/1998-4502-2022-14-3-501-511
- Ismagilov, R.I., Zhuravlev, A.G., Furin, V.O. Designing modern Russian crushing and transfer units for conveyor ore transportation systems. Russian Mining Industry. 2024. 3. Pp. 48–55. DOI: 10.30686/1609-9192-2024-3-48-55
- Zinkova, V.A. Optimization of the Structure of Flat Metal Tube Trusses. Lecture Notes in Civil Engineering. 95. Innovations and Technologies in Construction. BUILDINTECH BIT 2020. Springer. Cham, 2021. Pp. 213–218. DOI: 10.1007/978-3-030-54652-6
 32
- 18. Begich, Y.E., Klyuev, S.V., Jos, V.A., Cherkashin, A.V. Fine-grained concrete with various types of fibers. Magazine of Civil Engineering. 2020. 5(97). Article no. 9702. DOI: 10.18720/MCE.97.2
- Panchenko, L.A. Calculation of fiber-reinforced concrete structures taking into account physical nonlinearity. Bulletin of Belgorod State Technological University named after V.G. Shukhov. 2022. 7(1). Pp. 44–50. DOI: 10.34031/2071-7318-2021-7-1-44-50
- Panchenko, L.A. Concrete and Fiber-Reinforced Concrete in a Cage Made of Polymers Reinforced with Fibers. Lecture Notes in Civil Engineering. 95. Innovations and Technologies in Construction. BUILDINTECH BIT 2020. Springer. Cham, 2021. Pp. 131–136. DOI: 10.1007/978-3-030-54652-6 20
- 21. Brosens, K., Ahmed, O., Van Gemert, D. Strengthening of Concrete Structures with Externally Bonded Reinforcement Design Philosophy and Practical Applications. 10th International Congress on Polymers in Concrete. Honolulu, 2001. Pp. 103–107.
- 22. Lorenzis, L. de., Miller, B., Nanni, A. Bond of FRP laminates to concrete. ACI Material Journal. 2001. 98(3). Pp. 256-264.
- 23. Ma, J., Yuan, H., Zhang, J., Zhang, P. Enhancing concrete performance: A comprehensive review of hybrid fiber reinforced concrete. Structures. 2024. 64. Article no. 106560. DOI: 10.1016/j.istruc.2024.106560
- 24. Nelyubova, V.V., Babayev, V.B., Alfimova, N.I., Usikov, S.A., Masanin, O.O. Improving the efficiency of fibre concrete production. Construction Materials and Products. 2019. 2(2). Pp. 4–9. DOI: 10.34031/2618-7183-2019-2-2-4-9.
- Martyushev, N.V., Malozyomov, B.V., Sorokova, S.N., Efremenkov, E.A., Valuev, D.V., Qi, M. Review Models and Methods for Determining and Predicting the Reliability of Technical Systems and Transport. Mathematics, 2023. 11(15). Article no. 3317. DOI: 10.3390/math11153317
- Kondratiev, V.V., Karlina, A.I., Guseva, E.A., Konstantinova, M.V., Gorovoy, V.O. Structure of Enriched Ultradisperse Wastes of Silicon Production and Concretes Modified by them. IOP Conference Series: Materials Science and Engineering. 2018. 463(4). Article no. 042064. DOI:10.1088/1757-899X/463/4/042064
- Dudin, M.O., Vatin, N.I., Barabanshchikov, Y.G. Modeling a set of concrete strength in the program ELCUT at warming of monolithic structures by wire. Magazine of Civil Engineering. 2015. 54(2). Pp. 33–45. DOI: 10.5862/MCE.54.4
- Bosikov, I.I., Klyuev, R.V., Revazov, V.Ch., Martyushev, N.V. Analysis and evaluation of prospects for high-quality quartz resources in the North Caucasus. Mining Science and Technology (Russia). 2023. 8(4). pp. 278–289. DOI: 10.17073/2500-0632-2023-10-165
- 29. Cherkasova, T.G., Cherkasova, E.V., Tikhomirova, A.V., Gilyazidinova N.V., Gilyazidinova N.V., Klyuev R.V., Karlina, A.I., Skiba, V.Y. Study of Matrix and Rare Elements in Ash and Slag Waste of a Thermal Power Plant Concerning the Possibility of their Extraction. Metallurgist. 2022. 65(11–12). Pp. 1324–1330. DOI: 10.1007/s11015-022-01278-2
- 30. Rassokhin, A., Ponomarev, A., Shambina, S., Karlina, A. Different types of basalt fibers for disperse reinforcing of fine-grained concrete. Magazine of Civil Engineering. 2022. 109(1). Article no. 10913. DOI: 10.34910/MCE.109.13
- 31. Taha, M.M.R., Shrive, N.G. Enhancing Fracture Toughness of High-Performance Carbon Fiber Cement Composites. ACI Materials Journal. 2001. 98(2). Pp. 168–178.
- 32. Kondrat'ev, V.V., Ershov, V.A., Shakhrai, S.G., Ivanov, N.A., Karlina, A.I. Formation and Utilization of Nanostructures Based on Carbon During Primary Aluminum Production. Metallurgist. 2016. 60. Pp. 877–882. DOI: 10.1007/s11015-016-0380-x
- Yelemessov, K., Sabirova, L.B., Martyushev, N.V., Malozyomov, B.V., Bakhmagambetova, G.B., Atanova, O.V. Modeling and Model Verification of the Stress-Strain State of Reinforced Polymer Concrete. Materials. 2023. 16(9). 3494. DOI: 10.3390/ma16093494
- 34. Cusson, D., Pualtre, P. Stress-Strain Model for Confined High-Strength Concrete. Journal of Structural Engineering. 1995. 121(3). Pp. 468–477. DOI: 10.1061/(ASCE)0733-9445(1995)121:3(468)

Contacts:

Larisa Panchenko, PhD in Technical Sciences ORCID: https://orcid.org/0000-0003-1486-593X

E-mail: Panchenko.bstu@mail.ru

Tatyana Druzhinina,

ORCID: https://orcid.org/0009-0002-3003-9988

E-mail: <u>druzhininairnitu@mail.ru</u>

Received 03.06.2024. Approved after reviewing 13.11.2024. Accepted 22.11.2024.



Magazine of Civil Engineering

ISSN 2712-8172

journal homepage: http://engstroy.spbstu.ru/

Research article UDC 532.517

DOI: 10.34910/MCE.132.6



Loads on hydraulic engineering and berthing structures of the coastal zone of the Neva Bay

G.L. Kozinetc, V.L. Badenko 🕒 . D. Sharapov 🖾 🕒 . E.V. Shonina 🕒







Peter the Great St. Petersburg Polytechnic University, St. Petersburg, Russian Federation

Keywords: Neva Bay, hydraulic structures, ice loads, wave loads, wind loads, modeling, design, SP 38.13330.2018, climate impact

Abstract. The object of the research is the hydraulic structures in the Neva Bay, including ports, dams, and navigation facilities, which are subjected to natural loads such as ice, wave, wind, and water level fluctuations. The study focuses on analyzing the impact of these forces on the stability and safety of these structures. The research is of high relevance due to the increasing challenges posed by climate change, which alters hydrological and ice conditions, and the growing human activity in the region that places additional pressure on the bay's ecosystem and infrastructure. The analysis of natural loads is crucial for the design of resilient structures that can withstand extreme weather events and maintain safe operations in the Neva Bay. The goal of the research is to assess the natural loads on hydraulic structures in the Neva Bay, providing reliable calculation methods for their impact. The tasks include analyzing the ice regime, wave and wind loads, and utilizing modern modeling techniques to develop optimal design solutions for these facilities. The results demonstrate that ice and wave loads significantly affect the safety of hydraulic structures in the Neva Bay, and appropriate measures, such as protective piers and icebreaker assistance, can mitigate these impacts. The research provides valuable data for the design of durable and resilient infrastructure in the region, accounting for the specific natural conditions of the Neva Bay.

Funding: The study was supported by a grant from the Russian Science Foundation No. 23-19-20062 and the St. Petersburg Science Foundation, agreement No. 23-19-20062.

Citation: Kozinetc, G.L., Badenko, V.L., Sharapov, D., Shonina, E.V. Method of integrated consideration of factors for calculation of anchor system of pontoons. Magazine of Civil Engineering. 2024. 17(8). Article no. 13206. DOI: 10.34910/MCE.132.6

1. Introduction

The object of study is the hydraulic structures located within the Neva Bay. These include various infrastructure elements such as dams, culverts, shipping locks, berthing facilities, and other navigation and port structures. The research focuses on analyzing the natural loads these structures experience, particularly from waves, ice, wind, and water level fluctuations. Additionally, it examines the hydrological, climatic, and ice effects in the bay, evaluating their impact on the stability and safety of these engineering

The Neva Bay is the eastern part of the Gulf of Finland of the Baltic Sea, located near Saint Petersburg and the Leningrad Region, where the Neva River flows into the Gulf of Finland, and extends from the mouth of the Neva to the line connecting the cities of Sestroretsk and Lomonosov [1]. The Neva Bay is of great hydrographic, ecological and socio-economic importance for the region [2-4]. The Neva Bay is distinguished by its relatively shallow nature, with depths not exceeding an average of 6-8 meters, which is due to the presence of significant bottom sediments brought by the Neva River [5-6]. These sediments

© Kozinetc, G.L., Badenko, V.L., Sharapov, D., Shonina, E.V., 2024. Published by Peter the Great St. Petersburg Polytechnic University.

include sand, silt and organic matter, forming unique ecosystems of the coastal zone [7-8]. The hydrological regime of the Neva Bay is subject to significant fluctuations in water level caused by both river runoff and sea tides, as well as periodic surges of water during strong westerly winds, which can lead to flooding in Saint Petersburg [9-10]. From an ecological point of view, the Neva Bay is a significant natural zone, which includes a variety of biotopes and is a habitat for many species of aquatic flora and fauna [5, 11-13]. At the same time, the bay ecosystem experiences significant anthropogenic pressure as a result of human activity, including urbanization, industrial production and shipping [14-16]. This leads to pollution of water resources, eutrophication and changes in the natural processes of self-purification of the reservoir.

The Neva Bay is an important transport hub, where many hydraulic structures are concentrated, which ensure shipping, industrial production, passenger transportation and protection of the territory from unfavorable hydrological conditions. An important element of the protection of the Neva Bay and adjacent territories from floods was the construction of the Complex of protective structures of St. Petersburg from floods, which is dams, culverts and shipping locks. This complex not only protects the city, but also allows regulating the water exchange between the Neva Bay and the rest of the Gulf of Finland [17]. The Big Port of St. Petersburg is a large port of Russia in the waters of the Neva Bay, including several cargo terminals. Various cargo terminals are concentrated here. The sea passenger port of St. Petersburg ("Marine Facade") specializes in receiving passenger ships, including cruise liners and ferries [18-19]. The berthing facilities are equipped for the comfortable reception of large passenger ships and provide access for tourists to the city center. The Neva Bay is home to large shipbuilding companies, such as the Admiralty Shipyards, which have their own berthing facilities for launching ships, repairing them, and maintaining them. Along the coast, there are yacht clubs equipped with marinas for small vessels, making the water area attractive for sailing and walking. Dredging operations are regularly carried out to prevent coastal erosion and maintain the necessary depth for shipping.

Hydraulic structures and berthing facilities in the Neva Bay are subject to various natural loads, including hydrological, climatic, and ice effects [20].

In the Neva Bay, waves are formed under the influence of the wind blowing from the west from the Gulf of Finland. The average wave height in the bay is about 0.5–1.5 meters, but in severe storm conditions it can reach 2.5–3 meters. Wave loads affect berthing structures, especially during autumn and winter storms, causing erosion of the coastline and affecting the structural elements of hydraulic structures [21-22].

The Neva Bay is subject to a seasonal ice regime, when an ice cover forms in winter. Typically, the ice reaches a thickness of 30–50 cm, although it can be thicker in severe winters. Ice loads include ice pressure on hydraulic structures, dams, piers, and bridge supports [23-24].

Hydrostatic loads in the Neva Bay are associated with changes in the water level, which are caused by both the Neva river runoff and sea surges. The water level can rise by 2–3 meters in the case of strong westerly winds.

This research topic is highly relevant due to several critical factors that intersect ecological, engineering, and socio-economic concerns in the Neva Bay region. With the ongoing impacts of climate change, the frequency and intensity of extreme weather events, such as storms, surges, and ice cover variations, are expected to increase. Given the critical role of hydraulic structures—such as dams, locks, and piers—in protecting Saint Petersburg and the surrounding region from flooding and facilitating maritime transport, ensuring their safety and functionality is of paramount importance. The research directly addresses the risks posed by wave and ice loads, which can undermine the stability of these structures, potentially leading to catastrophic failures with significant economic and environmental consequences.

The goal of this research is to analyze the natural loads acting on hydraulic structures in the Neva Bay, with a focus on ice, wave, wind, and water level fluctuations, to ensure the safe design, operation, and durability of engineering facilities such as ports, dams, and navigation structures in the region. Some tasks of the research include:

Analyze the impact of natural loads on hydraulic structures in the Neva Bay, specifically addressing ice, wave, wind, and water level variations.

Develop calculation methods for determining the values of various impacts (ice, wave, wind, and water level changes) that affect the stability of structures in the Neva Bay.

Investigate the ice regime of the Neva Bay, including its formation, thickness, and effects on hydraulic structures, with a particular focus on ice hummocking and mid-winter ice conditions.

Calculate ice loads using the relevant formulas considering key factors such as ice movement speed, thickness, and compressive strength.

Assess wind loads in the Neva Bay region, especially the effects of prevailing west and westnorthwest winds on hydraulic structures.

Examine wave heights and wave loads in the Cabotage Harbor, and propose measures, such as protective piers, to mitigate wave impacts and ensure the safe operation of hydraulic structures.

Apply modern methodologies, including numerical modeling, to more accurately assess natural loads and optimize design solutions for hydraulic structures based on the specific conditions of the Neva Bay.

Methods and approaches to determining loads on hydraulic structures include both traditional engineering methods and modeling and monitoring technologies [25]. In recent years, there has been significant progress in the field of numerical modeling, the use of remote sensing data, and the application of intelligent systems for load assessment. The use of software packages for numerical modeling allows calculating wave loads and currents in a reservoir, taking into account the bottom topography, wind speed, and other factors [26]. Ice regime models take into account the formation and movement of ice, ice pressure on structures and possible collisions with icebergs. In Arctic conditions, it is possible to use models that take into account multi-year ice and its drift. Satellites and drones provide data on ice conditions, wave height, water level and other parameters. This data can be quickly processed to assess loads in real time. Analysis of natural loads on hydraulic structures is an important aspect of engineering design and operation aimed at ensuring the safety, durability and cost-effectiveness of these facilities. Without an accurate analysis of loads, there is a risk of structural failure, which can lead to emergency situations and environmental disasters. Load assessment allows you to design structures taking into account expected extreme conditions, reducing the likelihood of failure. One of the tasks of the analysis is to assess the intensity and frequency of various natural loads. For example, it is important to know the average and maximum wave height, ice thickness, the likelihood of extreme events (storms, water surges). In the current conditions of climate change, it is important to consider how natural loads may change in the future (for example, rising sea levels, more frequent storms or melting ice). This helps to adapt designs to changing conditions.

2. Methods

The ice cover of the Neva Bay is usually smooth [23, 27]. The upper layer of ice is cloudy white, opaque; it consists of frozen wet snow. The lower layers of ice are lead-gray and quite transparent. Sometimes at the beginning of winter, before the ice reaches a thickness of 15-20 cm, its movements and hummocking are observed. This occurs mainly during westerly winds, which are accompanied by a rise in water level. As the level rises, the ice cover breaks away from the banks, and through cracks appear in it. The wind completes the destruction. It happens that a solid ice cover turns into a bizarre mosaic of slabs of various shapes and sizes. Each slab lives its own life. At the junction of two slabs, either hummocks or leads are formed. Crawling onto the shore, the ice floes seem to plow it; and then low sand banks appear.

In mid-winter, the ice cover of the bay, the thickness of which is 30-60 cm, at an air temperature of 5 °C has the following strength characteristics: bending strength - 8.5 kg/cm², one-sided compression strength - 16.0 kg/cm² (1.6 MPa). The ice thicknesses are presented in the Table 1.

	Cha	aracteristics of winter	
Water body, area	Soft	Normal	Harsh
Coastal areas of the Neva Bay	30 — 40	50 — 70	80 — 100
Central regions of the Neva Bay	20 — 30	30 — 40	60 — 80

Table 1 - Maximum ice thickness (cm) during winter [23, 28].

According to the Ministry of Emergency Situations and Roshydromet [28], the thickness of the ice in the Kronstadt area usually does not exceed 60 cm. It is worth considering that the fairway along which the design object is located, as well as the port infrastructure, are regularly cleared using icebreakers, as shown in the figure 1.



Figure 1. Breaking ice using icebreakers.

The maximum load on the outer southern pier of the Coastal Harbour from fields of level ice on an extended structure is determined by formula (1) in accordance with Russian State Standard SP 38.13330.2018:

$$F_{c,w} = 2.2 \cdot 10^{-3} \cdot V \cdot h_d \cdot \sqrt{A \cdot k_v \cdot R_c \cdot \rho} \approx 4.2MN \tag{1}$$

where V — the speed of movement of the ice field, m/s, is taken as 0.6 m/s;

 h_d — the guaranteed thickness of level ice, m, is taken as 1 m;

A — the maximum area of an ice field (or the total area of several ice fields exerting pressure on each other), m^2 , is taken as 12000 m^2 ;

 k_v — coefficient, 0.5 is taken;

 ρ — water density;

 R_c — The one-way compression strength is taken as 1.6 MPa;

There are no loads on internal structures from flat ice fields. It is worth noting that the instructions for assessing ice loads according to SP 38.13330 differ for different versions of the documents. In the work [29] using the example of ice load on a pile foundation, it was shown that in some cases the load according to the new method becomes greater, while in others it is possible to reduce the load for the 2018 version.

The loads on structures from a continuous ice cover during its thermal expansion are determined by formula (2) in accordance with SP 38.13330.2018 per 1 meter of the structure:

$$q = h_d \cdot k_L \cdot p = 80 \, \frac{kN}{m} \tag{2}$$

where h_d — the guaranteed thickness of level ice, m, is taken as 1 m;

 k_L — coefficient of loss of stability of ice cover, 0.8 is taken;

p — pressure due to elastic and plastic deformation, kPa, 100 is taken.

The latest version of Russian State Standard SP 38.13330 (2018 version) introduced a large fork in the calculations of salt and fresh ice. Figure 2 shows a surface illustrating the behavior of the calculated force from ice action when varying the initial data. Some studies [27], indicate that the result of calculations with a salinity of more than 3‰ should be additionally checked. In the Gulf of Finland, the salinity of the

water is not high, which is due to the large influx of fresh water from the rivers, especially from the Neva (2/3 of the total flow). The salt water of the Baltic mixes with fresh water, but has a higher density and is located at depth, and fresh water spreads over the surface. Therefore, the further west and deeper the water sample is taken, the saltier it will be. Thus, the result according to SP 38.13330.2018 can be accepted as for relatively fresh ice near the mouth of the rivers.

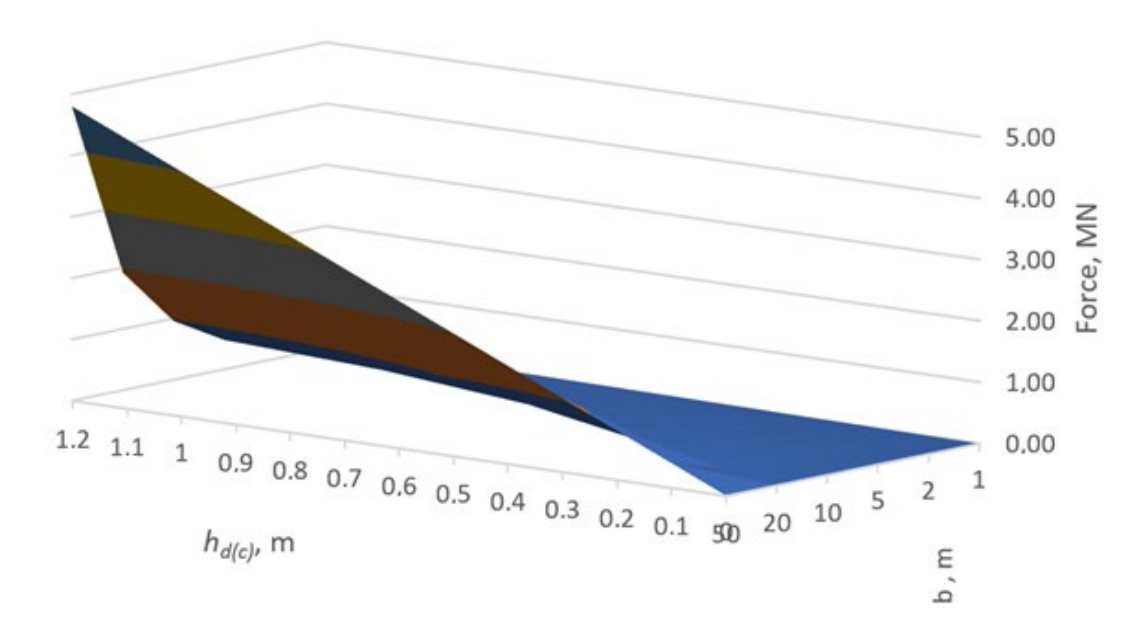


Figure 2. Behavior of the calculated ice force on a structure with varying width and thickness [20].

The vertical load (per 1 m of length along the front of the structure) from the ice cover frozen to the structure when the water level changes is determined by formula (3) in accordance with SP 38.13330.2018:

$$f_d = 2.24 \cdot 10^{-3} \cdot \rho \cdot g \cdot h_0 \cdot h_d \cdot \left(\frac{v^2}{g \cdot h_d^3}\right)^{1/12} = 20 \frac{kN}{m}$$
 (3)

where h_0 — change in UV, m, we take 0.5 m;

 h_d — the guaranteed thickness of level ice, m, is taken as 1 m;

v — kinematic viscosity of water at 0 °C, $v = 1,793 \cdot 10^{-6} m^2 / s$.

Ice load modeling using numerical methods is recommended in some works [20], to move to the next step of technological development, however, when implementing projects in the current legal field, significant efforts are required to justify the use of the results of a numerical calculation that is not standardized.

According to in-kind observations of meteorological stations located in the area of the navigation passage S1 KZ, the prevailing wind direction is W, WNW (240 - 290 degrees). The maximum wind speed is 29 m/s, the average value of the maximum wind gusts is 12.6 m/s.

For the worst mooring option, in the south direction or north direction, the load value is calculated using formula (4) in accordance with SP 38.13330.2018:

$$Q_w = 460kN \tag{4}$$

where A_n – lateral above-water projection, m², is taken as 100 for a yacht with dimensions of 20*5, 1000 for a yacht with dimensions 100*10

 V_n – transverse component of wind, m/s, we take 25 m/s

 ξ – the coefficient depending on the largest horizontal dimension is taken as 1.

For a vessel 100 m long, $Q_w = 460kN$, the longitudinal component is insignificant.

3. Results and Discussion

The analysis showed that: the estimated wave load height is 1.1 meters for a half-wave in the fairway area. The loads on structures from a solid ice cover with its thermal expansion are 80 kN/m. The loads on structures from an ice cover frozen to a structure with a change in water level are 20 kN/m. Wind loads for the worst-case location of a vessel with an above-water part length of 20 m, a height of 5 m and a wind speed of 25 m/s are 46 kN/m, for a vessel 100 m long and 10 m high – 460 kN/m. The maximum load on the outer southern pier of the Coastal harbor from flat ice fields is 4.2 MN. Verification dynamic calculations of wave loads and wave heights were carried out for two options. The calculations are shown in the figures 3, 4, 5, 6. The recommended maximum wave height according to clause 6.1.8 of Russian State Standard GOST R 58736—2019 is 0.3 meters. Figures 29 and 30 show 2 different scales: from -0.7 to +0.7 meters and, for clarity, a scale from -0.15 to 0.15 meters is shown.

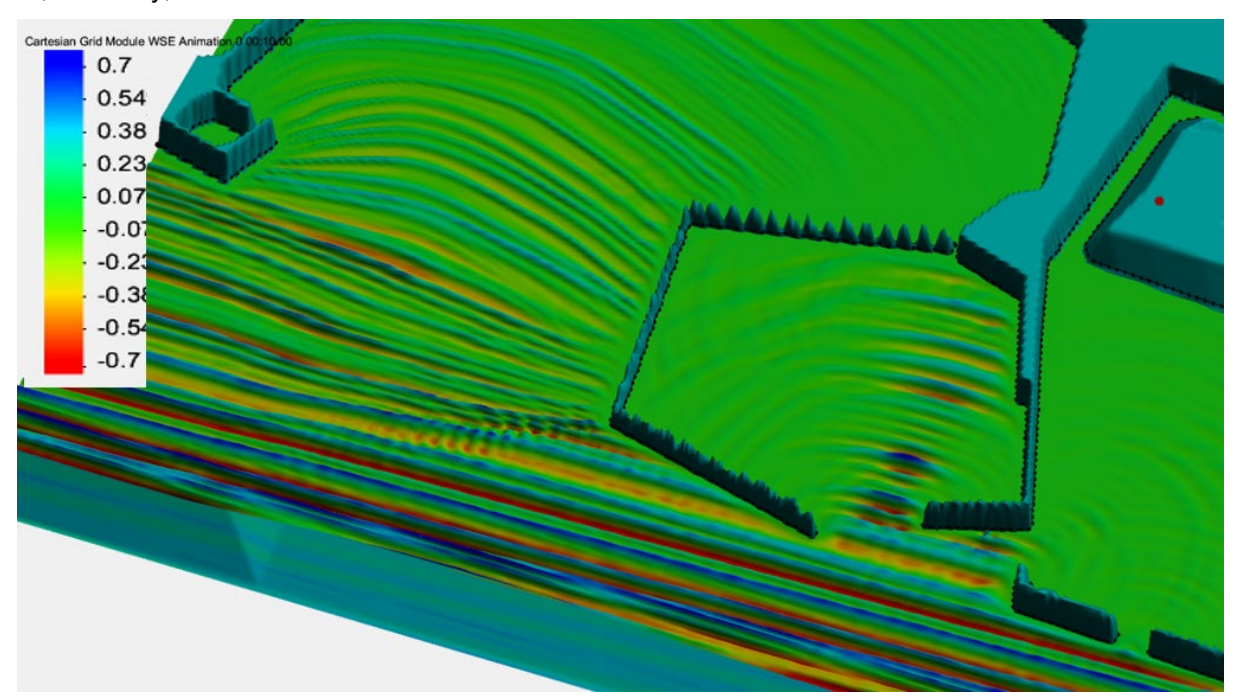
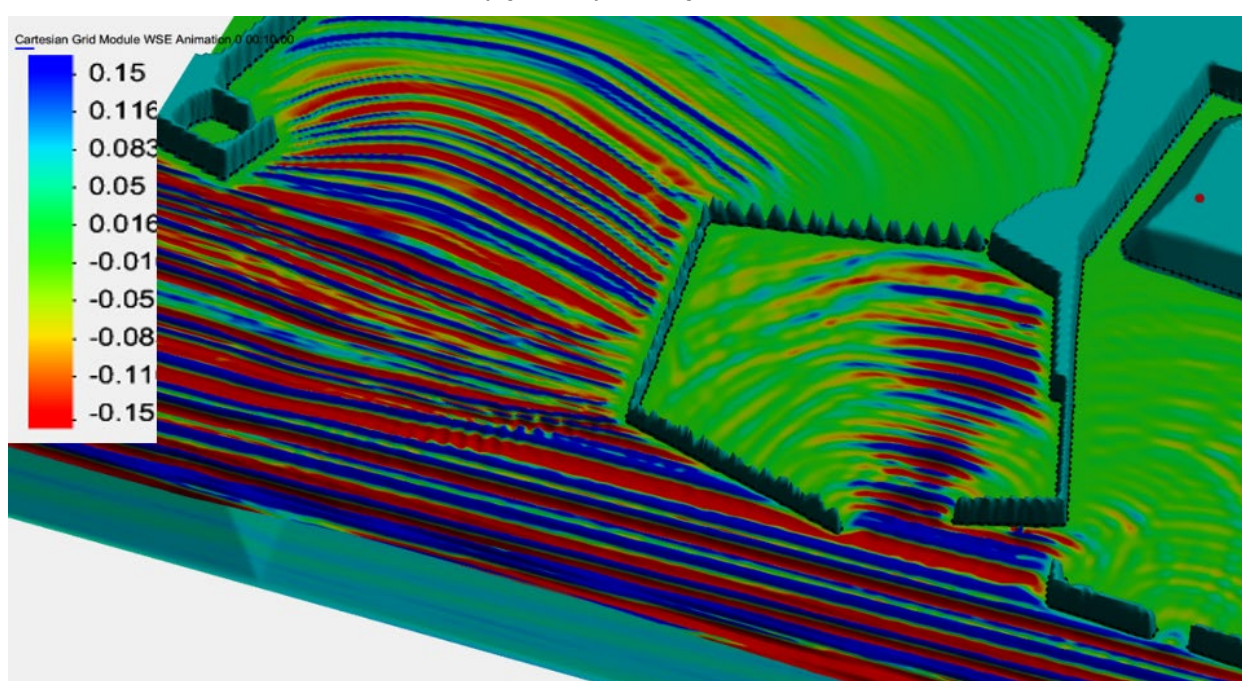


Figure 3. Result of wave height calculation in Kabotazhnaya and Kupecheskaya harbors (option 1), example 1.



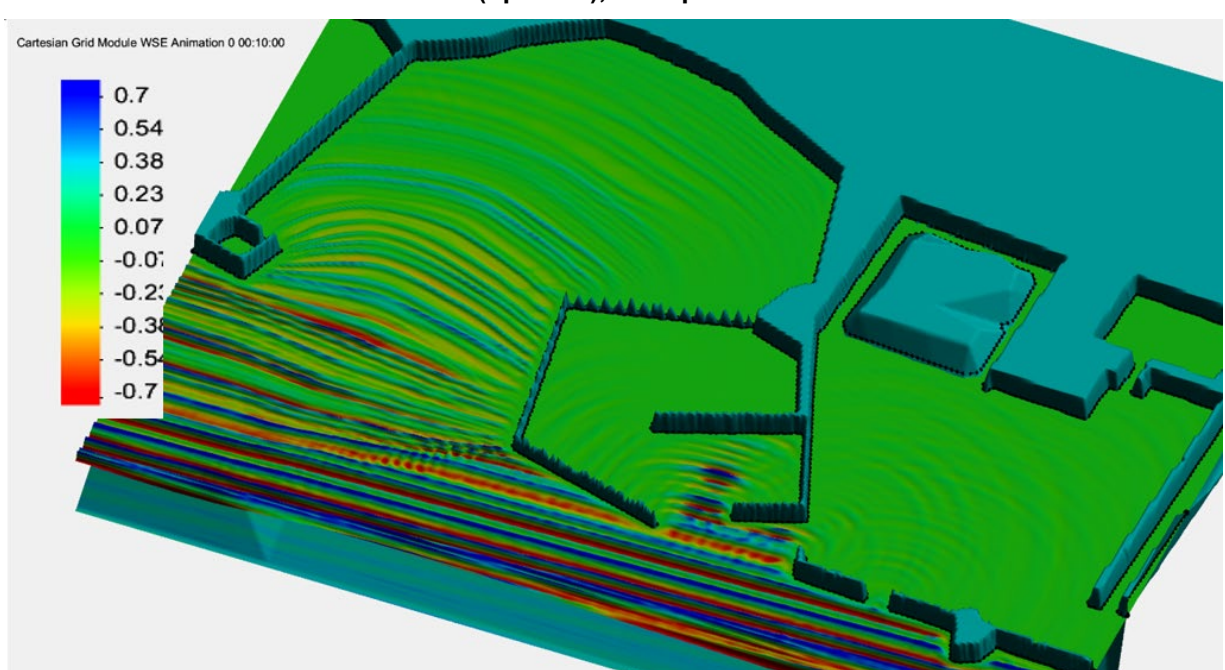


Figure 4. Result of wave height calculation in Kabotazhnaya and Kupecheskaya harbors (option 1), example 2.

Figure 5. Result of wave height calculation in Kabotazhnaya and Kupecheskaya Aharbors (option 2), example 3.

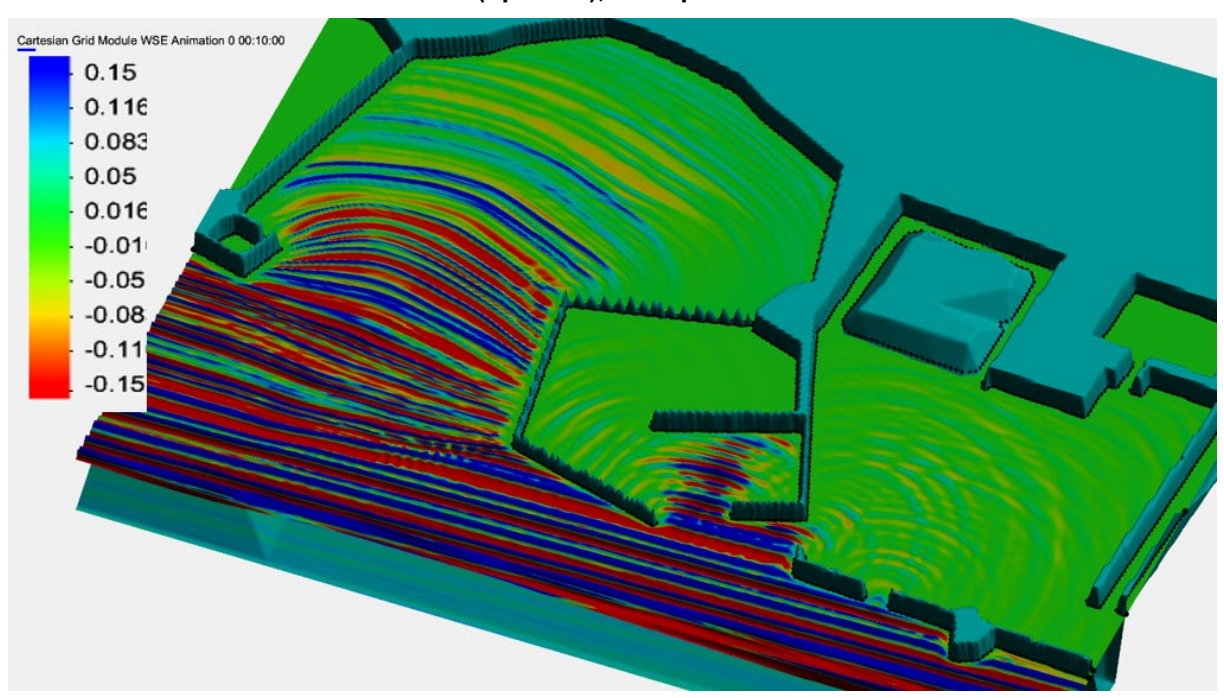


Figure 6. Result of wave height calculation in Kabotazhnaya and Kupecheskaya harbors (option 2), example 4.

Figures 7, 8 have wave height in meters (ETA) and the wave load in kN/m are determined for a design period of 600 seconds. Table 2 shows the maximum values of the wave height and the force of its impact at each design point.

Figures 7, 8 show graphs of wave height and loads at the design points. The maximum values of wave height and force at a given time at the design points are shown in Table 2 for two design cases.

Table 2. Maximum values of wave height and force at the calculated points at the moment of time.

No. of calculated point	Option	Maximum wave height. h (m)	Maximum force from wave. F (kN/m)	Time. s
	1	1.6	580	340
1	2	1.6	580	340
0	1	0.13	137	370
2	2	0.14	141	380
2	1	0.14	224	360
3	2	0.16	227	360
4	1	0.4	370	360
4	2	0.4	380	360
F	1	0.18	96	380
5	2	0.07	92	380
0	1	0.6	410	355
6	2	0.002	34.1	370
7	1	0.19	91	380
7	2	0.025	82	400
0	1	0.6	380	400
8	2	0.005	22.5	460

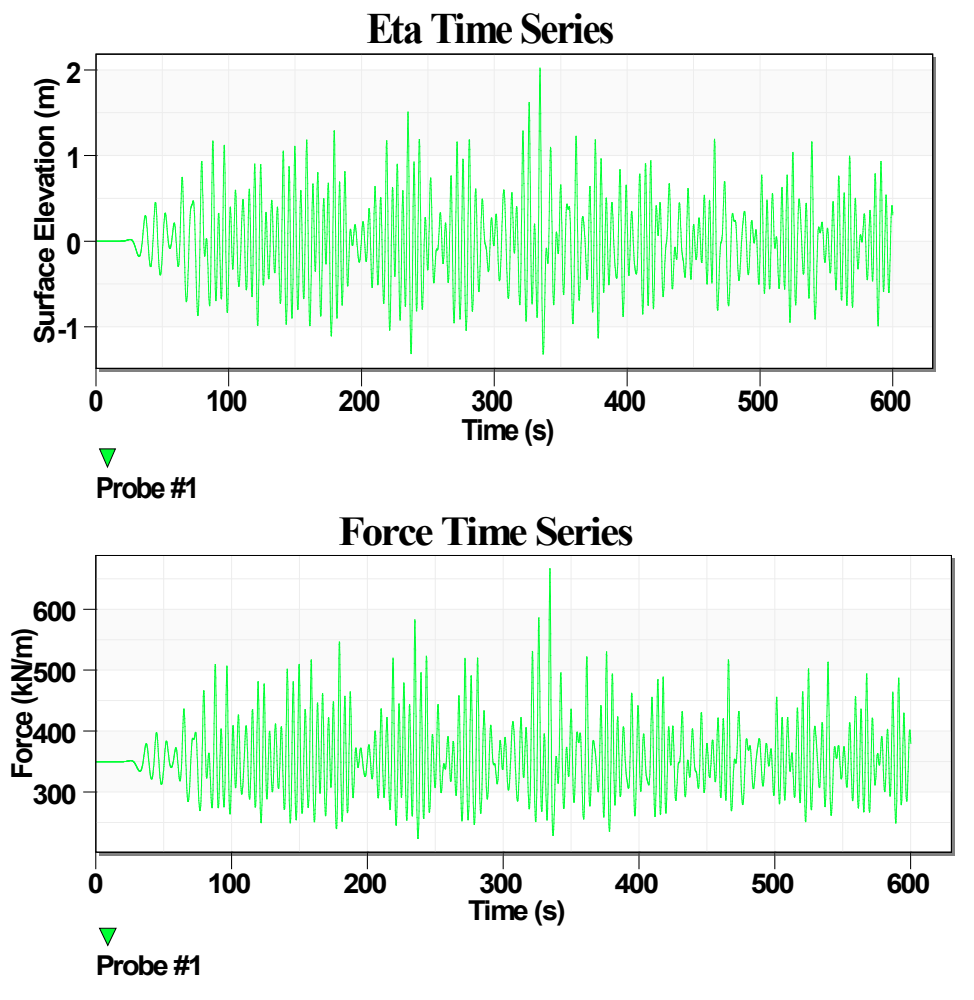


Figure 7. Design point 1, option 1, h (m) F (kN/m).

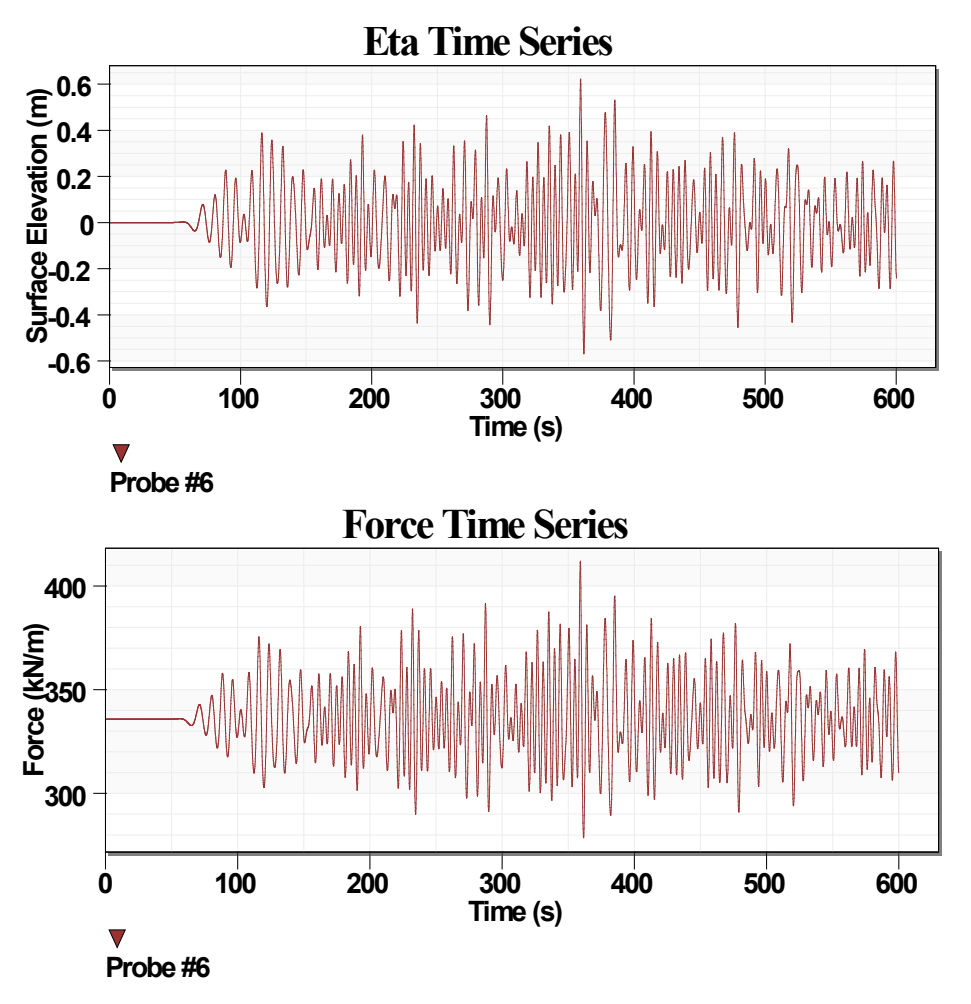


Figure 8. Design point 2, option 1, h (m) F (kN/m).

Based on the results of calculating the wave height at design points 1 and 2, in the first design option (without a protective pier with a 250 m long berth wall) the maximum wave height is observed at the entrance to the harbor (design point 1) is 1.6 meters. The wave height at design point 2 is 0.6 meters, which exceeds the maximum wave height recommended by the manufacturer for the selected pontoons, which is 0.5 meters, as well as the recommended wave height of 0.3 meters according to clause 6.1.8 of Russian State Standard GOST R 58736—2019. In this regard, the optimal design option is option No. 2, with a protective pier with a 250 m long berth wall.

the results а comparison with another works were The study by Ryabchuk [1] focuses on the anthropogenic and natural influences on Neva Bay, addressing the bay's role as a technogenic lagoon. Similar to the conclusions of the current research, it highlights the significance of hydrodynamic factors, such as ice and wave conditions, which impact the hydraulic structures. The research acknowledges the importance of natural forces like ice and wave activity, aligning with the emphasis on these factors in the current study. Kozinets and colleagues [2] focus on anthropogenic impacts, particularly on the bottom morphology of the Neva Bay. While the current study is more concerned with the design and calculation of loads on hydraulic structures, it also touches on similar aspects related to the environmental changes in the bay, such as the influence of water level fluctuations and ice conditions. Both studies stress the need for tailored engineering solutions based on the bay's dynamic conditions. Prishchepenko [5] discuss the long-term impacts of human activity on the region's ecosystem and geological environment. The current research shares an understanding of how natural forces, such as wind and ice, interact with human-made structures, influencing their design and longevity. Both studies reflect the importance of regional factors like ice cover and wind direction in shaping engineering solutions. Sharapov [20] made an emphasis on the development and application of calculation methods for ice loads, including parameters such as ice thickness, movement speed, and compressive strength. The current study aligns with the approaches outlined by Sharapov particularly in using SP 38.13330.2018 for ice load estimations. Väli [26] suggest that accurate hydrodynamic models are necessary for understanding and mitigating the risks posed by changing water conditions, which are crucial for designing resilient infrastructure. Golubkov [11] study the ecological impacts of environmental changes in the Neva Estuary, while the current research focuses more on engineering solutions for hydraulic structures. Both works

acknowledge the importance of monitoring regional environmental conditions, such as water turbidity and primary production, which can influence structural stability indirectly by affecting water properties.

The research findings align closely with the conclusions in the references, particularly with respect to the significance of ice, wave, and wind loads in the design and operation of hydraulic structures in the Neva Bay. The reviewed studies corroborate the need for specialized calculations, regional modeling, and tailored engineering solutions to address the unique challenges posed by these environmental forces.

4. Conclusion

- 1. The analysis of loads on hydraulic structures in the Neva Bay is crucial for the design and operation of engineering facilities, such as ports, dams, and navigation structures.
- 2. Special attention must be given to ice and wave loads, as well as the influence of wind and changes in water levels, since these factors significantly impact the stability of structures. The study addressed various types of impacts typical for the Neva Bay's conditions and provided calculation methods for determining the values of these impacts.
- 3. The ice regime in the Neva Bay is characterized by a relatively smooth ice cover, largely due to the low salinity of water caused by the influx of freshwater from the Neva River. Ice hummocking, which can occur at the beginning of winter, is linked to ice movement caused by westerly winds and rising water levels. In mid-winter, the ice thickness ranges from 30-60 cm. According to the Ministry of Emergency Situations and Roshydromet, the ice thickness in the Kronstadt area does not exceed 60 cm, confirming regional characteristics of the ice regime.
- 4. Calculations of ice loads show they can be determined using the formula from SP 38.13330.2018, considering factors such as ice movement speed, thickness, and compressive strength. Structures within protective facilities are not subject to significant ice loads, as icebreaker assistance enables the timely removal of ice from shipping routes and port waters.
- 5. Wind loads also significantly impact structures in the Neva Bay, with the prevailing wind direction being west and west-northwest.
- 6. The analysis of wave heights and wave loads in the Cabotage Harbor suggests the need for measures to reduce wave activity to ensure safe operation of hydraulic structures. Protective piers could help mitigate wave impact.
- 7. Load analysis and calculations aid in selecting optimal design solutions that ensure the safety and durability of hydraulic structures. The application of modern methods, such as numerical modeling, allows for a more precise assessment of loads and the design of hydraulic structures tailored to regional conditions. As a result of the study, the loads on structures in the Neva Bay were calculated.

References

- Ryabchuk, D., Zhamoida, V., Orlova, M., Sergeev, A., Bublichenko, J., Bublichenko, A., Sukhacheva, L. Neva Bay: A
 Technogenic Lagoon of the Eastern Gulf of Finland (Baltic Sea). The Diversity of Russian Estuaries and Lagoons Exposed to
 Human Influence. Estuaries of the World. Springer, Cham, 2017. DOI: 10.1007/978-3-319-43392-9
- Kozinets, G.L., Badenko, V.L., Zotov, D.K. Anthropogenic Impact on the Changes in the Neva Bay Bottom Morphology in the 19th–21st Centuries. Power Technology and Engineering. 2024. 58(2). 209–217. DOI: 10.1007/s10749-024-01799-7
- Dolukhanov, P.M., Subetto, D.A., Arslanov, K.A., Davydova, N.N., Zaitseva, G.I., Djinoridze, E.N., Kuznetsov, D.D., Ludikova, A.V., Sapelko, T.V., Savelieva, L.A. The Baltic Sea and Ladoga Lake transgressions and early human migrations in Northwestern Russia. Quaternary International. 2009. 203(1-2). 33–51. DOI: 10.1016/j.quaint.2008.04.021
- 4. Andrén, T., Björck, S., Andrén, E., Conley, D., Zillén, L., & Anjar, J. The development of the Baltic Sea Basin during the last 130 ka. The Baltic Sea Basin. 2011. 75–97. DOI 10.1007/978-3-642-17220-5 4
- Prishchepenko, D.V., Ryabchuk, D.V., Zhamoida, V.A., Sergeev, A.Y., Leontev, F.A., Grigoriev, A.G., Neevin, I.A., Budanov, L.M., Kovaleva, O.A. Main trends and results of 300-years anthropogenic impact on the geological environment and ecosystem of the Eastern Gulf of Finland. Continental Shelf Research. 2023. 265. 105058. DOI: 10.1016/j.csr.2023.105058
- Ludikova, A.V., Subetto, D.A., Kuznetsov, D.D., Orlov, A.V., Shatalova, A.E. New diatom and sedimentary data confirm the existence of the northern paleo-outlet from Lake Ladoga to the Baltic Sea. Quaternary. 2024. 7(3), 31. DOI: 10.3390/quat7030031
- Chusov, A., Shilin, M., Gogoberidze, G., Bobylev, N., Ershova, A., Lednova, J. Long-term monitoring of the dredged material deposit sites in the Eastern Gulf of Finland. E3S Web of Conferences. 2020. 164. 01010. EDP Sciences. DOI: 10.1051/e3sconf/202016401010
- 8. Martyanov, S., Ryabchenko, V. Bottom sediment resuspension in the easternmost Gulf of Finland in the Baltic Sea: A case study based on three–dimensional modeling. Continental Shelf Research. 2016. 117. 126–137. DOI: 10.1016/j.csr.2016.02.011
- 9. Lopez, J.L.A., Kalyuzhnaya, A.V., Kosukhin, S.S., Ivanov, S.V. Data quality control for St. Petersburg flood warning system. Procedia Computer Science. 2016. 80. 2128–2140. DOI: 10.1016/j.procs.2016.05.532
- 10. Popov, S.K., Lobov, A.L. Hydrodynamic modeling of floods in Saint Petersburg considering the operating dam. Russian Meteorology and Hydrology. 2017. 42. 267–274. DOI: 10.3103/S1068373917040070
- 11. Golubkov, S., Golubkov, M., Tiunov, A., Nikulina, V. Long-term changes in primary production and mineralization of organic matter in the Neva Estuary (Baltic Sea). Journal of Marine Systems. 2017. 171. 73–80. DOI: 10.1016/j.jmarsys.2016.12.009

- Golubkov, M., Golubkov, S. Photosynthetically active radiation, attenuation coefficient, depth of the euphotic zone, and water turbidity in the Neva estuary: relationship with environmental factors. Estuaries and Coasts. 2023. 46(3). 630–644. DOI: 10.1007/s12237-022-01164-9
- 13. Demchuk, A.S., Uspenskiy, A.A., Golubkov, S.M. Abundance and feeding of fish in the coastal zone of the Neva Estuary, eastern Gulf of Finland. Boreal Environment Research. 2021. 26(1-6). 1.
- 14. Kholodkevich, S.V., Kuznetsova, T.V., Sharov, A.N., Kurakin, A.S., Lips, U., Kolesova, N., Lehtonen, K.K. Applicability of a bioelectronic cardiac monitoring system for the detection of biological effects of pollution in bioindicator species in the Gulf of Finland. Journal of Marine Systems. 2017. 171. 151–158. DOI: 10.1016/j.jmarsys.2016.12.005
- 15. Golubkov, M., Nikulina, V., Golubkov, S. Species-level associations of phytoplankton with environmental variability in the Neva Estuary (Baltic Sea). Oceanologia. 2021. 63(1). 149–162. DOI: 10.1016/j.oceano.2020.11.002
- 16. Filippov, A.A., Kokorin, A.I., Genelt-Yanovskaya, A.S., Polyakova, N.V., Starkov, A.I., Nikishina, D.V., Gerasimova, A.V. The state of benthic and planktonic invasive species in adjacent to St. Petersburg waters of the Gulf of Finland in 2018 as against the data for 2014. Ecosystem Transformation. 2024. 7(1). 120–146. DOI: 10.23859/estr-220928
- Vasilevsky, A.G., Klimovich, V.I., Tikhonova, T.S., Shipilov, A.V. Contribution of the VNIIG IM. BE Vedeneeva to the Design, Construction, and Operation of the St. Petersburg Flood Protection Barrier. Power Technology and Engineering. 2022. 55(5). 696–701. DOI: 10.1007/s10749-022-01418-3
- 18. Nazarenko, K.B., Smirnova, M.A. St. Petersburg port through disasters: challenges and resilience. Journal of Urban History. 2021. 47(2). 272–292. DOI: 10.1177/0096144219877864
- 19. Lavrov, L., Molotkova E. Marine Facade, western High-Speed Diameter and Vasilyevsky Island as a part of the Saint Petersburg historical center. Architecture and Engineering. 2019. 4(2). 40–52. DOI: 10.23968/2500-0055-2019-4-2-40-52
- Sharapov D., Brief on development of ice load estimation for hydrotechnical engineering. Proceedings of 23rd International Multidisciplinary Scientific GeoConference SGEM 2023. 2023. 23(2.1). DOI: 10.5593/sgem2023/2.1/s08.18
- 21. Kurennoy, D., Ryabchuk, D. Wind wave conditions in Neva Bay. Journal of Coastal Research. 2011. 1438–1442.
- Sokolov, A., Chubarenko, B. Case-Study Modelling Analysis of Hydrodynamics in the Nearshore of the Baltic Sea Forced by Extreme Along-shore Wind in the Case of a Cross-shore Obstacle. Archives of Hydro-Engineering and Environmental Mechanics.2018. 65(3). 163–176. DOI: 10.1515/heem-2018-0011
- 23. Ryabchenko, V., Dvornikov, A., Haapala, J., Myrberg, K. Modelling ice conditions in the easternmost Gulf of Finland in the Baltic Sea. Continental Shelf Research. 2010. 30(13). 1458–1471. DOI: 10.1016/j.csr.2010.05.006
- Vainio, J., Kalliosaari, S., Schmelzer, N., Grafström, T., Dailidiene, I., Komissarov, E., Soloshchuk, P. The ice season 2005– 2006. HELCOM Baltic Sea Environment Fact Sheets. [Online]. http://www.helcom.fi/baltic-seatrends/environment-fact-sheets/.
- 25. Andreev, P.N., Dvornikov, A.Y., Ryabchenko, V.A., Tsepelev, V.Y., Smirnov, K.G. Simulation of storm surges in the Neva Bay on the basis of a three-dimensional model of circulation in the conditions of maneuvering by gates of the flood protection barrier. Fundamental and Applied Hydrophysics. 2013. 6(4). 23. 31.
- 26. Väli, G., Zhurbas, V., Lips, U., Laanemets, J. Submesoscale structures related to upwelling events in the Gulf of Finland, Baltic Sea (numerical experiments). Journal of Marine Systems. 2017. 171. 31–42.
- 27. Sharapov, D.A., Andreeva, S.A. Features of the Calculation of Ice Load Due to Thermal Expansion. Power Technology and Engineering. 2024. 57(5). 697–704. DOI 10.1007/s10749-024-01721-1
- 28. A report on climate features on the territory of the Russian Federation in 2022, Roshydromet, Moscow, 2023. 104 p.
- 29. Andreeva, S.A., Sharapov, D.A., Kudryashova, E.E. et al. Analysis of a new normative approach to calculating ice loads applied on pile rows. Power Technology and Engineering. 2024. 58. 195–200. DOI: 10.1007/s10749-024-01796-w

Information about the authors:

Galina Kozinetc. Doctor of Technical Sciences

E-mail: kozinets gl@spbstu.ru

Vladimir Badenko, Doctor of Technical Sciences ORCID: https://orcid.org/0000-0002-3054-1786

E-mail: vbadenko@gmail.com

Dmitry Sharapov, PhD

ORCID: https://orcid.org/0000-0001-8650-2375

E-mail: sharapov.dm@gmail.com

Ekaterina Shonina.

ORCID: <u>https://orcid.org/0000-0001-5292-7295</u>

E-mail: shonina ev@spbstu.ru

Received 31.08.2024. Approved after reviewing 06.12.2024. Accepted 16.12.2024.



Magazine of Civil Engineering

ISSN 2712-8172

journal homepage: http://engstroy.spbstu.ru/

Research article **UDC 624**

DOI: 10.34910/MCE.132.7



Stability of gypseous soils slopes stabilized with cutback asphalt and lime using the finite element method

Z. Abd Hacheem¹, S. Al-Khyat², K.A. Saeed², S.H.L. Fartosy² D



Mustansiriyah University, Baghdad, Iraq

☑ dr.sabah77@uomustansiriyah.edu.iq

Keywords: factor of safety, slope stability, binders, bituminous soil stabilization, ADONIS.

Abstract. Gypseous soils are widely distributed all over the world, particularly in Iraq. These soils exhibit unpredictable behaviour including losing strength and collapsing upon wetting. Treatment of gypseous soil is necessary to improve its geotechnical properties and assess its potential applications in engineering practices. Compacted gypseous soil samples stabilized with different binders, including cutback asphalt and lime. Slope stability analysis was performed to determine the factor of safety and analyze the behaviour of the stabilized gypseous soil. ADONIS 3.25, a computer program based on the finite element method, was used to characterize the gypseous soil and to analyze the slope stability by Mohr-Coulomb failure criteria and visco-plastic algorithm. The effects of varying the percentages of binders and the slope angle (H:V) were investigated. A total of thirty numerical analyses were performed. Results of the numerical analysis indicated that the best slope stability was obtained when the gypseous soils stabilized with 4 %cutback asphalt and 3 % lime at a slope angle of 3H:1V. It was also observed that the slope angle has a considerable effect on the safety factor of the slope, such that, the steepest the slope angle - the lowest the safety factor.

Acknowledgment: The authors would like to appreciate the great support they received from Mustansiriyah-University (https://www.uomustansiriyah.edu.iq), Baghdad- Iraq which was helpful to achieve this research.

Citation: Abd Hacheem, Z., Al-Khyat, S., Saeed, K.A., Fartosy, S.H.L. Stability of gypseous soils slopes stabilized with cutback asphalt and lime using the finite element method. Magazine of Civil Engineering. 2024. 17(8). Article no. 13207. DOI: 10.34910/MCE.132.7

1. Introduction

Slope stability analysis is required in geotechnical projects, such as cuts, fills, dams, and road embankments, since it concerns the safety of human life and property. As a result, appropriate slope inspections, remedies, and engineering solutions must be provided to prevent potentially devastating collapse [1]. A slope failure is the failure of a mass of soil in a downward and outward movement of a slope. The surface along which the slide occurs has different shapes and represents the surface of minimum resistance. A variety of methods and techniques have been used for the analysis of earth slopes, including the finite element method (FEM) based on cohesion (c) and internal friction angle (Φ) reduction, the finite difference method (FDM), the limit analysis (LA), and a combination of the FEM and the FDM [2]. Slope geometry, soil type, soil shear strength, soil stratification, groundwater condition, and seepage significantly impact slope failure and should be considered during slope stability analysis [3].

Slope stabilization can be accomplished using a variety of approaches including structural and geometric methods [4]. For example, reducing the slope height (H) results in a higher factor of safety (FS) of the slope. Many other studies have employed soil improvement and stabilization to investigate the

© Abd Hacheem, Z., Al-Khyat, S., Saeed, K.A., Fartosy, S.H.L., 2024. Published by Peter the Great St. Petersburg Polytechnic University

behaviour of reinforced slope stability soils made of various materials [5–8]. Soil stabilization alters the engineering properties of soils, such as gypseous soils, in such a way that it gains long-term strength and stability. Gypseous soils are soils that contain gypsum and are susceptible to losing strength when introduced to wetting. Gypseous soils with varied proportions of gypsum contents cover a large portion of Iraq. The estimated coverage area of gypseous soils was reported to be about 12.2 % by Barazanji [9] as shown in Fig. 1. The amount of gypsum in the upper north and centre parts of the Euphrates and Tigris beds can reach 80 %, whereas the gypsum content of the Al-Jazirah area ranges from 3 % to 10 % in the upper parts to 50 % in the lower parts [10].

Several stabilizers can be used to improve the characteristics of gypseous soils by limiting the effect of water, such as cutback asphalt and lime. Bituminous soil stabilization is one of the oldest methods for improving soil properties. Cutback asphalt dissolves in certain solvents, such as gasoline, to improve its fluidity and workability. Cutback asphalt is classified into rapid, medium and slow curing cutback depending on the solvent used [11]. When the solvent evaporates, the bitumen remains to bond the particles together. The asphalt acts as a waterproofing agent and enriches the cohesive strength and durability characteristics of gypseous soils. Asphalt coating the soil particles provides a membrane that prevents or limits water infiltration, which would otherwise result in a loss of soil strength. In the waterproofing of bituminous materials, two hypotheses can be explained. The theory of the plug at which the bituminous globules operate as plugs or stoppers in the soil void spaces or soil capillaries, removing or eliminating the flow pathways via which surface water might enter or exit the mix [12]. The membrane theory is the second theory that assumes a thin bituminous film will operate as a covering or segregator for individual soil particles, resulting in the same consequence of waterproofing the soil as the plug theory, however in a slightly different way. Cutback asphalt also acts as a cementing agent, such that the soil particles also adhere to the asphalt allowing it to act as a binder or cementing agent. The cementing effect thus increases shear strength by increasing cohesion [13]. According to the intimate mix theory, the efficiency of a bituminous material's cementing activity is primarily explained by the adhesion that occurs between the binder and soil particles. The action of surface tension, adsorption, and other features of the solid and liquid surfaces interact to produce this adhesion. Since water has a higher wetting power than any bituminous binder, full cementation and total adhesion can only be achieved when the binder displaces any water on the surface and when too much binder is applied and the film covering around the particles becomes too thick. Because the bituminous cohesiveness is reduced, contact between the particles is prevented, and strength is reduced. Lime soil stabilization, on the other hand, has been often used. The lime is added in the form of calcium oxide or calcium hydroxide to the soil at the optimum moisture content [14].

Generally, all fine-grained soils treated with lime show lower plasticity, enhanced workability, and reduced volume change characteristics. Not all soils, however, have better strength properties. The characteristics of a soil-lime mixture are influenced by several factors, the most important of which are soil type, lime type, lime percentage, and curing conditions [15]. When lime is added to fine-grained soil, it causes a series of reactions. Cation exchange is taken place in which the positively altered ions cling to the surface of clay particles. The common cation replacement happens in the form of lyotropic series (Na+ K+ Mg++ Ca++). It is clear from this series that if multivalent cations are accessible in the soil, monovalent cations will be replaced by them [16]. As a result of the modifying effects of electrolytes on the extension of the electrical double layer from the surfaces of clay particles, clays flocculate when electrolytes are added. The electrolyte reduces the electrostatic repulsive interactions between clay particles by repressing the double layer. This causes a net pull between negatively charged faces and positively charged edges of neighboring clay particles, especially between negatively charged faces and positively charged edges of nearby clay particles [17]. The other series of reactions can occur in the form of pozzolanic reactions. The pozzolanic reactions are lime reactions with soil silica and/or alumina that result in the development of a stiff water-insoluble gel that cements the soil particles [18]. When lime reacts with the silica and/or alumina, it forms calcium silicate hydrated and/or calcium aluminate hydrated in the form of a soluble gel that coats and cements soil particles as it hardens. Pozzolanic reactions are lime-dependent, and strength improved slowly and steadily over time [17]. A potentially negative impact reaction on the stabilizing process could be lime reacts with carbon dioxide in the air to generate calcium carbonate, a rather weak cementing agent (CaCO3) [15].

Stabilization of gypseous soil with asphalt and lime has been recognized as an economical treatment in Iraq due to the abundance of limestone from which lime is manufactured and the availability of cutback asphalt as refineries wastes [19]. These stabilizers have been successfully used to improve the engineering properties of gypseous soils. Studies on examining the potential application of stabilized gypseous soils in engineering practice, such as earth slopes are scarce. Therefore, this study aims to evaluate the slope stability of gypseous soils stabilized with different percentages of cutback asphalt and lime using the FEM.

2. Materials and Methods

Experimental results of a study conducted by Al-Safarani [19] was used in this study. Al-Safarani [19] used a gypsum-rich soil that obtained from Abu Ghraib, 30 km from Baghdad with 48.6 % gypsum content. The sample was collected at a depth of 0.5–1.0 m below the natural ground level [19]. Table 1 lists the physical and chemical characteristics of the soil used [19]. Soil stabilization was achieved using the hydrated lime (Ca(OH)₂) generated when quick lime reacts chemically with water. Table 2 shows the chemical composition of the lime used [19]. A medium cutback asphalt [MC-30] produced by the Dora refinery in Baghdad was used. The properties of asphalt used are given in Table 3 [19].

Two groups of stabilized samples were prepared. The first group were stabilized with 0 %, 2 %, 4 %, 6 %, 8 %, and 10 % cutback asphalt (MC). While, lime (L) of 3 %, 5 %, 7 %, and 9 % were added to the soil samples with the best percentage of cutback asphalt to stabilize the second group. It was found that the best percentage of cut back asphalt was 4 % as it shows better soil behavior in terms of compression, permeability, collapse, and compaction. The stabilized samples were air-cured for seven days and then soaked for about one hour. A series of direct shear tests were conducted on the prepared samples and the results are summarized in Table 4 [19]. The dry unit weight for each condition was obtained from the compaction tests.

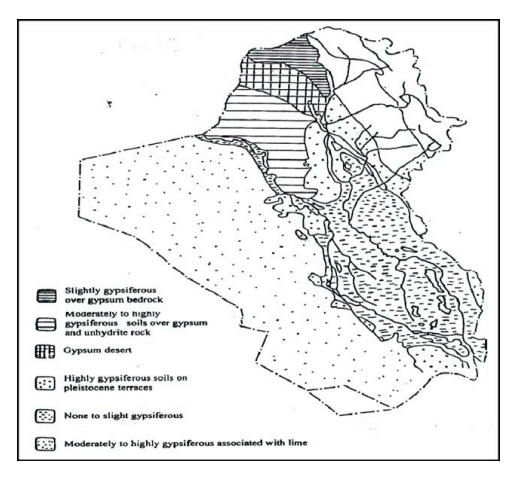


Figure 1. Gypseous soil in Iraq (after, Barazanji [9]).

Table 1. Geotechnical properties of the soil [19].

Soil property	Standard	Result
Gypsum content (%)		48.6
Liquid limit (%)	BS1377: 1975, test No.2, A	31.0
Plastic limit (%)	BS 1377:1975, test No.3	NP
Specific gravity of soil solids	BS 1377:1975, test No.6 B	2.39
Maximum dry unit weight (kN/m³)	ASTM D698-78	16.0
Optimum moisture content (%)		14.7
Sand (%)	ASTM D422-72	90.5
Fines (%)	ASTM D422-72	9.5
Soil classification	USCS	SP-SM
Sulphate content (SO ₃) (%)	BS 1377:1975, test No.5	22.21
Total soluble salt (T.S.S) (%)	BS 1377:1975, test No.8	63.7
Chloride content (CL) (%)	BS 1377:1975, test No.7	0.09
Organic matters (%)	BS 1377:1975, test No.3	0.2
рН	BS 1377:1975, test No.9	8.1

Table 2. Chemical analysis of Lime [19].

Composition	Percentage by weight
CaO	72.33
MgO	6.83
SiO ₂	10.25
Al_2O_3	1.68
Fe ₂ O ₃	8.13

Table 3. Properties of the cutback asphalt after Dora Refinery lab. Baghdad [19].

Property	MC-30	
Kinematics viscosity at 60°C (c.Stoke)	75–150	
Specific gravity of soil solids	0.99	
Distillate, %vol. of the total, Distillate to 360°C		
To 225°C	25 max.	
To 260°C	40-70	
To 315°C	75–93	
Residue from distillation to 360°C%vol. by difference	50 min.	
Test on residue from the distillation	120–300	
Penetration at 25°C (100g, 5 sec.)	120–300 100 min.	
Ductility at 25°C	99.5 min.	
Solubility in CCl4, %wt. min.		

Table 4. The effect of binder on shear strength parameters [19].

Percentage of binder	c (kPa)	Ø (degree)	γd (kN/m³)
0 % MC	10.0	46.3	16.00
2 % MC	28.0	39.8	15.25
4 %MC	39.5	42.0	14.90
6 % MC	43.5	37.6	14.75
8 % MC	38.5	37.0	14.60
10 % MC	37.0	36.2	14.20
4 % MC + 3 % L	51.5	44.5	14.90
4 % MC + 5 % L	53.0	40.2	14.85
4 % MC + 7 % L	36.1	39.8	14.70
4 % MC + 9 % L	35.0	28.6	14.70

2.1. Failure Criteria

Several failure criteria for characterizing the strength of soil as an engineering material have been developed. The best-known criterion for soils with both frictional and cohesive components of shear strength is Mohr–Coulomb, which has the shape of an irregular hexagonal cone in primary stress space. Cylindrical failure criteria are acceptable for metals or undrained clays that behave in a frictionless manner ($\phi u \approx 0$, ϕu is the angle of internal friction in undrained condition). These are the most basic conditions, and they are not affected by the initial invariant S or σ_m . Since the Tresca criterion is a particular case of the Mohr–Coulomb criterion, it does not require independent mathematical treatment [20]. According to the Mohr–Coulomb criterion, the shear strength increases with increasing normal stress on the failure plan [21].

$$\tau = C + \sigma \tan \varphi, \tag{1}$$

where τ is the shear stress on the failure plane, C is the cohesion of the material, σ is the normal effective stress on the failure surface, and ϕ is the angle of internal friction. This failure criterion is shown graphically in Fig. 2. The concept of the Mohr circle can be used to express the criterion in terms of principal stresses.

According to Fig. 2,

$$\frac{\sigma_1 - \sigma_3}{2} = AB + BF. \tag{2a}$$

That is

$$\frac{\sigma_1 - \sigma_3}{2} = OA \sin \varnothing + C \cos \varnothing. \tag{2b}$$

Hence:

$$\frac{\sigma_1 - \sigma_3}{2} = \frac{\sigma_1 + \sigma_3}{2} \sin \varnothing + C \cos \varnothing. \tag{2c}$$

Here, σ_1 & σ_3 are the major and minor principal stresses, respectively. In the stress space, Equation (2c) describes an uneven hexagonal pyramid. The projection of this surface on the π -plane is shown in Fig. 2. The three stress invariants are σ_m , t and θ . In which σ_m describes the mean stress, t describes the shear stress, and θ gives the direction of the shear stress. The relationship between principal stresses and invariants is given as follows.

$$\sigma_1 = \sigma_m + 2/3\,\overline{\sigma}\sin\left(\theta - \frac{2\pi}{3}\right);$$
 (3a)

$$\sigma_2 = \sigma_m + 2/3\,\overline{\sigma}\sin(\theta);\tag{3b}$$

$$\sigma_3 = \sigma_m + 2/3\,\overline{\sigma}\sin\left(\theta + \frac{2\pi}{3}\right),$$
 (3c)

where:

$$\sigma_m = S/\sqrt{3}, \ \overline{\sigma} = t\sqrt{\frac{2}{3}}, \ S = \frac{1}{\sqrt{3}}(\sigma_x + \sigma_y + \sigma_z);$$
 (4)

$$t = \frac{1}{\sqrt{3}} \left[\left(\sigma_x - \sigma_y \right)^2 + \left(\sigma_y - \sigma_z \right)^2 + \left(\sigma_z - \sigma_x \right)^2 + 6\tau_{xy}^2 + 6\tau_{yz}^2 + 6\tau_{zx}^2 \right]^{1/2}; \tag{5}$$

$$\theta = \frac{1}{3}\arcsin\left(\frac{-3\sqrt{6}J_3}{t^3}\right),\tag{6}$$

where:

$$J_3 = S_x S_y S_z - S_x \tau_{yz}^2 - S_y \tau_{xz}^2 - S_z \tau_{xy}^2 + 2\tau_{xy} \tau_{yz} \tau_{zx}. \tag{7}$$

And

$$S_x = \frac{\left(2\sigma_x - \sigma_y - \sigma_z\right)}{3},\tag{8}$$

etc.

The substation of σ_1 and σ_3 from equations (3a and 3c) in equation (2c) provides the function

$$F = \sigma_m \sin \varnothing + \overline{\sigma} \left(\frac{\cos \theta}{\sqrt{3}} - \frac{\sin \theta \sin \varnothing}{3} \right) - C \cos \varnothing. \tag{9}$$

Which is dependent upon all three invariants $(\sigma_m, \overline{\sigma}, \theta)$. The Tresca criterion is obtained from equation (3) by using $(\emptyset = 0)$.

$$F = \frac{\overline{\sigma}\cos\theta}{\sqrt{3}} - C_u. \tag{10}$$

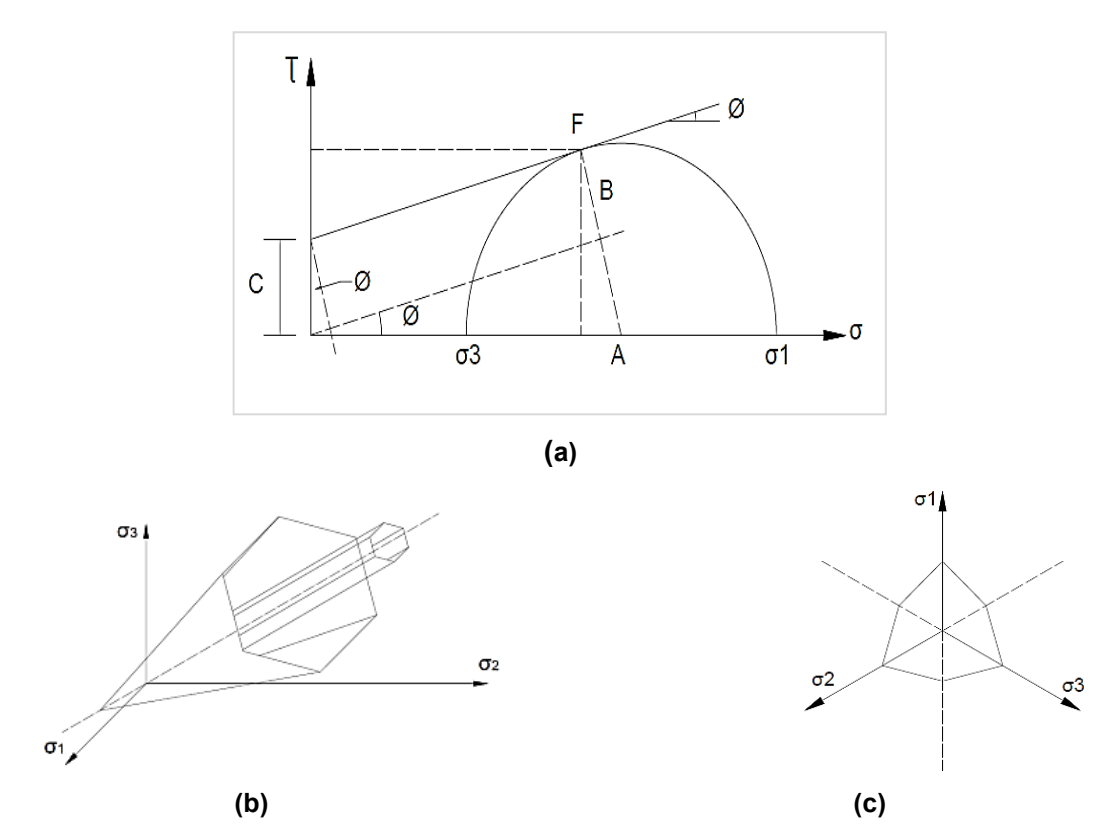


Figure 2. Mohr–Coulomb criteria on (a) σ – τ -plane, (b) stress space and (c) π plane.

2.2. Finite Element Method

The FEM is often used to obtain a realistic evaluation of stresses and deformations within earth structures as an approximate solution for gypseous soil. The results of finite element analysis can also be effectively used to evaluate the overall degree of safety and stability of these structures. The proper modelling of materials behavior and the efficient simulation of different loading conditions confirm to a high extent the reliability of the finite element results. The mathematical formulation related to the theoretical aspects of the finite element techniques is presented by Reddy [22].

The solution technique utilized in the present analysis is based on the modified Newton–Raphson method where the elastic solutions are repeated for a constant stiffness matrix. To achieve the required convergence, the load vector (the right-hand side) is to be changed iteratively. The following equations are used for each load increment:

$$K\delta^i = P^i. (11)$$

Must be solved for displacements δ^i where i represents the iteration number. The element displacement increments u_i are extracted from the nodal displacement vector oi and these lead to total strain increment according to the strain-displacement relationships:

$$\Delta \varepsilon^i = B u^i, \tag{12}$$

where B is the B-matrix of an element. If the material is yielding, the strains will comprise both elastic and plastic or visco-plastic components, as given in Equation (13):

$$\Delta \varepsilon^{i} = \left(\Delta \varepsilon^{e} + \Delta \varepsilon^{P}\right)^{i}. \tag{13}$$

Only the elastic strain increments $\Delta \varepsilon^e$ cause stresses to be generated by the elastic stress-strain matrix $\left(D^e\right)$; thus:

$$\Delta \sigma^i = D^e \left(\Delta \varepsilon^e \right)^i. \tag{14}$$

These stress increments are added to the stresses already existing from the previous load step and updated stresses are substituted into the failure criterion. If stress redistribution is required, the load increment vector P_i in equation is changed (15). This load vector, in general, holds two sorts of loads as shown by:

$$P_i = P_a + P_b^i, (15)$$

where P_a denotes the actual applied load increase, and P_b^i denotes the body load vector, which fluctuates from iteration to iteration. The P_b^i vector must be self-equilibrating in order for the system's net load to be unaffected.

The visco-plasticity algorithm established by Zienkiewicz [23] is used to generate the body-loads vector. The material is allowed to endure stresses that are outside the failure criterion for finite elements in this manner (periods). Overshoot of the failure criterion, denoted by a positive value of (f), is a crucial component of the approach and is utilized to create the algorithm. The plastic strains generated by this algorithm are referred to as visco-plastic strains because their rate is proportional to the amount by which yield has been violated by the expression:

$$\xi^{VP} = F \frac{\partial Q}{\partial \sigma},\tag{16}$$

where the potential function (Q) is used instead of the yield function to account for the non-associative flow rule.

For dimensional considerations, a pseudo-viscosity property equal to unity is implied on the right-hand side of Equation (16). The increase of visco-plastic strain is accumulated from one "time step" or iteration to the next by multiplying the visco-plastic strain rate by a pseudo-time step:

$$\left(\delta \varepsilon^{VP}\right)^i = \Delta t \left(\xi^{VP}\right)^i; \tag{17}$$

$$\left(\Delta \varepsilon^{VP}\right)^{i} = \left(\Delta \varepsilon^{VP}\right)^{i-1} + \left(\delta \varepsilon^{VP}\right)^{j}.$$
 (18)

Since the time step for unconditional numerical stability is dependent on the stated failure criterion, the Mohr–Coulomb criterion:

$$\Delta t = \frac{4(1+\nu)(1-2\nu)}{E(1-2\nu+\sin^2\varphi)},\tag{19}$$

where v is Poisson's ratio and E is the modulus of elasticity. The derivatives of the potential function (Q) concerning stresses are conveniently expressed through the chain rule; thus:

$$\frac{\partial Q}{\partial \sigma} = \frac{\partial Q}{\partial \sigma_m} \frac{\partial \sigma_m}{\partial \sigma} + \frac{\partial Q}{\partial J_2} \frac{\partial J_2}{\partial \sigma} + \frac{\partial Q}{\partial J_3} \frac{\partial J_3}{\partial \sigma}.$$
 (20)

Summing the following integrals for all elements having a yielding Gauss point, the body loads P_b^l are accumulated at each time step inside each load phase:

$$P_b^i = P_b^{i-1} + \sum_{element}^{all} \int B^T D^e \left(\delta \varepsilon^{VP} \right)^i d(element). \tag{21}$$

At each time step or iteration, this process is repeated until no Gauss point stresses violate the failure condition within a given tolerance. The convergence criterion is based on a dimensionless measure of the change in the displacement increment vector I from iteration to iteration. Description of the entire algorithm are given in [20].

2.3. Factor of Safety Calcualtion

ADONIS is a free geotechnical nonlinear finite element software (http://geowizard.org) that employed the visco-plastic algorithm presented by Smith and Griffiths [20]. The problem to be investigated is a Mohr–Coulomb slope subjected to gravity loading. The FS of the slope must be determined, and this factor is defined as the proportion by which tan (\varnothing) and C must be reduced to induce failure. This differs from the author's software, which caused failure by raising loads while keeping the material attributes constant.

From integrals of the type, the gravity loading vector P_a for material with unit weight (γ) is accumulated for each element.

$$P_{a} = \gamma \sum_{element}^{all} \int N^{T} d\left(element\right). \tag{22}$$

These computations are made in the same program that creates the global stiffness matrix. It is worth noting that the integrals only include the freedoms that correspond to vertical movement. The 1-d array ELD is used at the element level to collect the contributions from each Gauss point. After multiplying by the unit weight GAMA (γ) , the global gravity loads vector GRA VLO gathers ELD from each element.

In this software, the gravity loads vector is applied to the slope in a single increment, and the "load increment loop" is now known as the "trial factor of safety loop". Each step in this loop corresponds to a distinct soil strength parameter's FS. The elastoplastic analysis requires calculated soil strength parameters, which are obtained.

$$\emptyset_f = \arctan(\tan \emptyset/FOS);$$
 (23)

$$C_f = \frac{C}{FOS}. (24)$$

Several (typically increasing) values of the FS are tried until the algorithm fails to converge while keeping the load constant. The value to induce failure is the actual factor of slope safety.

2.4. Slope Stability Analysis

Three slope angle geometries were considered for the analysis (1H:1V), (2H,1V), and (3H:1V) as shown in Figs. 3a, b and c, respectively. Fig. 3 also illustrates the typical generated finite element mesh with the boundary condition of the slope problem. The parametric studies were the slope angle and binder contents in the gypseous soil.

3. Results and Discussion

Table 5 presents the safety factors calculated for the three slopes of gypseous soils stabilized with various percentages of cutback asphalt and lime binders. Results of the slope stability assessment indicated that the gentlest slope of (3H:1V) produced a higher FS compared to the other steeper ones. Such slope geometry impact on the slope stability was also reported by Shiferaw [1] and Taher et al. [24]. By decreasing the slope angles from 1:1 to 3:1, the safety factor increased by a range of 76 % to 84 % for all treated gypseous soils and by about 107 % for the untreated gypseous soil. The optimum percentage of cutback asphalt that produced the highest FS was found to be 6 %. This observation differs from the experimental results, in which 4 % was the optimum content of cutback asphalt. The reason could be related to the fact that the numerical analysis takes into consideration various stress distributions for each point along the failure surface, such as triaxial compression, direct simple shear, and triaxial extension, whereas the experiment results were only based on the direct shear tests [25] as explained in Fig. 4.

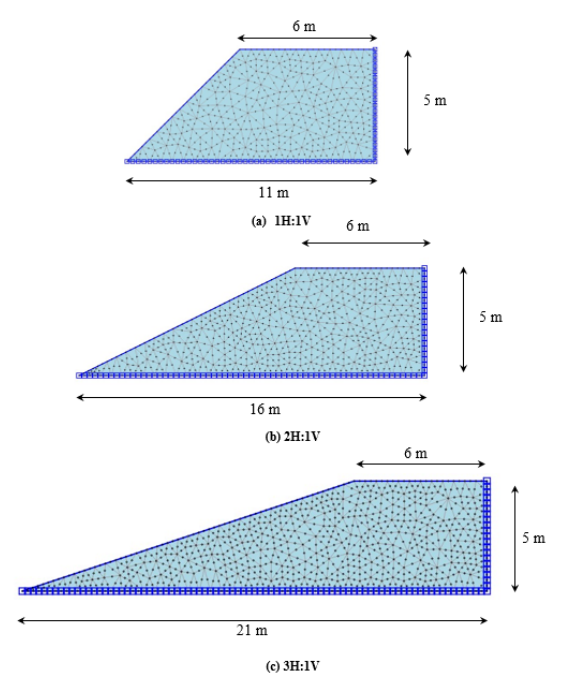


Figure 3. Typical generated mesh for prototype slopes geometry at (a) 1H:1V, (b) 2H:1V and (c) 3H:1V.

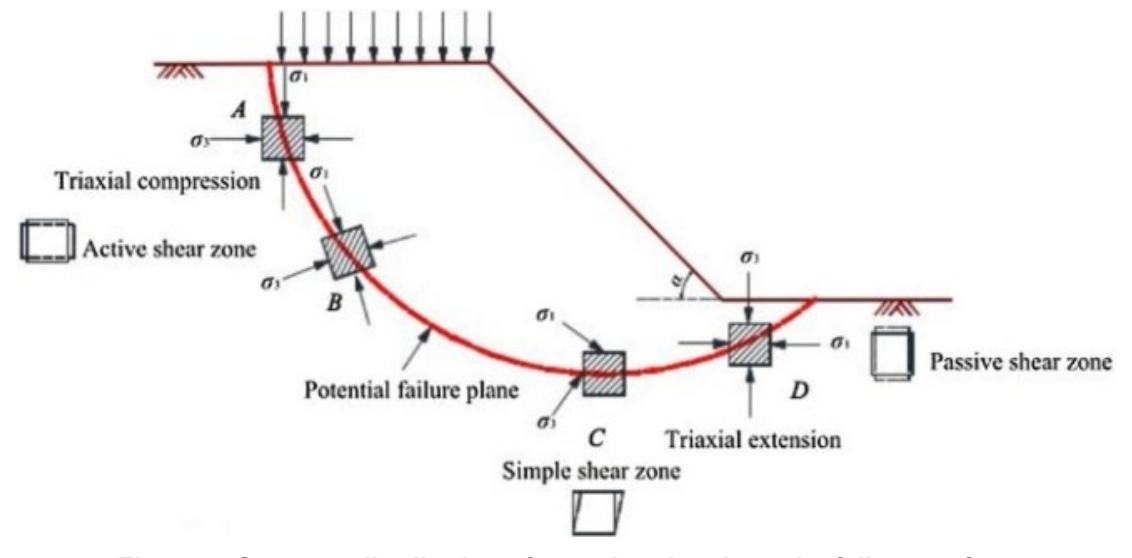


Figure 4. Stresses distributions for each point along the failure surface (after Nitzsche and Herle) [25].

The results presented in Table 5 also revealed that the stability of the slope was further improved when gypseous soils stabilized with mixed binders of 4 % MC and up to 5 % L. While no improvements were obtained with further addition of lime. Thus, it can be concluded that the greatest increase in the degree of stability was observed on slopes of gypseous soil with 4 % MC and 3 % L added binders. The reason could be mainly related to the increase in the soil strength (see Table 4), which resulted in increasing the FS.

Figs. 5a, b and c show the percentage increase in the FS versus the percentage of binders in the gypseous soil for slope angles 1:1, 2:1 and 3:1, respectively. The increasing percentage in the FS was calculated based on the following Equation:

$$FS(increasing\ percentage\ \%) = \frac{FS_{treated\ soil} - FS_{untreated\ soil}}{FS_{untreated\ soil}} \times 100. \tag{25}$$

It can be noticed from the results that the best increase in the FS of about 155 % was produced by the steepest slope followed by 130 % for the slope of 2H:1V and 120 % for the gentlest slope.

Table 5. Factors of the safety of the three slope angles with different percentages of binders.

Diadamana atau	FS		
Binder percentage	1 H:1 V	2 H:1 V	3 H:1 V
0 % MC	2.467	3.838	5.110
2 % MC	3.904	5.580	7.182
4 % MC	5.092	7.221	9.225
6 % MC	5.264	7.373	9.373
8 % MC	4.826	6.787	8.650
10 % MC	4.752	6.678	8.510
4 % MC + 3 % L	6.275	8.873	11.279
4 % MC + 5 % L	6.193	8.686	11.029
4 % MC + 7 % L	4.873	6.721	8.592
4 % MC + 9 % L	4.135	5.783	7.314

Fig. 6 presents the contours of the total displacement of the slope (3H:1V) at three selected percentages of the binder. It can be observed that as the binder content increased, the deformation decreased. The results of the failure mechanism slope also indicated that the majority of the failure surface was circular, which can be classified as face slope failure. This is because the soil employed in this study was gypseous soil, which is prone to collapse at the slope's face.

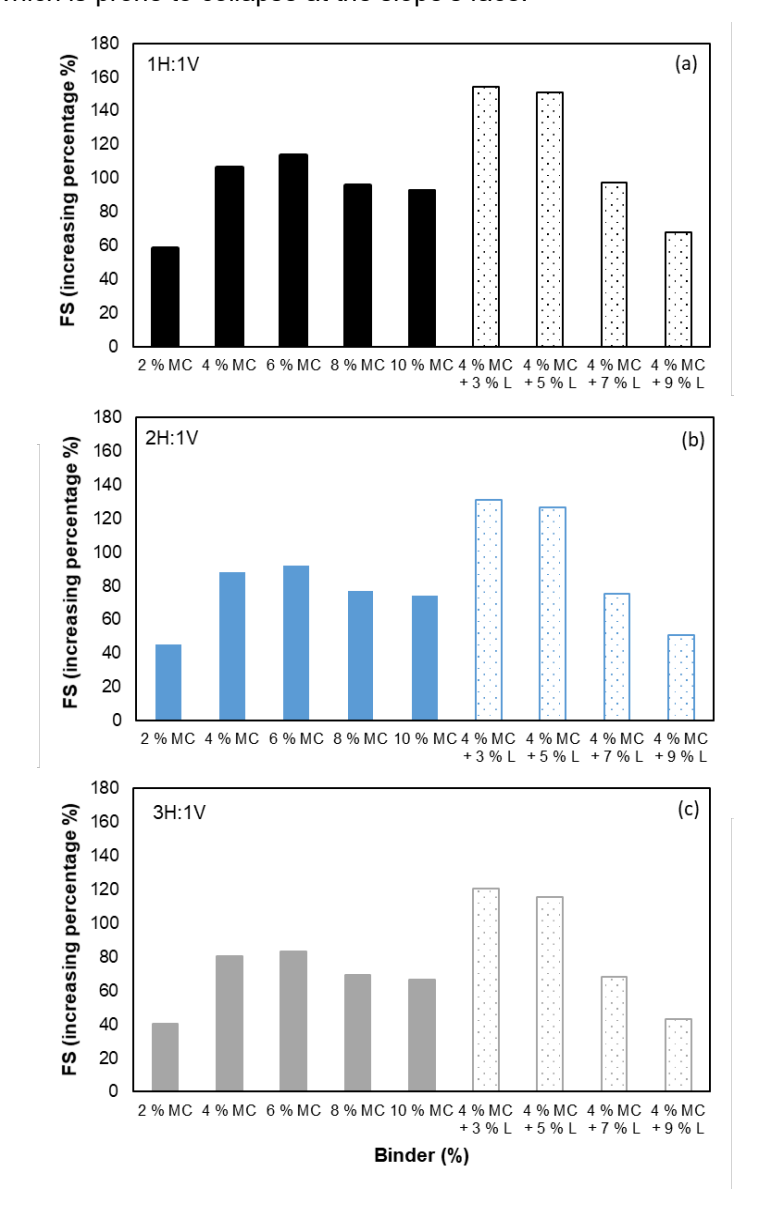


Figure 5. Percentage of increase in the FS with different content of binders of the three slopes at (a) 1H:1V, (b) 2H:1V and (c) 3H:1V.

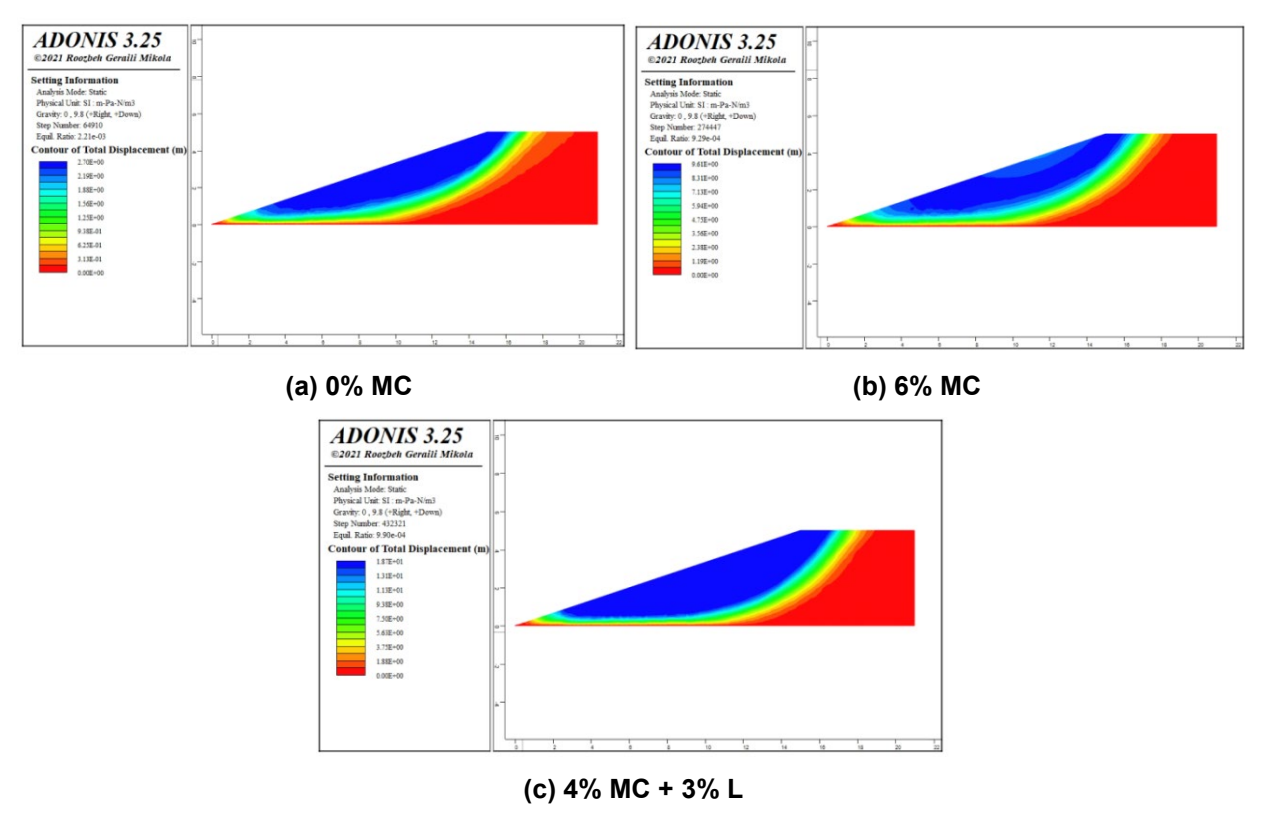


Figure 6. Contours of total displacement of 3H:1V slope at (a) 0% MC, (b) 6% MC and (c) 4% MC + 3% L.

4. Conclusions

The stability of slopes of gypseous soil stabilized with different percentages of cutback asphalt and lime was assessed using ADONIS computer program based on the FEM. The influence of slope angle (H:V) and binder percentages were considered in the analysis. The main findings from the numerical analysis can be summarized as follows: [1]

- 1. The angle of the slope has a substantial impact on slope stability. Such that, when the slope angle was changed from the steepest (1H:1V) to the gentlest (3H:1V), the safety factor increased dramatically. A similar finding was also reported by Shiferaw, and Taher et al. [23].
- 2. Based on the calculated FS, it can be suggested that stabilization of gypseous soil with cutback asphalt and lime offers a possible implication of the improved soil in engineering practice.
- Results of the stability analysis revealed a disagreement with the experimental results concerning
 the optimum content of the cutback asphalt stabilizer. The numerical results showed that when
 stabilizing the gypseous soil with cutback asphalt alone, the 6 % MC provides the highest safety
 factor.
- 4. The greatest stability of slopes was attained when gypseous soils were stabilized using 4 % MC and 3 % L at a slope angle of 3H:1V.
- Comparison between unstabilized and stabilized gypseous soil indicated that the steepest slope of 1H:1V provided the greatest increase in the safety factor.

References

- Shiferaw, H.M. Study on the influence of slope height and angle on the factor of safety and shape of failure of slopes based on strength reduction method of analysis. Beni-Suef University Journal of Basic and Applied Sciences. 2021. 10(1). Article no. 31. DOI: 10.1186/s43088-021-00115-w
- 2. Gör, M., Taher, N., Aksoy, H., Ahmed, H. Effect of Geogrid Inclusion on the Slope Stability. Proceedings of 5th International European Conference on Interdisciplinary Scientific Research. Valencia, 2022. Pp. 275–286.
- Halder, A., Nandi, S., Bandyopadhyay, K. A Comparative Study on Slope Stability Analysis by Different Approaches. Lecture Notes in Civil Engineering. 85. Geotechnical Characterization and Modelling. Spinger. Singapore, 2020. Pp. 285–293. DOI: 10.1007/978-981-15-6086-6_23
- Broms, B., Wong, I. Stabilization of slopes with geofabric. Proceedings of Third International Geotechnical Seminar on Soil Improvement Methods. Singapore, 1985. Pp. 75–83.

- 5. Abd Hacheen, Z. Finite Element Method for Evaluation of Gypseous Soil Treated with Emulsified Asphalt for Sloped Embankment. Engineering and Development Journal. 2008. 12. Pp. 111–128.
- Anvari, S.M., Shooshpasha, I., Kutanaei, S.S. Effect of granulated rubber on shear strength of fine-grained sand. Journal of Rock Mechanics and Geotechnical Engineering. 2017. 9(5). Pp. 936–944. DOI: 10.1016/j.jrmge.2017.03.008
- 7. Li, W., Kwok, C.Y., Senetakis, K. Effects of inclusion of granulated rubber tires on the mechanical behaviour of a compressive sand. Canadian Geotechnical Journal. 2020. 57(5). Pp. 763–769. DOI: 10.1139/cgj-2019-0112
- 8. Aksoy, H.S., Taher, N., Awlla, H. Shear strength parameters of sand-tire chips mixtures. Gümüşhane Üniversitesi Fen Bilimleri Dergisi. 2021. 11 (3). Pp. 713–720. DOI: 10.17714/gumusfenbil.865490
- 9. Barzanji, A.F. Gypsiferous soils of Iraq. PhD Thesis. Civil Engineering Department. Ghent University, 1973.
- 10. Barazanji, K.K.H. Infiltration rate characteristics of gypsiferous soils in Northern Iraq (Jazirah-Area). MSc Thesis. Department of Irrigation and Drainge Engineering. University of Mosul, 1984.
- 11. Woods, K.B. Highway Engineering Handbook. 1st edn. McGraw-Hill Education. NY, 1960. 1665 p.
- 12. Rogers, M., Enright, B. Highway engineering. 3rd edn. Wiley-Blackwell, 2016. 432 pp.
- 13. Guyer, J.P. Introduction to Soil Stabilization in Pavements. Continuing Education and Development, Inc. Woodcliff Lake, NJ, 2011. 29 p.
- Consoli, N.C., Lopes, L.d.S., Prietto, P.D.M., Festugato, L., Cruz, R.C. Variables Controlling Stiffness and Strength of Lime-Stabilized Soils. Journal of Geotechnical and Geoenvironmental Engineering. 2011. 137(6). Pp. 628–632. DOI: 10.1061/(ASCE)GT.1943-5606.0000470
- Haerry, F.A. Lime-Treated Soil Construction Manual: Lime Stabilization and Lime Modification. National Lime Association. 2004. 326(5). Pp. 67–92.
- Thompson, M.R. Lime Reactivity of Illinois Soils. Journal of the Soil Mechanics and Foundations Division. 1966. 92(5). Pp. 67–92.
- 17. Diamond, S., Kinter, E.B. Mechanisms of Soil-Lime Stabilization. Highway Research Record. 1965. 92. Pp. 83–102.
- 18. Archibong, G., Sunday, E., Akudike, J., Okeke, O., Amadi, C. A review of the principles and methods of soil stabilization. International Journal of Advanced Academic Research. Sciences, Technology and Engineering. 2020. 6(3). Pp. 2488–9849.
- 19. Al-Safarani, M. Improvement Ability of Gypseous Soil Characteristics Using Cutback Aasphalt and Lime. MSc Thesis. Civil Engineering Department. Mustansiriyah University, 2007.
- 20. Smith, I.M., Griffiths, D.V., Margetts, L. Programming the Finite Element Method. 5th edn. John Wiley & Sons. NY, 2013. 688 p.
- 21. Yu, H.-S. Plasticity and Geotechnics: Advances in Mechanics and Mathematics. 1st edn. Springer Science & Business Media, 2007. 522 p.
- 22. Reddy, J.N. An Introduction to the Finite Element Method. 3rd ed. McGraw-Hill Education. NY, 2019. 784 p.
- 23. Zienkiewicz, Cecil, O., Morice, P. The Finite Element Method in Engineering Science. 1st edn. McGraw-Hill. London, 1971. 521 p.
- 24. Taher, N.R., Mesut, G., Aksoy, H.S., Ahmed, H. Numerical investigation of the effect of slope angle and height on the stability of a slope composed of sandy soil. Gümüşhane Üniversitesi Fen Bilimleri Dergisi. 2022. 12(2). Pp. 664–675. DOI: 10.17714/gumusfenbil.1051741
- Nitzsche, K., Herle, I. Strain-dependent slope stability. Acta Geotechnica. 2020. 15(11). Pp. 3111–3119. DOI: 10.1007/s11440-020-00971-3

Information about the authors:

Zuhair Abd Hacheem, PhD

E-mail: zuhairabd@uomustansiriyah.edu.iq

Sahar Al-Khyat, PhD

E-mail: saharalkhyat@uomustansiriyah.edu.iq

Khitam Abdulhussein Saeed, PhD

E-mail: khitamhussein@uomustansiriyah.edu.iq

Sabah Fartosy, PhD

ORCID: https://orcid.org/0000-0001-5831-297X E-mail: dr.sabah77@uomustansiriyah.edu.iq

Received 01.02.2023. Approved after reviewing 19.10.2024. Accepted 26.10.2024.



Magazine of Civil Engineering

ISSN 2712-8172

journal homepage: http://engstroy.spbstu.ru/

Research article UDC 624.074.433

DOI: 10.34910/MCE.132.8



Ensuring uniform brightness of the afterglow surface of the hardened cement paste with photoluminescent pigment

L.A. Suleymanova ¹, A.A. Maslennikova ¹, D.E. Kravchenko ¹, N.V. Martyushev ², N.I. Vatin ³, A.I. Karlina ⁴

- 1 Belgorod State Technological University named after V.G. Shukhov, Belgorod, Russian Federation
- 2 National Research Tomsk Polytechnic University, Tomsk, Russian Federation
- 3 Peter the Great St. Petersburg Polytechnic University, St. Petersburg, Russian Federation
- 4 Moscow State University of Civil Engineering, Moscow, Russian Federation

⊠ martjushev@tpu.ru

Keywords: afterglow brightness, photoluminescent pigment particle size s, hardened cement paste, uniformity, particle size distribution, light emission stability, hydration processes, decorative concrete, luminescent properties

Abstract. The elevated standards for architectural and artistic expression, pivotal in enhancing the livability of urban landscapes, are significantly influenced by the innovative characteristics of materials employed in landscaping features and minor architectural structures. This paper delves into the influence of the particle size distribution of photoluminescent pigments on the quality of afterglow observed on the surface of hardened cement paste. Utilizing a method of computer image analysis, the study scrutinized samples with diverse compositions containing varying proportions of photoluminescent pigments. The principal aim of the investigation was to evaluate the uniformity of afterglow luminosity across the surface of hardened cement paste integrated with photoluminescent pigment. Experimental results revealed that the pigment fraction measuring 100–110 μm demonstrated superior uniformity and longevity of afterglow, while maintaining the integrity of the hydration processes within the cement matrix. In contrast, fractions sized 30–40 μm and 180–190 μm exhibited a diminished uniformity in the dispersion of light spots on the surface of hardened cement paste by 79 % and 88 %, respectively. This discrepancy can be ascribed to variations in the quantity of particles capable of photoluminescence and their distribution within the volume of the cement matrix.

Funding: This work was realized in the framework of the Program "Priority 2030" on the base of the Belgorod State Technological University named after V.G. Shukhov. The work was realized using equipment of High Technology Center at BSTU named after V.G. Shukhov.

Citation: Suleymanova, L.A., Maslennikova, A.A., Kravchenko, D.E., Martyushev, N.V., Vatin, N.I., Karlina, A.I. Ensuring uniform brightness of the afterglow surface of the hardened cement paste with photoluminescent pigment. Magazine of Civil Engineering. 2024. 17(8). Article no. 13208.

1. Introduction

Photoluminescent materials constitute a crucial category in construction due to their afterglow capability, rendering them appealing for various applications such as signaling, emergency lighting, and decorative purposes. Typically, in the manufacturing of construction materials, photoluminescent pigments (PLPs) are incorporated into cement-based formulations [1–5]. However, for the effective utilization of PLPs in construction materials, ensuring their uniformity and stability of light emission is imperative [6–8].

© Suleymanova, L. A., Maslennikova, A.A., Kravchenko, D.E., Martyushev, N.V., Vatin, N.I., Karlina, A.I., 2024. Published by Peter the Great St. Petersburg Polytechnic University.

Afterglow denotes a phenomenon wherein a material retains light energy and emits it for a specific duration after the external light source is removed. This phenomenon relies on the properties of photoluminescence, which are achieved by integrating PLPs into the material. PLPs possess the ability to absorb and store light energy, subsequently emitting it as visible light for a certain period [9, 10].

With an increase in the concentration of pigments, the brightness of the afterglow increases, but at certain concentrations, attenuation and degradation of the light properties of the material are observed [11]. At the same time, different types of pigments exhibit varying durations of afterglow and spectral characteristics. For example, some pigments have a long afterglow, which can be useful for decorative and safety lighting, while other pigments provide a brighter glow, suitable for signal markings [12].

Various additives and substances in PLPs cement composites have different effects on afterglow. Thus, some additives contribute to a better dispersion of pigments and an increase in the uniformity of light emission, while others can lead to undesirable interactions that affect light emission [13]. In [14], methods for synthesizing PLPs and their effect on the afterglow brightness were studied. The authors presented a new method for the synthesis of pigments, which makes it possible to obtain particles with improved light-emitting properties. It has been shown that the use of such pigments in cement-based composites improves the brightness of the afterglow and the uniformity of light emission [14].

Conditions for the production and optimization of the process of applying PLPs on the surface of hardened cement paste on the light-emitting properties of materials. Mixing parameters, curing temperature and humidity play a decisive role in the formation of a homogeneous structure of the material and its light-emitting properties [15]. At the same time, new application methods, such as mixing pigments with transparent coatings and the use of special adhesives, make it possible to achieve a more uniform distribution of pigments on the surface and increase the brightness of the afterglow [16–18].

The use of PLPs in building materials, such as concrete, represents an important class of materials with afterglow results. These PLPs facilities are designed for a variety of purposes including alarms, emergency lighting, and decorative features. However, for the beneficial use of PLPs in building materials, it is necessary to ensure their visibility and stability of luminescence [19, 20].

Uniformity means that the luminous properties of a material should be uniform and uniform across its entire surface to avoid the appearance of uneven bright or dull areas. Glow stability is important so that the luminous properties of the material do not change over time and under the influence of various operating conditions [21–23].

To achieve this goal, it is necessary to study the influence of the particle size distribution of pigments on the afterglow quality, since when analyzing the afterglow of the surface of hardened cement paste, it is important to consider how the particle size affects the texture and homogeneity of the coating and the color intensity due to the fact that, based on available data [9, 10], the influence of the particle size of pigments is (or should be) an important factor influencing the uniformity and quality of the afterglow of hardened cement paste. Particle size distribution refers to the size and distribution of particles within a pigment. Studying the particle size distribution will help determine large particle sizes to achieve high results and stable luminescence.

Based on previous studies in the field of PLPs building materials, further research should probably be conducted to study the light after luminescence of the hardened cement paste surface with PLPs.

The aim of the work is to establish the possibility of providing the best uniformity of afterglow of hardened cement paste by using PLP of different sizes.

The use of hardened cement paste is due to the fact that, unlike concrete, it does not contain concrete aggregates, which allows for a better study of the effect of PLPs on the properties of hardened cement paste and a more accurate assessment of how different particle sizes of pigments affect the formation of hydrates.

The main objectives of the study are: to study the effect of different pigment particle sizes on the brightness distribution after the light source is removed; to apply an image entropy analysis algorithm to identify areas with increased brightness and to assess the uniformity of the distribution of light spots on the surface of the hardened cement paste; to compare the obtained data on the brightness and homogeneity of the afterglow for different pigment fractions in order to determine the optimal particle size to achieve the best results and to assess the effect of the selected pigment fractions on the hydration processes in the cement matrix to ensure that they do not disrupt the formation of the necessary hydrates that provide the strength and stability of the hardened cement paste.

2. Methods

This study employed a primary method based on computer image analysis. Each sample consisted of hardened cement paste with PLPs, substances capable of absorbing and then emitting light. Aalborg

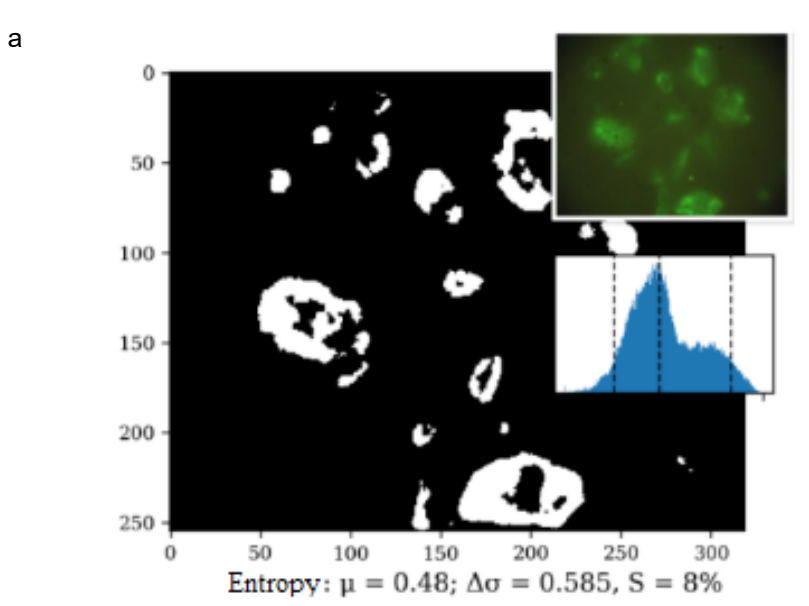
White CEM I 52.5R Portland cement (specific surface area $425 \text{ m}^2/\text{kg}$; mineral composition, %: $C_3S - 78.7$; $C_2S - 7.1$; $C_3A - 5.37$; $C_4AF - 0.49$) was used to prepare specimens with a water-cement ratio of 0.43 measuring $10 \times 10 \times 10$ cm. Waterproof, long-lasting, high-brightness pigment $SrAl_2O_4$: Eu^{2+} , Dy^{3+} particle sizes of 30-40, 100-110, and 180-190 µm and a yellow-green tint in an amount of 10 % of the cement mass were used as PLP for concrete. The glow intensity increases with increasing content of PLP in concrete, however, according to [8], the glow intensity of samples with a pigment content above 10 % changes insignificantly. The use of this type of pigment of such a particle size is due to its high quantum efficiency, long afterglow phase, and high resistance to ultraviolet radiation. When measuring the initial brightness of the afterglow under standard experimental conditions, we photographed the samples after 14 days of their hardening in natural humid conditions. This allowed us to capture the initial level of luminescence that occurs after exposure to light and subsequent extinction.

For analyzing the quality of the surface afterglow, we utilized an image entropy analysis algorithm. This algorithm enabled us to identify areas of the image where brightness changes most intensively, indicating transitions from dark to light regions [24, 25]. Subsequently, we applied binarization to divide the image into "white" and "black" areas, helping evaluate how evenly the luminescent spots were distributed across the surface of the hardened cement paste.

Within the scope of the study, several criteria were selected for quality assessment, including the average level of the brightness histogram (μ) , contrast $(\Delta\sigma)$, and uniformity (S) of light spots. A comparison of the histogram median (μ) across different samples enables conclusions to be drawn regarding the contrast of light spots on the surface. Samples exhibiting higher median entropy generally exhibit greater contrast. The width of the histogram $(\Delta\sigma)$ allows for the comparison of samples based on the uniformity of changes in brightness over the surface. A narrower histogram typically indicates a more uniform distribution of afterglow foci. The afterglow brightness was estimated by measuring the afterglow of the sample using a lux meter in a dark room at an illumination brightness of 0 lux, after removing the excitation (charge) irradiation from the D65 light source [7].

3. Results and Discussion

Histograms of images were analyzed, which displayed the distribution of the entropy of brightness in magnitude (Fig. 1). The images presented in the graphs show the distribution of brightness entropy with 5, 50, and 95 % quantiles labeled.



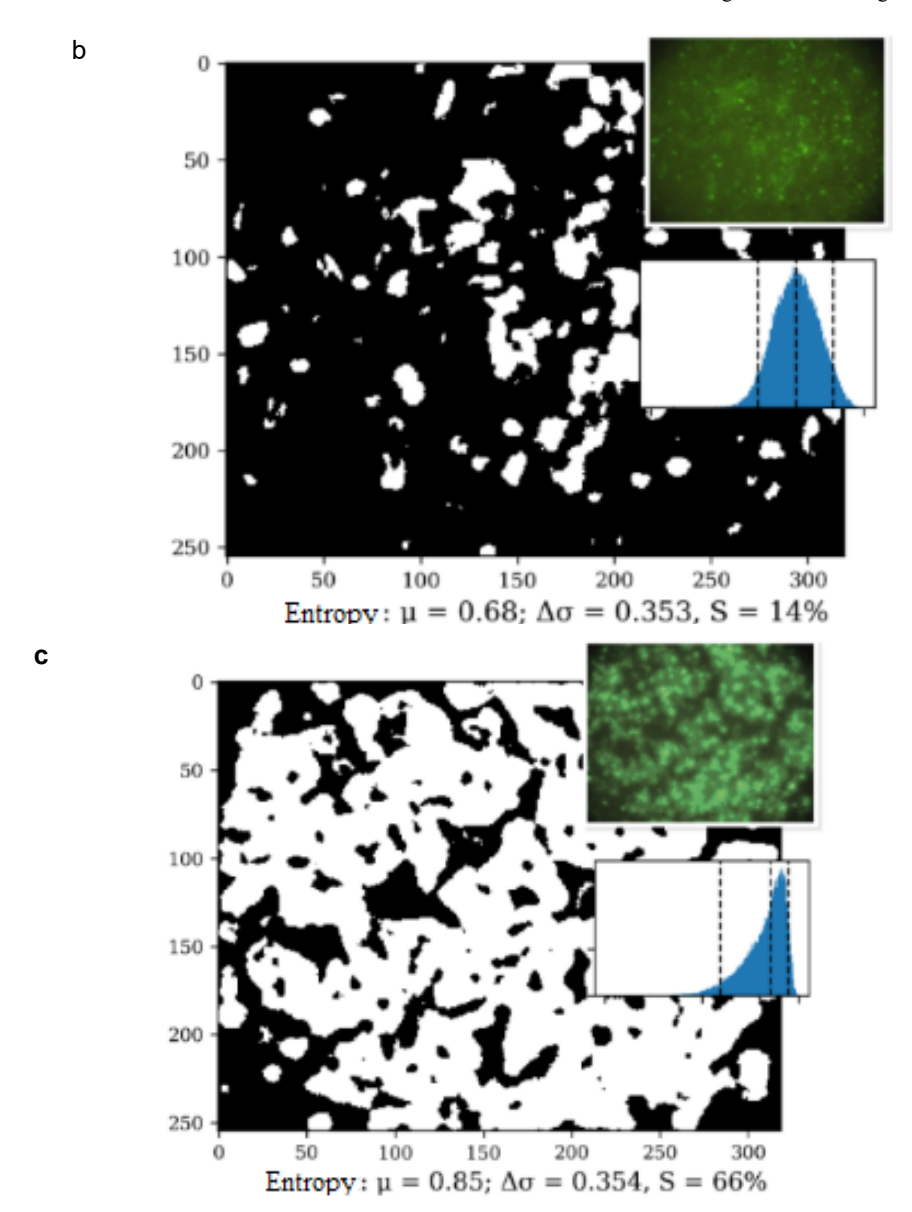


Figure 1. Uniformity of the afterglow of the surface of samples with PLP with different fractions: $a-180-190 \mu m$ 10 %; $b-30-40 \mu m$ 10 %; $c-100-110 \mu m$ 10 %.

The results demonstrate that incorporating fractions of PLPs sized 30– $40~\mu m$ and 180– $190~\mu m$ into hardened cement paste significantly reduces the uniformity of light spot distribution on its surface. The reduction in uniformity amounts to 79~% and 88~%, respectively. This reduction is consistent with findings from Wang et al. [2], who observed a 75~% decline in uniformity with larger particle sizes.

To delve deeper into the impact of the 180–190 μm PLPs fraction, introducing this fraction while maintaining a constant pigment mass ratio in the cement matrix results in a lower number of PLPs particles capable of generating photoluminescence. This leads to non-uniform afterglow within the cement matrix volume, thereby causing a reduction in the uniformity of light spot distribution on the surfaces of specimens containing this PLPs fraction (Fig. 1, a).

In contrast, the 30–40 µm PLPs fraction promotes the formation of a denser surface layer through the growth of new formations, such as calcium silicate hydrate and tricalcium aluminate hydrate (Fig. 1, b). This results in the formation of a dense surface layer of C-S-H, the main product of cement hydration, and AFt (aluminoferrites) as crystalline structures formed in the presence of excess calcium and sulfate during hydration, which in turn results in partial pigment closure or pigment encapsulation (Fig. 2). This encapsulation is critically important as it is directly related to the observed reduction in brightness and afterglow duration. Gao et al. [3] observed a 65 % reduction in brightness due to densification with smaller PLP fractions.

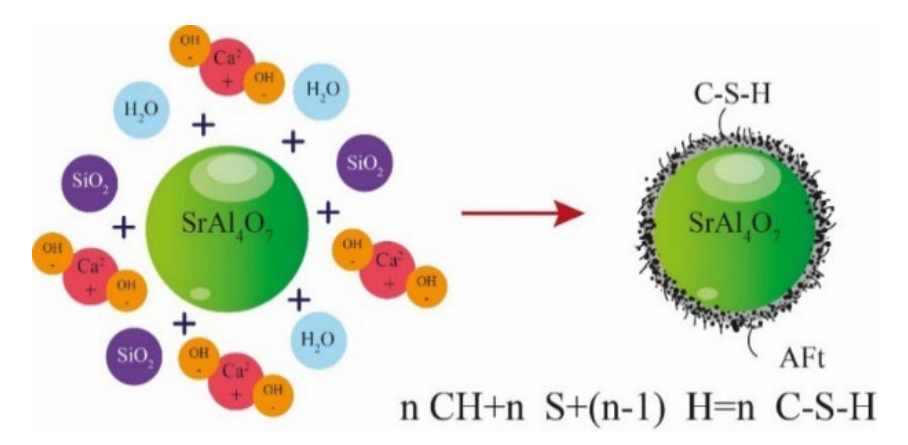


Figure 2. Scheme of C-S-H and AFt around PLPs particles.

The fraction of PLPs with a size of $100-110~\mu m$ exhibits properties that contribute to a uniform afterglow of the surface of the hardened cement paste. This particle size is smaller than the particle size of Portland cement, allowing the PLPs to form a layer on the surface of the cement sample that is uniform and open to light irradiation, maintaining a uniform distribution of light spots (Fig. 1, c). He et al. [5] found a 90 % improvement in uniformity with optimal particle size selection.

The 100–110 µm PLPs fraction fills voids in the mixture, creating a denser structure. These particles penetrate the pores of the cement matrix, optimizing its structure (Fig. 3), which apparently has a positive effect on the subsequent strength of concrete with photoluminescent properties. Wang et al. [4] reported a 20 % increase in compressive strength with similar optimization.

After the initial increase in concrete strength, a slow stage begins, during which a significant change in the composition of hydration products occurs. This stage is critical for the formation of a concrete structure that will have optimal properties throughout its entire service life. Thus, the selection and use of the $100-110~\mu m$ PLPs fraction does not disrupt the hydration of the components in the mixture (Fig. 4), without leading to excessive formation of C-S-H and AFt around the particles, which critical to ensure the durability and reliability of concrete structures.

The PLPs fraction of $100-110 \, \mu m$ has an optimal size that allows it to be integrated into the cement matrix without disrupting the hydration process. This means that PLPs particles do not interfere with the formation of C-S-H and AFt hydrates around them. Thus, the PLPs fraction does not cause unnecessary formations or anomalies in the structure of concrete, which can lead to a deterioration in its quality.

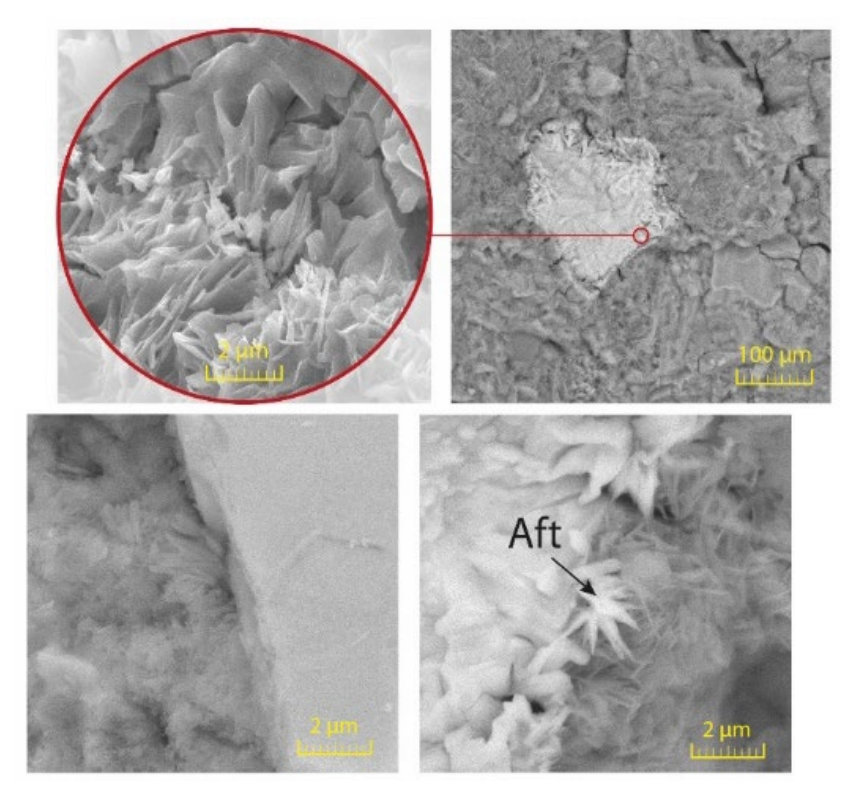


Figure 3. Microstructure of hardened cement paste containing PLP with fraction of 100-110 µm.

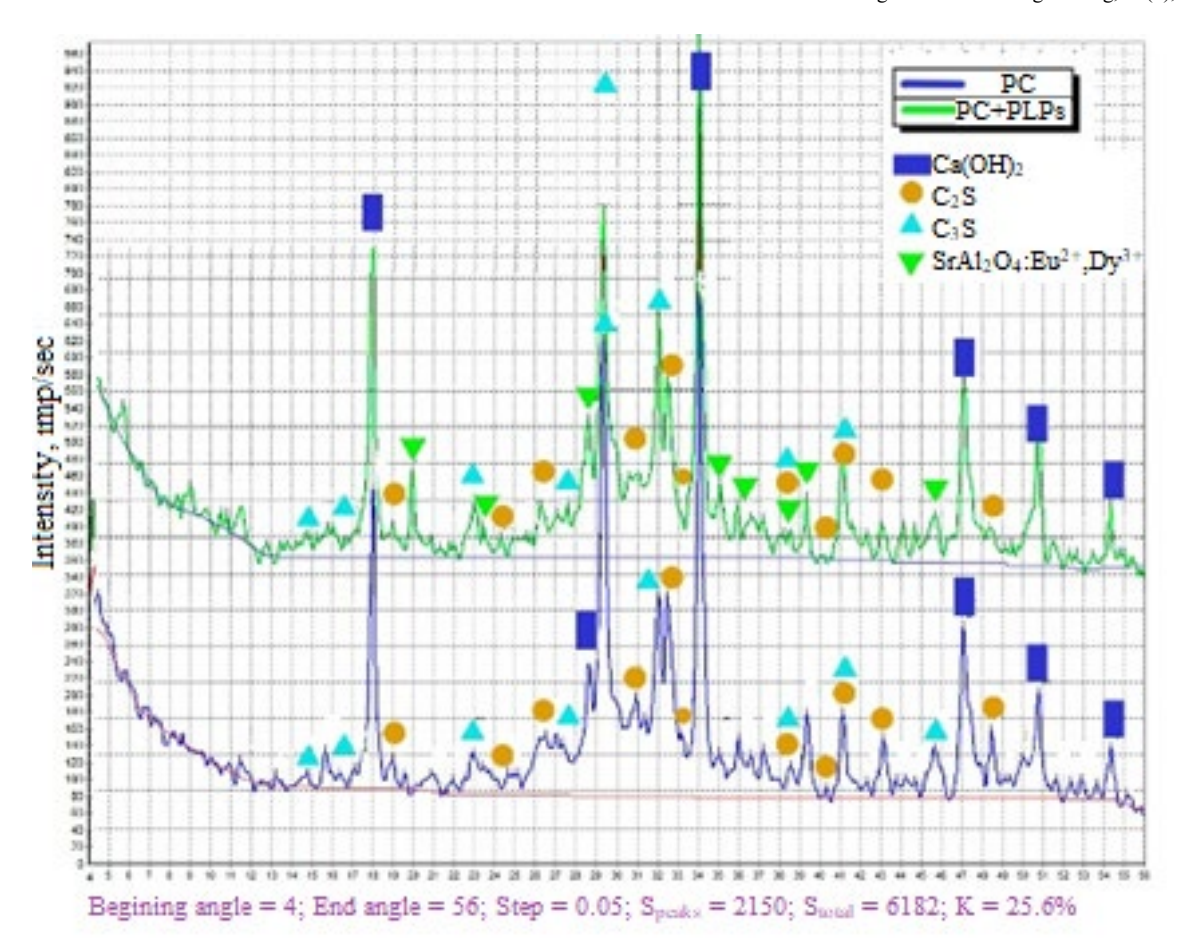


Figure 4. Radiographs of hardened cement paste using Portland cement and Portland cement containing PLP with fraction of 100–110 µm.

Due to their size and chemical composition, PLPs particles of $100-110~\mu m$ are integrated into the structure of the hardened cement paste, maintaining its strength and stability. This integration creates more durable and reliable concrete structures, reducing the risk of deformation or destruction due to inhomogeneities in the structure. Solís et al. [11] observed a 15 % reduction in structural deformation with optimal PLP integration.

The introduction of PLPs into building materials aims to improve the decorative properties of the material without reducing its physical and mechanical characteristics. It is crucial that these pigments do not affect the hydration of the mixture components or lead to excessive formation of hydration products around the pigment particles. Hydration is the chemical process of cement reacting with water to form the hydrate compounds necessary for a strong concrete matrix. Suleymanova et al. [8] found that improper selection of PLP fractions can result in a 30 % increase in unwanted hydration products.

The study confirmed that the correct choice of the PLPs fraction plays a key role in ensuring a uniform and high-quality afterglow of the surface of the hardened cement paste. The PLPs fraction with a size of 100–110 μ m showed the best properties in this regard, providing a uniform and long-lasting afterglow without interfering with hydration processes in the cement matrix. Tunali and Selli [10] emphasized the importance of particle size, noting that the 100–110 μ m fraction provided 25 % longer afterglow than other sizes in the natural state, which is consistent with studies conducted on pigment afterglow in hardened cement paste.

Based on the studies, the pigment fractions were ranked according to the increase in the homogeneity of the afterglow of the hardened cement paste with their use in the following sequence: 180–190 μ m \rightarrow 30–40 μ m \rightarrow 100–110 μ m.

4. Conclusion

The results of the study on the example of waterproof, long-lasting, high-brightness pigments SrAl₂O₄: Eu²⁺, Dy³⁺ show that the particle size distribution of PLPs has a significant impact on the afterglow quality of the hardened cement paste surface.

It was found that with the introduction of PLP fractions with sizes of 30–40 μ m and 180–190 μ m, the uniformity of the distribution of light spots decreases by 79 % and 88 %, respectively, in relation to PLP

fraction 100–110 μ m. This means that the use of these PLPs fractions leads to a less uniform distribution of luminous points on the surface of the hardened cement paste.

Pigment fractions are ranked according to the increase in the afterglow uniformity of the hardened cement paste when used in the following sequence: $180-190 \ \mu m \rightarrow 30-40 \ \mu m \rightarrow 100-110 \ \mu m$.

With equal consumption of different pigment fractions by mass, the low efficiency of the large fraction (180–190 μm) is explained by the smaller number of particles capable of exhibiting photoluminescence, as well as their heterogeneous distribution in the volume of the cement matrix. In the case of the finely dispersed fraction (30–40 μm), the pigment particles, due to their size, form a denser coating of the surface with new formations of hardened cement paste, which leads to a decrease in the brightness and duration of the afterglow.

It has been established that the results of the study of the deep glow allow selecting the stage of PLPs to ensure high quality afterglow and the effect of light spots on the surface of the hardened cement paste. It is possible that the effect of pigment size established in this work may be somewhat different quantitatively when using other pigments and cements. However, the results of the work showed the possibility of ensuring the best uniformity of the afterglow of hardened cement paste by using PLPs of a certain size.

The $100-110~\mu m$ fraction is gaining attention as the strongest choice of this decade. Its use gives the best results in terms of uniformity and duration of afterglow without disturbing the hydration processes in the cement matrix. This indicates that the working fraction is capable of providing not only effective glow, but also maintaining the stability and strength of the material itself.

These findings represent an important step in the development of the construction industry, where the requirements for the aesthetic and functional characteristics of materials are constantly evolving. The research results will be useful in creating new building materials with photoluminescent effects, which will allow engineers and architects to create more sustainable, attractive, and reliable structures.

Therefore, proper selection of PLPs is a key factor to ensure post-glow quality of building materials, and this study will help in this process.

References

- Suleymanova, L.A., Malyukova, M.V., Koryakina, A.A. Architectural and decorative concrete with photoluminescent pigment. IOP Conference Series Materials Science and Engineering. 2020. 896(1). Article no. 012025. DOI: 10.1088/1757-899X/896/1/012025
- Wang, W., Sha, A., Lu, Z., Yuan, D., Jiang, W., Liu, Z. Cement filled with phosphorescent materials for pavement: Afterglow decay mechanism and properties. Construction and Building Materials. 2021. 284. Article no. 122798. DOI: 10.1016/j.conbuildmat.2021.122798
- 3. Gao, Y., He, B., Xiao, M., Fang, Z., Dai, K. Study on properties and mechanisms of luminescent cement-based pavement materials with super-hydrophobic function. Construction and Building Materials. Article no. 2018. 165. Pp. 548–559. DOI: 10.1016/j.conbuildmat.2017.12.231
- Wang, W., Sha, A., Lu, Z., Jia, M., Jiang, W., Liu, Z., Yuan, D. Self-luminescent cement-based composite materials: properties and mechanisms. Construction and Building Materials. 2021. 269. Article no. 121267. DOI: 10.1016/j.conbuildmat.2020.121267
- He, B., Gao, Y., Leng, Zh., Qu, L., Peng, J., Fang, Z. Study on strength and optical properties of photoluminescence cement-based composites materials. Journal of Functional Materials. 2019. 50(7). Article no. 07126. DOI: 10.3969/j.issn.1001-9731.2019.07.023
- 6. Li, Y., Ren, S. Building Decorative Materials. 1st edn. Woodhead Publishing, 2011. Pp. 10–24.
- Suleymanova, L.A., Malyukova, M.V., Ryabchevskiy, I.S., Koryakina, A.A., Levshina, D.E. Glowing Decorative Concrete Using Rock Crushing Waste. Bulletin of Belgorod State Technological University named after V.G. Shukhov. 2021. 5(12). Pp. 8–16. DOI: 10.34031/2071-7318-2020-5-12-8-16
- 8. Suleymanova, L.A., Malyukova, M.V., Koryakina, A.A. Research of Photoluminescent Pigment for Use in Luminous Architectural and Decorative Concrete. Bulletin of Belgorod State Technological University named after V.G. Shukhov. 2021. 6(6). Pp. 8–18. DOI: 10.34031/2071-7318-2021-6-6-8-18
- Lusvardi, G., Malavasi, G., Menabue, L., Smargiassi, M. Systematic Investigation of the Parameters that Influence the Luminescence Properties of Photoluminescent Pigments. Journal of Luminescence. 2016. 175. Pp. 141–148. DOI: 10.1016/j.jlumin.2016.02.038
- 10. Tunali, A., Selli, N.T. Influence of the Photoluminescent Pigments' Particle Size Distribution on the Afterglow Duration. Acta Physica Polonica A. 2014. 125. Pp. 513–514. DOI: 10.12693/APhysPolA.125.513
- Solís, C.G., Vallejo, M., Sosa, M., Bernal Alvarado, J.J., Fraga, T., Fajardo, G., Torres-Martínez, L.M. Development of Photoluminescence White Cement Based Materials and Physic-Mechanical Study. Research in Computing Science. 2020. 149(2). Pp. 61–70.
- 12. Naeem, M., Khan, S., Zekker, I., Subhan, F., Salman, M., Khan, A. Application of Strontium Aluminate Europium and Dysprosium Doped in Cement Mortar as a Luminescent Material for the Maintenance of Green Environments. Journal of Hazardous, Toxic, and Radioactive Waste. 2023. 27(1). Article no. 04022032. DOI: 10.1061/(ASCE)HZ.2153-5515.0000716
- 13. Dipika, G., Kaaviya, S., Karthikeyan, S.K., Indhumathi, S. Exploratory Study On Photo Luminescence Induced Concrete. International Journal of Civil Engineering and Technology (IJCIET). 2019. 10(3). Pp. 622–628.
- 14. Sundari, S., Shriswarnambigai, A. Experimental study on Luminescent Concrete. International Research Journal of Engineering and Technology (IRJET). 2021. 8(6). Pp. 4188-4196.

- Dang, J., Song, C., Qiao, M., Li, G., Dong, S., Fan, F., Lv, Y. Characteristics analysis of long afterglow phosphor with SiO₂ coating and evaluation its influence on the properties of self-luminescent cement-based materials. Construction and Building Materials. 2023. 407. Article no. 133402.DOI: 10.1016/j.conbuildmat.2023.133402
- Wang, W., Sha, A., Li, X., Zhang, F., Jiang, W., Yuan, D., Liu, Z. Water resistance and luminescent thermal stability of SiO₂ coated phosphor and self-luminous cement-based materials: View from the perspective of hydration balance. Construction and Building Materials. 2022. 319. Article no. 126086. DOI: 10.1016/j.conbuildmat.2021.126086
- 17. Sanjuána, M.A., Argiz, C. Photoluminescent cements. Afinidad. 2019. 76(588). Pp. 262–269.
- Amor, F., Ingrišová, L., Rácová, Z., Baudys, M., Hájek, P. Effect of TiO₂ and ZnO powder mixtures on mechanical and photocatalytic performance of high performance concrete. Acta Polytechnica CTU Proceedings. 2022. 33. Pp. 15–19. DOI: 10.14311/APP.2022.33.0015
- Oesterle, A., Boehm, A.V., Müller, F.A. Photoluminescent Eu³⁺-Doped Calcium Phosphate Bone Cement and Its Mechanical Properties. Materials. 2018. 11(9). Article no. 1610. DOI: 10.3390/ma11091610
- Gabouze, N., Hadjersi, T., Guerbous, L. Photoluminescence from porous layers formed on phosphorus-implanted silicon by Agassisted chemical etching. Physica Status Solidi (C) Current Topics in Solid State Physics. 2007. 4(6). Pp. 2160–2164. DOI: 10.1002/pssc.200674410
- 21. Ptáček, P., Šoukal, F., Opravil, T., Bartoníčková, E., Zmrzlý, M., Novotný, R. Synthesis, hydration and thermal stability of hydrates in strontium-aluminate cement. Ceramics International. 2014. 40(7(A)). Pp. 9971–9979. DOI: 10.1016/j.ceramint.2014.02.095
- 22. Acuña Ulises, A.; Amat-Guerri, F.; Morcillo, P.; Liras, M.; Rodríguez, B. Structure and Formation of the Fluorescent Compound of *Lignum nephriticum*. Organic Letters. 2009. 11(14). Pp. 3020–3023. DOI: 10.1021/ol901022g
- 23. Timilsina, S., Bashnet, R., Kim, S.H., Lee, K.H., Kim, J.S. A life-time reproducible mechanoluminescent paint for the visualization of crack propagation mechanisms in concrete structures. International Journal of Fatigue. 2017. 101(1). Pp. 75–79. DOI: 10.1016/j.ijfatigue.2017.03.011
- 24. Al-Senani, G.M., Al-Qahtani, S.D. Silica nanoparticle-reinforced polyurethane plastic immobilized with strontium aluminate nanofiller: Ultraviolet protection, superhydrophobicity and photoluminescence. Journal of Photochemistry and Photobiology A: Chemistry. 2024. 456. Article no. 115808. DOI: 10.1016/j.jphotochem.2024.115808
- 25. El-Newehy, M.H., Thamer, B.M., Abdulhameed, M.M. Preparation of luminescent polyethylene plastic composite nano-reinforced with glass fibers. Journal of Applied Polymer Science. 2024. 141(14). Article no. e55189. DOI: 10.1002/app.55189

Information about the authors:

Lyudmila Suleymanova, Doctor of Technical Sciences

ORCID: <u>https://orcid.org/0000-0002-1180-558X</u>

E-mail: <u>ludmilasuleimanova@yandex.ru</u>

Alina Maslennikova, PhD in Technical Sciences

E-mail: alinakoryakina.arch@gmail.com

Darya Kravchenko,

ORCID: https://orcid.org/0009-0009-8618-2952

E-mail: darya.levshina@mail.ru

Nikita Martyushev, PhD in Technical Sciences

E-mail: <u>martjushev@tpu.ru</u>

Nikolai Vatin, Doctor of Technical Sciences ORCID: https://orcid.org/0000-0002-1196-8004

E-mail: vatin@mail.ru

Antonina Karlina, PhD in Technical Sciences ORCID: https://orcid.org/0000-0003-3287-3298

E-mail: karlinat@mail.ru

Received 31.05.2024. Approved after reviewing 17.11.2024. Accepted 23.11.2024.

